Università degli Studi di Padova

Doctoral Thesis

Musculoskeletal Modeling of the Human Lower Limb Stiffness for Robotic Applications

School Director:
Prof. Matteo Bertocco
Coordinator:
Prof. Carlo Ferrari
Supervisor:
Prof. Enrico Pagello
Ph.D. Candidate:
Roberto Bortoletto

A thesis submitted in fulfilment of the requirements
for the degree of Doctor of Philosophy

in the

Information and Communication Science and Technologies (ICT)

Intelligent Autonomous Systems Laboratory (IAS-Lab)
Department of Information Engineering (DEI)

January, 2016

To my son Gianluca

Acknowledgements

I would like to express my special appreciation and thanks to my advisor, Professor Eng. Enrico Pagello, and to my co-advisor, Professor Davide Piovesan, for having encouraged my research and for having followed me in this years. Your advices on my research as well as on my career have been extremely important. I would like to thank Prof. Emanuele Menegatti, for allowing me to conduct my research at the Intelligent Autonomous Systems Laboratory by supporting my activity so far. Thank you so much to all my colleagues and friends.

A special thanks to my mother and father for all of the sacrifices that you have made on my behalf, through which I was able to go on my way.

At the end, a huge thanks and a special hug goes to my beloved girlfriend, Serena, who is always my support, and without which I would not have achieved certain goals.

Abstract

Musculoskeletal Modeling of the Human Lower Limb Stiffness for Robotic Applications

This research work presents a physiologically accurate and novel computationally fast neuromusculoskeletal model of the human lower limb stiffness. The proposed computational framework uses electromyographic signals, motion capture data and ground reaction forces to predict the force developed by 43 musculotendon actuators. The estimated forces are then used to compute the musculotendon stiffness and the corresponding joint stiffness. The estimations at each musculotendon unit is constrained to simultaneously satisfy the joint angles and the joint moments of force generated with respect to five degrees of freedom, including: Hip Adduction-Abduction, Hip Flexion-Extension, Hip Internal-External Rotation, Knee Flexion-Extension, and Ankle Plantar-Dorsi Flexion. Advanced methods are used to perform accurate muscle-driven dynamic simulations and to guarantee the dynamic consistency between kinematic and kinetic data.

This study presents also the design, simulation and prototyping of a small musculoskeletal humanoid made for replicating the human musculoskeletal structure in an artificial apparatus capable to maintain a quiet standing position using only a completely passive elastic actuation structure. The proposed prototype has a total mass of about 2 kg and its height is 40 cm. It comprises of four segments for each leg and six degrees of freedom, including: Hip Adduction-Abduction, Hip Flexion-Extension, Knee Flexion-Extension, Ankle Plantar-Dorsi Flexion, Ankle Inversion-Eversion, and Toe Flexion-Extension. In order to reconstruct the continuous state space parameters proper of the assembly's control of quiet standing, a hybrid non-linear Extended Kalman Filter based technique is proposed to combine a base-excited inverted pendulum kinematic model of the robot with the discrete-time position measurements.

This research work provides effective solutions and readily available software tools to improve the human interaction with robotic assistive devices, advancing the research in neuromusculoskeletal modeling to better understand the mechanisms of actuation provided by human muscles and the rules that govern the lower limb joint stiffness regulation. The obtained results suggest that the neuromusculoskeletal modeling technology can be exploited to address the challenges on the development of musculoskeletal humanoids, new generation human-robot interfaces, motion control algorithms, and intelligent assistive wearable devices capable to effectively ensure a proper dynamic coupling between human and robot.

Sommario

Modellazione Muscoloscheletrica della Rigidezza Articolare dell'Arto Inferiore Umano per Applicazioni Robotiche

Questa ricerca presenta un nuovo modello neuromuscoloscheletrico della rigidezza articolare dell'arto inferiore umano, fisiologicamente consistente e computazionalmente veloce. Il modello computazionale proposto usa segnali elettromiografici, dati di movimento e forze di reazione al suolo per predire la forza sviluppata da 43 attuatori muscolotendinei. Le forze stimate sono poi usate per calcolare la rigidezza muscoloteninea e la corrispondente rigidezza articolare. Le stime, per ogni unità muscolotendinea, sono vincolate a soddisfare simultaneamente gli angoli e i momenti generati ai giunti, rispetto a cinque gradi di libertà: Adduzione-Abduzione, Flesso-Estensione e Rotazione Interna-Esterna dell'Anca, Flesso-Estensione del Ginocchio e Flessione Dorsi-Plantare della Caviglia. Metodi avanzati sono stati utilizzati per l'esecuzione di simulazioni dinamiche e per garantire la consistenza tra i dati cinematici e cinetici.

Nel presente lavoro, viene inoltre descritta la progettazione, simulazione e prototipazione di un piccolo umanoide, realizzato per replicare la struttura muscoloscheletrica umana in un apparato artificiale, in grado di mantenere una posizione eretta stabile utilizzando una struttura di attuazione elastica completamente passiva. Il prototipo proposto ha una massa totale di circa 2 kg e un'altezza di 40 cm. Ciascuna gamba è composta da quattro segmenti e si articola su sei gradi di libertà: Adduzione-Abduzione e Flesso-Estensione dell'Anca, Flesso-Estensione del Ginocchio, Flessione Dorsi-Plantare e Inversione-Eversione della Caviglia, Flesso-Estensione delle dita del Piede. Per ricostruire i parametri di stato nel mantenimento della posizione eretta, viene proposta una tecnica ibrida che coniuga l'utilizzo di un Filtro di Kalman Esteso non lineare, un modello del robot basato su pendolo inverso eccitato alla base e misure di posizione.

L'obiettivo di questo lavoro è di fornire soluzioni efficaci e strumenti software atti a migliorare l'interazione umana con ausili robotici. Questa tesi si propone di contribuire al progresso della ricerca nella modellazione neuromuscoloscheletrica per comprendere meglio i meccanismi di attuazione fornita dai muscoli umani, nonché le regole che governano la modulazione della rigidezza articolare degli arti inferiori. I risultati ottenuti suggeriscono che la modellazione neuromuscoloscheletrica può essere sfruttata per affrontare le sfide dello sviluppo di umanoidi, interfacce uomo-robot di nuova generazione, algoritmi di controllo del movimento e dispositivi indossabili intelligenti capaci di garantire in modo efficace un corretto accoppiamento dinamico tra uomo e robot.

Contents

List of Figures

List of Tables

Chapter 1

Introduction

The Central Nervous System (CNS) generates neural commands to activate the muscles in order to control the human body movements. Subsequent forces produced by muscles are transmitted by tendons to the skeleton to perform a specific motor task. Thus, muscles and tendons are the interface between the CNS and the articulated body segments [1]. Hence, the human sensory-motor control system cannot be understood by studying the control circuits (i.e., CNS) while ignoring the inherent properties and the mechanical dynamics of the musculoskeletal system that it must control [2]. A firm understanding of the properties of the whole framework, user's intention and action's generation, is important for both scientists and engineers in order to interpret kinesiological events in the context of coordination of the body and in order to design functional neuromuscular stimulation systems for restoring lost of impaired motor function, to develop new generation human-robot interfaces, and motion control algorithms for robotic leg prosthesis and intelligent assistive wearable devices.

1.1 The three pillars

The extraordinary breadth and multidisciplinary nature of the research field in neuromotor and robotics-based rehabilitation (i.e., neurorobotics) can be well summarized by three pillars (Fig. 1.2): NeuroMusculoSkeletal (NMS) modeling, Human-Machine Interfaces (HMIs), and Robot Control Strategies (RCSs).

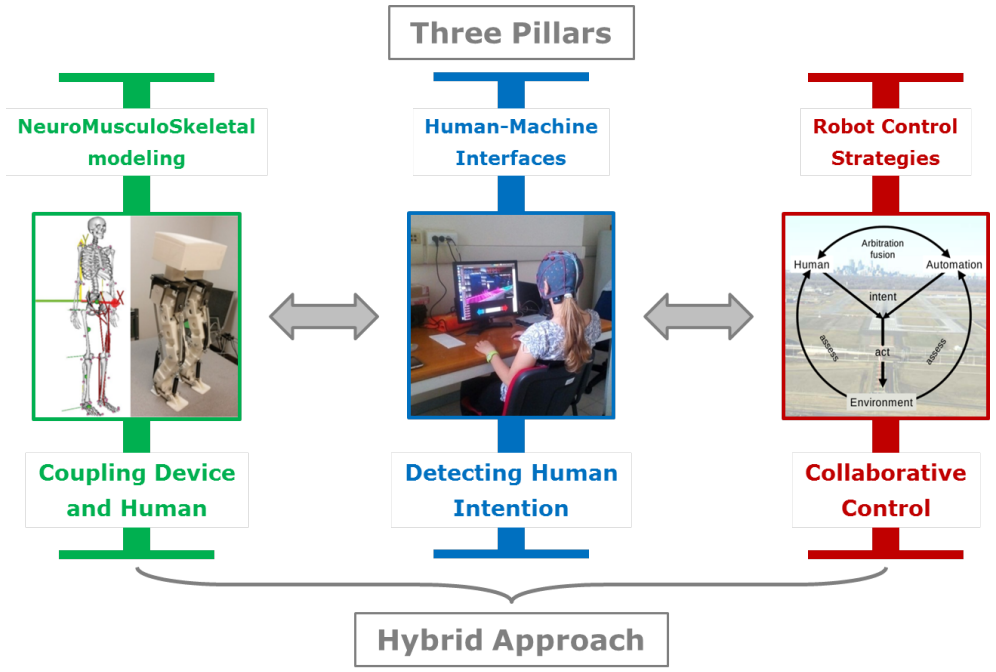

FIGURE 1.1: A schematic representation of the three pillars representing the three major topics in the neurorobotics research field.

The NMS modeling enhances coupling between human and robot, the HMI allows for detecting the high-level intention to move, while the RCS pillar implements a collaborative control approach. Thus, these three pillars are strictly correlated in a framework that allows for implementing an effective hybrid neurodriven control according to a Man-In-The-Loop approach.

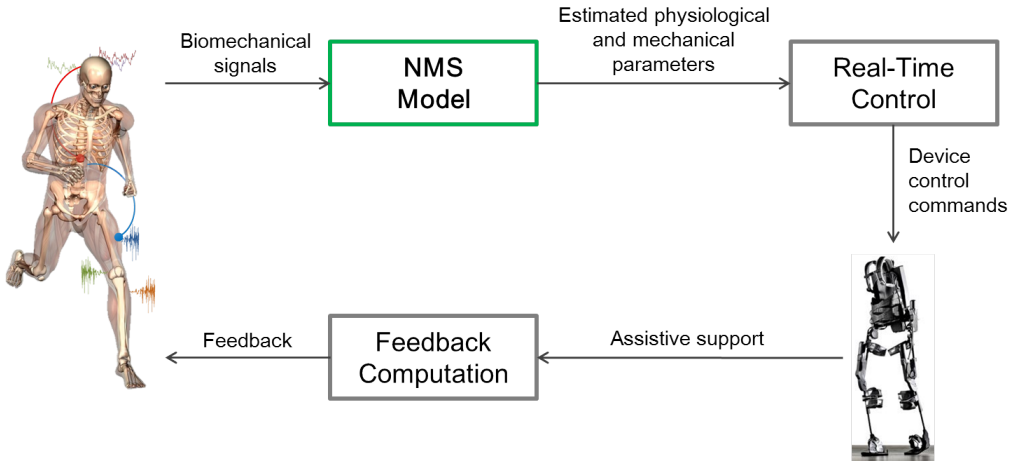

FIGURE 1.2: A schematic representation of the Man-In-The-Loop control approach using biomechanical signals to control a wearable robotic device or a software application.

1.1.1 Neuromusculoskeletal modeling

The first pillar is the topic on which this thesis is focused. Even more important, it represents a framework that allows for integrating models describing the anatomy and physiology of the human body, and the mechanics of multi-joint movement. From a biomechanical point of view, the analysis of movement plays an important role in both rehabilitation of neurological and orthopaedic conditions [3] as well as performance enhancement [4]. How mammals control the overconstrained actuation of their limb has been a research topic for decades. Human movement coordination requires some form of planning: every Degree Of Freedom (DOF) needs to be supplied with approriate motor commands at every moment in time. Because of the numerous DOFs in bipedal locomotion, there exist an infinite number of possible movement plans for any given task that is known as Bernstein's Degrees of Freedom problem [5]. This abundance of DOFs, also called *redundancy*, is advantageous as it allows as locomotion system to move around or between obstacles, avoiding situations where the range of motion for specific DOFs is limited. On the other hand, it makes planning a movement quite complicated since the number of all possible strategies to accomplish a task is extremely large.

Researchers have tried to simplify the problem postulating that the brain uses less independent commanding signals than those necessary to control each single muscle independently. Recently, a new prospective has been proposed by Kutch and Valero-Cuevas [6]. They showed that the dimensionality reduction observed in neurophysiological studies could simply arise from the physical constraint of the system. As humans move, accomplishing a task that require both the following of a trajectory and the exertion of a force, they must regulate not only the generated muscle forces, but also the stiffness of their limbs and joints in order to effectively interact with the environment. During unimpaired gait, depending on the terrain, one might either walk in a relaxed manner or stiffen up to increase stability.

Typically, *stiffness* is viewed as a material property describing the degree to which an object resists deformation when subjected to a known force. Sometimes this idea of deformation under a given load is discussed using the term *compliance* which is the inverse of stiffness [7]. This concept can be extended to the limbs and joints of biological organisms in which stiffness (i.e., the static component of *impedance*) describes the degree to which a joint bends under a given load [8, 9]. In particular, the translation of *stiffness classical physics definition* in the context of *human limb joints* was deeply

discussed by Mussa-Ivaldi et al. [10], by Latash and Zatsiorsky in a seminal work [11], and further addressed and extended, for the arm joints, by others [12, 13]. Humans use neural control, along with the mechanical constraints of the body, to adjust the stiffness as the body performs various tasks. It has been shown that humans change the stiffness of their limbs as they perform tasks such as hopping [14], accurate reaching tasks [15], or walking and running on different surfaces [16]. In particular, co-contraction of antagonistic muscle groups alters the biomechanical operating ranges of muscle and tendon by increasing both muscle damping and muscle-tendon stiffness [17, 18]. While the exact method by which this neural-modulation of limb stiffness occurs is unknown, many different hypotheses have been proposed [19, 20].

In this context, there exists also the concept of *quasi-stiffness*. It describes the relationship between joint angle and joint torque, and it is a frequently studied aspect in biomechanics with numerous applications, including motor control [21], prosthesis/orthosis design, and biologically inspired robotics [22]. The distinction between quasi-stiffness and stiffness was discussed by [11], wherein the authors stressed the important energy-storing nature of stiffness and described the physiological joint structures and their contribution to mechanical properties. Shamaei et al. [23] investigated the knee torque-angle relationship using a generalized inverse dynamics analysis approach in order to identify the key independent variables needed to predict knee quasi-stiffness during walking, including gait speed, knee excursion, and subject height and weight. It is also worth noting the studies related to the hip [24, 25] and ankle [26] quasi-stiffness estimation. Hansen et al. [27] reported ankle torque-angle relationships for various walking speeds, noting that quasi-stiffness characteristics of the human ankle appear to change as walking speed increases. Rouse et al. [28] demonstrated the differences between ankle quasi-stiffness and stiffness using two computational models, based on a simulated inverted pendulum and an impedance-controlled motor, with force information that could be obtained in a standard laboratory setting. While the estimation of quasi-stiffness can be derived by the inverse dynamics equations, measuring lower limb stiffness during locomotion requires perturbations from the desired trajectory. Hence, such experiments are difficult to perform and still in their infancies [29–32].

As argued by Delp et al. [33], a theoretical framework is needed, in combination with experiments, to uncover the principles that govern the coordination of muscles during normal movement, to determine how neuromuscular impairments contribute to abnormal movement and to predict the functional consequences of treatments. Over the last

decades, biomechanical models have been extensively used in order to understand the physiological basis of human and animal movement [34, 35]. One of the first mathematical muscle's models was proposed by Hill [36]. Gordon et al. [37] refined such model by incorporating the dependence between changes in muscle force as function of muscle lengths and contraction speeds. Zajac [38] extended the Hill's model introducing a muscle-tendon model, which is known as *Hill-type muscle force model*. More recently, muscle-actuated dynamic simulations based on the aforementioned biomechanical models and on the use of optimization algorithms are becoming an essential tool for determining how the elements of the musculoskeletal system interact to produce movement [39]. Such algorithms are usually based on a cost function that depends directly on a physical parameters such as force variance, energy, muscle stress, to name a few [40–42]. The commonly used optimization algorithms can be subdivided into *Static Optimization* (SO) [43] and *Dynamic Optimization* (DO) [44] approaches. The first refers to the process of minimizing or maximazing some objective function for one instant in time only. The second refers to the process of minimizing or maximizing some objective function over a period of time, and it is also sometimes called Optimal Control [45–47]. Using DO-based methods to compute excitation patterns comes at a large computational cost, which has limited their use within muscle-actuated simulations. Thelen et al. [48] proposed the Computed Muscle Control (CMC) algorithm. It uses a SO along with feedforward and feedback controls to drive the kinematic trajectory of a musculoskeletal model toward a set of desired kinematics. The speed and accuracy of this algorithm improved the feasibility of using detailed musculoskeletal models to simulate movement. Moreover, a further improvement to the performance of musculoskeletal optimizations comes with the introduction of supplemental sets of actuators (i.e., *reserve actuators*) included in addition to the modeled muscles, in order to adjust the Center of Gravity (COG) of each segment, notoriously difficult to measure [49], and to reduce *residual forces*. Anderson and Pandy [50] proposed a quantitatively comparison between a DO solution and two SO solutions adopted for the estimation of muscle forces during normal walking gait. They concluded that in terms of predicted muscle forces and joint contact forces, the dynamic and static solutions were similar. Moreover, activation dynamics and the Force-Length-Velocity (FLV) properties of muscle had little influence on the SO solutions. Lin et al. [51] performed a correlation analysis between three different muscle force solutions (i.e., Neuromusculoskeletal Tracking [52], SO, and CMC) in order

to determine the extent to which inclusion of muscle activation dynamics and a time-dependent performance criterion influences predictions of lower limb muscle forces for walking and running. The patterns of muscle loading predicted by the three methods were similar for both walking and running. The results suggested that the robustness and efficiency of SO make it the most attractive method for estimating muscle forces in human locomotion.

In light of this background, this thesis aims to provide an effective solution and readily available software tool to improve the human interaction with robotic assistive devices, advancing the research in NSM modeling to better understand the mechanisms of actuation provided by human muscles and the rules that govern the lower limb joint stiffness regulation. The obtained results suggest that the NMS modeling technology is mature enough to be exploited to address the challenges on the development of musculoskeletal humanoids and intelligent assistive wearable devices capable to effectively ensure a proper dynamic coupling between human and robot.

1.1.2 Human-Machine Interfaces

The second pillar is based on the fact that the detection of the intention to move is a necessary condition to effectively control new-generation prostheses for rehabilitation purposes. A HMI has to properly estimate the subject's *motor intention* and provide an adequate device control command for the robot.

The motor intention can be evaluated in a number of ways. A common solution is to determine the current contribution of both subject and assistive device by evaluating the dynamics of the operator together with that of the device itself, in order to estimate the extra support moment has to be given to the joints [53–55]. The major drawback of this HMI is that, to perform a movement, the subject has to be able to at least initiate the movement before they can receive support from the system. Thus, the assistive device is not directly coupled to the operator. In recent years, a number of researches has been conducted on developing HMIs based on the use of biological signals generated by the subject [56–58]. Among others, the two major approaches are based on the Electroencephalographic (EEG) and Electromyographic (EMG) signals.

The first, known as Brain-Machine Interfaces (BMIs) or Brain-Computer Interfaces (BCIs), was defined for the first time by Wolpaw [59], and is able to recognize specific brain patterns and translate them in actual actions of external devices in order to

enable a new real-time interaction between people with severe motor disabilities and the outside world. In this respect, the last years have seen an increase in sophistication of BMI-driven applications [60, 61] that allow direct brain communication even in completely paralysed patients and restoration of movement in paralysed limbs through the transmission of brain signals to the muscles or to external prosthetic devices [62–65]. Evidences from several recent studies suggest also that BMI technology is mature enough to play an active role in the field of motor rehabilitation after stroke [66–69].

Among the different mental tasks and brain signals that have been taken into consideration, most BMI systems share the same architecture. The main components may be divided in: signal acquisition, feature extraction, classification and action generation. Signals are acquired from the user's brain while he/she is performing a predefined mental task (e.g., imagination of hand movement) and those specific features that are supposed to better encode user's intention are extracted. Then, features are classified and translated in an output signal (e.g., posterior probabilities associated to user's intent) by means of machine learning algorithms. Finally, the output of the process is used as a control signal for external devices.

BMIs can be invasive or non-invasive according to the techniques that have been used to record brain signals and, consequently, user's intents. An invasive BMI relies on the activation of single neurons or population of neurons recorded by means of a multi-unit array implanted within the cerebral cortex or its surfaces. These systems directly record the neuronal firing rates or the Local Field Potential (LFP) [70, 71]. Regardless of the several advantages in terms of quality of signals, signal-to-noise ratio and spatial resolution, invasive BMIs suffer from substantial drawbacks related to technical difficulties and clinical risks of a surgical intervention. Contrariwise, non-invasive BMIs decode user's intents from activity recorded at the scalp level. Several non-invasive acquisition techniques have been investigated based on the modulation of both the electrical activity of the brain (i.e., EEG and Magnetoencephalogram (MEG)) and the blood oxygen level (i.e., functional Magnetic Resonance Imaging (fMRI), Near-infrared spectroscopy (NIRS)) [72–74]. The main advantage of these acquisition techniques is that they do not require any kind of surgical intervention. In addition, in the case of EEG and NIRS based BMIs, the system is portable, low cost and it may be setup in a short period both in clinical environment and at a patient's home. The low signal-to-noise ratio and the poor spatial or temporal resolution are the intrinsic disadvantages of such methods. One

of the main challenges in the research field is to employ BMI to catch the user's intention of moving and to naturally control new generation robotic prostheses by bypassing conventional, and easily damaged, activation channels.

The second approach, known as EMG-informed or EMG-driven HMIs, shares a similar architecture to that of BMI from a high level point of view, but is based on the muscle activity. EMG signals measure the electrical currents generated in muscles during contraction, representing neuromuscular activities [75]. They consist of two types: surface EMG, and intramuscular EMG, which are recorded by non-invasive and invasive electrodes, respectively. Currently, surface-detected signals are preferably used to obtain information about the time or intensity of superficial muscle activation [76]. They are emitted prior to muscle contraction and can be detected by superficial non-invasive electrodes. EMG signals appear in lower limb muscles approximately 10 ms before the muscle actually contracts. In the upper limb muscles, delays are between 20 and 80 ms. This is called Electro-Mechanical Delay (EMD) [77, 78]. If the EMD can be exploited in the assistive device control system, the evaluation of the signal can be done by the time muscles contract and a robust coupling between human and robot can be achieved [79, 80]. In this case, since the EMG signals are generated unconsciously, no additional mental load is needed by the subject.

Several comprehensive surveys about its use in modern, multi-DOFs prostheses have appeared, showing that basically all possible electrode arrangements and machine-learning methods have been tried to enable fine control over self-powered prosthesis [81, 82]. However, it turns out that EMG-based HMIs have a number of drawbacks, which still make it challenging. The main problem lies in the inherent noise in electronics equipment, the ambient noise, the motion artifact and its changing nature due to sweat, electrode shift, and fatigue, the latter being especially hard to counter since it entails shifts in the frequency components of the signal as well as in its amplitude [83].

Concluding, beside the architecture of a HMI, the key characteristic is to provide a real-time online feedback in order to maintain the direct connection between user's intent and the generated action. On one side, the feasibility to recognize specific motor intention and on the other, the possibility to learn how to modulate control patterns are the two fundamental aspects of a HMI system. The strict interaction between these two aspects implements the closed-loop approach (i.e., Man-In-The-Loop) where the HMI user may continuously self-regulate his intention / activity according to the provided real-time online feedback. The user can learn the best strategy to operate the HMI.

1.1.3 Robot Control Strategy

As already mentioned, the control of devices by means of an EEG or EMG based HMI suffers from intrinsic limitations such as the number of available commands, the signal reliability and the level of effort for the user. Recently, a new and promising approach has been proposed in order to overtake these drawbacks: a hybrid HMI (hHMI). As a general definition, a hHMI is a combination of different signals including at least one electrophysiological channel (e.g., EEG plus EMG biosignals) [84]. Thus, for example, a user suffering from the progressive loss of muscular activity might control the movement of a robotic arm by means of his residual motor functionalities while he uses his motor imagination only to perform the action. Even more so, all the input channels can be weighted and fused together in order to give a more reliable and robust control signal. Currently, HMI research is moving fast towards a hybrid approach to solve the issue of operating complex devices in natural and daily-life situations. Several examples that adopt such a design have been reported in literature, to control software applications [85, 86], external navigation devices [87] and even new generation neuroprostheses [88]. The achieved results demonstrated that an EEG/EMG driven device is not only attainable but can reach high levels of performance and usability for disables users [89].

In the context of hybrid architecture for HMIs, one of the most promising techniques for operating complex devices is the shared-control approach. The role of shared-control is to contextualize high level commands in the current situation and thus to allow the device to perform a wide range of behaviors with minimum user effort. The concept of shared-control comes from the Human-Computer (Robot) Interaction field and it is based on the so-called H-Metaphor. The H-Metaphor (or Horse-Metaphor) was proposed by Flemish et al. [90] and implements a new design for semi-autonomous vehicles as simple as effective. Imagine you are riding a horse in a wooded park: you need to focus your attention only on the final destination of your journey, or you can even just enjoy the scenery, without caring about the low level navigation details. In fact, you are confident that the horse is intelligent enough to avoid possible obstacles and to follow the correct path. At the same time, you have the full control of your *vehicle*: by means of a simple movement of the *reins*, you can make it turn, stop or move forward. This idea perfectly matches the control limitation of a non-invasive HMI system, that conveys few and high level commands associated to specific tasks performed by the user. In this framework, a EEG/EMG driven device, such as a telepresence robot or a semi-autonomous wheelchair

or even a lower limb exoskeleton, may perform complex behaviors (e.g., moving in real and crowded environment, docking a table, entering a door) by means of a few user's commands. The key point of such a system is the capability of contextualizing the same command according to different situations in order to perform the intended action. Over the last years, shared-control has been widely utilized in HMI applications [63, 91, 92], highlighting that the role of shared-control is twofold: on one hand, it helps disabled users to accomplish the navigation task; on the other, it reduces the workload and allows them to reach similar performances as healthy subjects (i.e., time and number of commands to complete the task).

1.2 Thesis overview

This thesis consists of five chapters.

Chapter 1 - *Introduction* contextualizes the role of the neural and musculoskeletal modeling technology in the biomechanical analysis of the human movement. The aim of this chapter is to identify the most significant results as well as the open challenges within the three main pillars of the Neurorobotics research field.

Chapter 2 - *Contributions and Significance* illustrates the research questions addressed in this thesis, the novelty and limits of this research as well as the significance of the proposed methodologies, providing some possible future perspectives.

Chapter 3 - *Materials and Methods*, illustrates the workflow that goes from the collection of data to the creation of the musculoskeletal model and simulation. The proposed methodology for estimating the musculotendon and joint stiffness during the movement execution is presented. Finally, the design, simulation and prototyping of a small bipedal humanoid robot is described, as well as an Extended Kalman Filter based technique for estimating the ankle damping and stiffness parameters.

Chapter 4 - *Validation Procedures and Results* describes the evaluation techniques and experiments performed to validate the proposed techniques.

Chapter 5 - *Discussion and Conclusion* summarizes the contributions of this research with respect to the state-of-the-art.

Chapter 2

Contributions and Significance

2.1 Research questions to be addressed

This work addresses a number of research questions including:

- The Information Communication Technology (ICT) in the health sector is growing increasingly in the recent years, with particular reference to new-generation protheses, neuromuscular Human-Machine Interfaces (HMI), and EMG-informed / EMG-driven simulation techniques. What is the role of neural and musculoskeletal modeling in neurorehabilitation? (Chapter 1)

- In the last decades, biomechanical models and muscle-driven dynamic simulations have complemented the experimental approaches commonly adopted. With respect to the estimation of physiological and mechanical parameters that cannot be measured experimentally, what are the major open challenges? (Chapter 1, 2)

- By considering the translation of *stiffness classical physics definition* in the context of *human limb joints*, what is the difference between the concepts of *stiffness*, *apparent stiffness* and *quasi-stiffness* in biomechanical analysis? (Chapter 3)

- How do muscle force static and dynamic estimation techniques impact on the musculotendon stiffness and corresponding joint stiffness computation approaches? (Chapter 3)

- By considering the high variability of the surface Electromiographic (EMG) signals, and the inherent difficulties in recording deep muscle activity, is it possible to use a probabilistic approach (i.e., *Gaussian Mixture Models*) to estimate single joint angle using EMG signals? Moreover, is it possible to use an analogous approach to estimate musculotendon stiffness using EMG signals? (Chapter 3, 4)

- By looking at the definition of the *Force-Length-Velocity-Activation* (FLVA) muscle properties, how do muscle force estimates change with respect to different Hill-type based muscle models? (Chapter 3, 4)

- In the context of muscle force optimization solutions, how do muscle force estimates change with respect to different objective functions? (Chapter 3, 4)

- The muscle-driven dynamic simulations often include a set of fictitious actuators (i.e., *Reserve Actuators*) that accounts for the dynamic inconsistencies between kinematic and kinetic data, not resolvable by muscle actuators alone. What are the effects of *Reserve Actuators* on muscle force and joint stiffness optimization solutions? (Chapter 4)

- When studying humanoid robots, many of the processes involving the synthesis of robots' motion have much in common with problems found in biomechanics and human motor-control research. Is it possible to maintain a stable posture during standing, on a humanoid robot, using only a completely passive elastic structure? (Chapter 4)

- By considering the implementation of a hybrid robotic system where the balance of biped is obtained using passive elastic elements, in order to simplify the control of gait, what is the effectiveness on using an Extended Kalman Filter (EKF) as an identification tool for the estimation of damping and stiffness coefficients? (Chapter 4)

- How can a Neuromusculoskeletal (NMS) model be used to provide effective control strategies for powered orthoses and humanoid robots? (Chapter 2, 5)

- Can pattern recognition and machine learning techniques be combined to NMS modeling to provide a better way to extract neuro-motor information from EMG signals? (Chapter 2, 5)

2.2 Novelty of this research

This research work presents a novel NMS model of the human lower limb stiffness that is physiologically accurate and computationally fast (Chapter 3). The proposed computational framework uses EMG signals, Motion Capture (MC) data and Ground Reaction Forces (GRFs) to predict the force developed by 43 musculotendon actuators (Section 3.3). The estimated forces are then used to compute the musculotendon stiffness and the corresponding joint stiffness, clearly differentiating the concepts of *stiffness* from *quasi-stiffness* at multiple Degrees Of Freedom (DOFs) level, within the same joint (Section 3.4). The estimations at each Musculotendon Unit (MTU) is constrained to simultaneously satisfy the joint angles and the joint moments generated with respect to five DOFs, including: Hip Adduction-Abduction (HipAA), Hip Flexion-Extension (HipFE), Hip Internal-External Rotation (HipIER), Knee Flexion-Extension (KneeFE), and Ankle Plantar-Dorsi Flexion (AnklePDF). Advanced methods are used to perform accurate muscle-driven dynamic simulations and to guarantee the dynamic consistency between kinematic and kinetic data. This novel methodologies combine together the physiological accuracy of the state-of-the-art models proposed by the biomechanists, to the fast operation of those proposed by robotics researchers.

This work investigates the impact of different Hill-type based muscle model setups and FLVA properties on the estimation of muscle forces and joint stiffness, as well as the effect of using kinematic constraints in muscle force optimization solutions.

This study presents also the design, simulation and prototyping of a small musculoskeletal humanoid made for replicating the human musculoskeletal structure in an artificial apparatus capable to maintain a quiet standing position using only a completely passive elastic actuation structure (Section 3.6). The prototype has a total mass of about 2 kg and its height is 40 cm. It comprises of four segments for each leg and six DOFs, including: HipAA, HipFE, KneeFE, AnklePDF, Ankle Inversion-Eversion (AnkleIE), and Toe Flexion-Extension (ToeFE). In order to reconstruct the continuous state space parameters proper of the assembly's control of quiet standing, a hybrid non-linear EKF based technique is proposed to combine a base-excited inverted pendulum kinematic model of the robot with the discrete-time position measurements (Subsection 3.6.3).

The objective of this work is to provide effective solutions and readily available software tools to improve the human interaction with robotic assistive devices. This thesis aims

to contribute on advancing research in NMS modeling to better understand the mechanisms of actuation provided by human muscles and the rules that govern the lower limb joint stiffness regulation. The obtained results demonstrate the effectiveness of the proposed techniques, and support the idea of using the NMS modeling technology to address the challenges on the development of musculoskeletal humanoids, new generation HMI, motion control algorithms, and intelligent assistive wearable devices capable to effectively ensure a proper dynamic coupling between human and robot.
As part of the research activity, also a number of software tools have been developed.

- Custom MATLAB and C++ routines were implemented to setting up a development environment capable to import raw data, perform batch processing of movement modeling within OpenSim, and the post-processing of the obtained data within MATLAB in order to estimate joint stiffness and quasi-stiffness.
- A complete model of the robot was implemented within OpenSim and within SimWise 4D.
- Custom MATLAB routines were implemented to process the experimental data related to the robot design and development, as well as for the aforementioned hybrid non-linear EKF identification technique.

The software, C++ implementation and MATLAB routines, will be made freely available to download at `https://bitbucket.org/iaslab-unipd/`.

2.3 Significance of this research

The use of a subject-specific NMS model coupled with machine learning techniques will have a substantial contribution to the design and implementation of robotic exoskeletons and powered orthoses. Indeed, a better understanding of the behavior of muscles can improve the actuation of these devices and their control algorithms, resulting in enhanced biomimetic control systems. Also, the ability to directly study muscles behavior in healthy and impaired people will be readily possible.
The methodology proposed here could be used, in the future, in the context of robotics and neurorehabilitation technologies in conjuction with predictive models of muscle recruitment and modularity for synthetizing the neuromuscular mechanisms underlying

human-like locomotion and adaptation capacity to different terrains in artificial systems such as bipedal robots or prosthetic limbs.

The ability of the proposed methodology to characterize subject-specific and motor task-specific MTU and joint stiffness is critical for sizing wearable robots actuator power and spring stiffness to individual users' joint properties and external mechanical demands. The ability of estimating net joint stiffness could be used in scenarios involving patients with uni-lateral impairments. In this context, stiffness could be estimated from healthy side joints and used as a control signal for compliant prostheses and orthoses acting on the contralateral affected leg so that it mimics (i.e., restores) healthy leg behavior across different locomotion tasks and terrains. The ability of estimating the individual muscle fibers and tendon stiffness could be used to modulate the metabolic cost of locomotion in individuals wearing orthoses. In this context, the orthosis could be controlled so that muscle fibers always operate on the most favorable portion of the FLVA surface. Finally, the ability of translating an individual's EMG activity into muscle and joint stiffness estimates could help understand abnormal stiffness strategies in patients with neurological and orthopaedic conditions in order to deliver personalized rehabilitation treatments that restore physiological properties.

The NMS model can also provide effective solutions for the actuation of humanoid robots that have a musculoskeletal architecture and artificial muscles. The proposed NMS model allows taking inspiration from the way humans move and addressing the challenge of autonomous locomotion in musculoskeletal humanoids. Indeed, a better understanding of the dynamics of muscles during movement will allow designing more sophisticated systems to actuate and control artificial muscles.

This research development aims to integrate musculoskeletal dynamics into robotics systems to achieve more advanced bio-inspired control strategies. Neuromusculoskeletal modeling techniques not only can offer great solutions for exoskeletons control and humanoids actuation, but can also boost research that aims to provide a more realistic estimation of the human internal state.

2.4 Limitations and Future Perspective

There are a number of limitations to this study that should be discussed.

This work was based on a limited number of subjects (i.e., five healthy subjects), using freely available datasets, already employed in other studies with different purposes. Therefore, results may not be completely generalizable. However, this study aimed at developing the theoretical and computational modelling framework for investigating the NMS mechanisms regulating musculotendon and joint stiffness on a subject-specific basis. In this context, every single subject becomes representative. Such a preliminary step needs to be necessarily taken before the developed framework can be applied to large subject populations. Future work will couple the proposed methods with dimensionality reduction techniques, thus enabling characterizing regularities in the neuromuscular control of joint stiffness across large subject population.

Surface EMG only provides a surrogate measurement of the neural drive received by muscles, from which it is currently not possible to discern the underlying afferent and efferent components as well as their contribution to muscle and skeletal joint stiffness regulation. It would be highly speculative to separate the contribution to joint stiffness resulting from EMG-extracted estimates of reflex and descending neural drive. Moreover, for each subject and muscle, the resulting EMG linear envelopes were normalized with respect to the peak-processed values obtained from each recorded trial. Such peak values are relative maximum, not an absolute maximum. This may affect the obtained musculotendon stiffness estimates. However, the problem of surface EMG amplitude estimation is one of the greatest challenges currently open in the field of signal processing. The major problem is the fact that surface EMG is the interference signal resulting from multiple sampled motor unit action potential superimposed in time and frequency. Because of motor unit action potential superimposition, there is in general a non-linearity between the recorded EMG amplitude and the actual muscle activation level. Future work could be employ high-density EMG in conjunction with decomposition techniques to experimentally decode single motor unit action potential and spiking events. In combination with our proposed framework, this could enable identifying the roles of central and peripheral circuitries in the modulation of stiffness.

The proposed methods employed Hill-type muscle models that did not characterize a number of important muscle-tendon force generating mechanisms. Future work will address this limitation by modeling history-dependent muscle force generating mechanisms

including stretch-induced force enhancement and shortening-induced force depression, and by incorporating more realistic damping and force-velocity characteristics as well as muscle energetics characteristics resulting from MTU stiffness modulation.

Finally, with respect to the proposed Locomotive Underactuated Implement Guided via Elastic Elements (L.U.I.G.E.E.), there are two major limitations. First, in order to reduce costs due to fabrication and material, it was designed as a small humanoid robot. Probably, in the future it will be necessary to increase its size in order to include motors, control modules and sensors. Second, the current prototype does not have a real torso and arms. It is well known that these components are essential for maintaining stability during posture and gait in humans. Future works aim to carry on the study by investigating the viscoelastic properties of the whole assembly, by solving the aforementioned limitations, and by introducing motors, control modules and sensors so that this new elastic humanoid robot can move its first steps forward.

In light of the aforementioned limitations, and of the issues discussed about the three pillars of neurorobotics (Chapter 1), it is worth noting that the successful control of neuroprostheses may be achieved only if we are able to correctly detect user's motor intents and to translate them in coherent, natural and ecological actions of the new generation ICT devices. Challenges are open from both theoretical and technological points of view in order to demonstrate that neuroprostheses systems are mature enough to be used in real and daily life situations.

Looking at the characterization of the patient's movement biomechanics, a major challenge is related to the fact that, muscle-tendon forces, joint contact forces and several other physiological parameters are currently not measurable in vivo with non-invasive devices, during motion. Furthermore, often, the measurement system alters the movement of the patient falsifying the measurement itself. Computational modeling of the musculoskeletal system is the only practicable method that can provide an approach to analyze loading of muscle and joint. The development of new modeling methods and numerical simulation algorithms, which are computationally efficient, are increasingly raising the interest in musculoskeletal modeling and simulation among the biomechanical and medical communities.

Considering the modeling of the interaction between patient and orthotics, two critical tasks in process of using personalized models are calibration and validation. Since generic models are constructed from detailed anatomic measurements performed on cadaver specimens, a subject-specific model calibration is needed. Four significant model

calibration steps could be performed in whole or in part to transform a generic model into a personalized model, including: geometric calibration, kinematic calibration, kinetic calibration and neurologic calibration. In this context, validation of clinical predictions is a major challenge faced by personalized models will ultimately require randomized controlled trials, where outcomes are compared between patients whose treatments were planned with a personalized model and those whose treatments were not.

On the other hand, with respect to Human-Machine Interfaces (HMIs), the fundamental requirement is to improve the accessibility, reliability and robustness of such systems in decoding user's intentions. In this respect, biomechanical signals have to be acquired by means of non-invasive techniques while ensuring the quality of the signals. Improvements in the acquisition devices (e.g., amplifier, electrodes) as well as advances in the decoding algorithms are strictly required in order to bring EEG/EMG based HMI system *out-of-the-lab*. As previously mentioned, researchers are currently investigating novel approaches (i.e., hybrid HMIs, shared control theory) to fulfil this ambitious goal. Next challenge is to implement and integrate them in the new generation of prostheses: on one side, a hybrid control of the prostheses that fuses together different kinds of physiological signals (e.g., EEG, EMG, residual muscular functionality) in order to enhance the quality and the naturalness of the control. On the other side, the goal is to improve the Human-Robot Interaction by means of intelligent prostheses able to gather information from the environment, to take autonomous decisions, to adapt its behavior to the musculoskeletal parameters of the user and eventually, to provide him with an haptic and coherent feedback. In this context, the strict coupling between human intention, Brain-Machine Interface and intelligent device will make the prostheses no longer an external actuator, but an actual extension of the user's body.

Chapter 3

Materials and Methods

Despite the detailed subdivision of sections and subsections, which is adopted in order to better clarify the concepts, two major domains can be indentified in this chapter:

1. The description of data and methodologies proposed to study the biomechanics of human movement in order to better quantify the musculotendon and joint stiffness during the movement execution.

2. The description of L.U.I.G.E.E. (Locomotive Underactuated Implement Guided via Elastic Elements). A small humanoid robot, implemented in collaboration with the Mechanical Engineering Department of the Gannon University, Erie, PA, USA, whose actuation structure includes linear elastic springs replicating the major human lower limb muscle groups.

With respect to the first point, the structure of the computational model developed and employed in this thesis has four major components (Fig. 3.1): a) Human Movement (Section 3.1); b) Movement Modeling (Section 3.2); c) Neuromusculoskeletal (NMS) Modeling (Section 3.3); d) Muscle-Tendon Short-Range Stiffness (SRS) (Section 3.4). The experimentally recorded data are elaborated through modules a), b), and c) to estimate the physiological and kinematics data needed to compute the joint stiffness through module d) and joint quasi-stiffness information.
With respect to the second point, the detailed description of the design and implementation of the robot (Section 3.6), as well as of the system state and the joint stiffness estimation techniques (Subsection 3.6.3), proposed as part of this thesis, are provided.

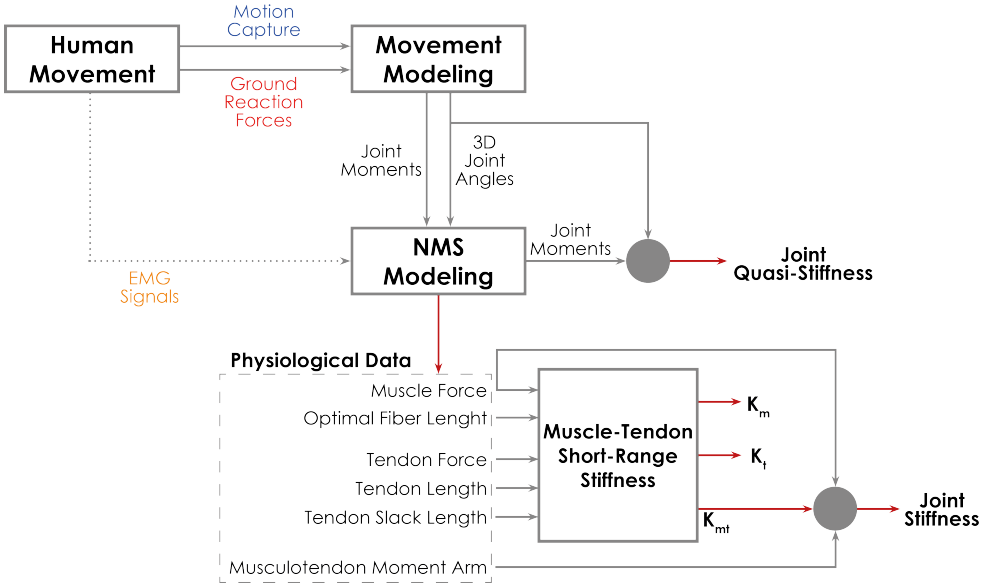

FIGURE 3.1: Flow-chart depicting the proposed multi-DOFs *stiffness* and *quasi-stiffness* computational model. It comprises of four components: a) Human Movement; b) Movement Modeling; c) Neuromusculoskeletal (NMS) Modeling; d) Muscle-Tendon Short-Range Stiffness (SRS). The experimentally recorded data are elaborated through a), b), and c) modules to estimate physiological and kinematics data needed to compute joint stiffness through module d) and joint quasi-stiffness information.

3.1 Human Movement

The *Human Movement* block represents the first step of the workflow. It includes the experimental setup and Motion Capture (MC), Ground Reaction Forces (GRFs), and Electromyographic (EMG) signals recording. In this thesis, two public available dataset were used in which the data from healthy male and female subjects' movements were collected. The raw data, for each subject and trial, were pre-processed in order to remove noise and extract the movements of interest (i.e., stance and swing phases of walking and running) through a custom MATLAB code, as described in Subsections 3.1.1 and 3.1.2, respectively.

3.1.1 Dataset 1: *Multiple Speed Walking Simulations*

The *Multiple Speed Walking Simulations*[1] project includes 32 three-dimensional muscle-actuated simulations of human walking. This dataset was originally recorded in order to quantify the muscle contributions to vertical support and forward progression over a range of walking speeds. Three-dimensional muscle-actuated simulations of gait were

[1] https://simtk.org/home/mspeedwalksims

generated and analyzed for 8 subjects walking overground at 4 different speeds [93]. Protocols for measuring MC, GRFs, and EMG signals are reported in [94]. The GRFs were sampled at 1080 Hz and low-pass filtered at 20 Hz. The EMG data were sampled at 1080 Hz, band-pass filtered between 20 and 400 Hz, rectified, and then low-pass filtered at 10 Hz. The resulting envelope for each muscle was normalized by the peak value recorded from that muscle over all walking speeds for a given subject. The walking speed for each trial was categorized post-hoc as very slow, slow, free, or fast:

$$\text{walking speed} = \begin{cases} 0 < v^* \leq \overline{v}^*_{free} - 3\sigma^*_{free} & \text{very slow} \\ \overline{v}^*_{free} - 3\sigma^*_{free} < v^* \leq \overline{v}^*_{free} - \sigma^*_{free} & \text{slow} \\ \overline{v}^*_{free} - \sigma^*_{free} < v^* \leq \overline{v}^*_{free} + \sigma^*_{free} & \text{free} \\ \overline{v}^*_{free} + \sigma^*_{free} < v^* & \text{fast} \end{cases} \tag{3.1}$$

where $v^* = v/\sqrt{gL_{leg}}$ represents the dimensionaless walking speed, computed from v, the absolute walking velocity, L_{leg}, the leg length, and g, the gravitational acceleration [95]. $\overline{v}^*_{free}$ and σ^*_{free} are the mean and standard deviation, respectively, of the dimensionless free walking speed of the subject cohort reported in [94].

Within this dataset, 4 subjects were selected (age: 13.35 ± 2.11 years; weight: 62.725 ± 16.80 kg; leg length: 0.85 ± 0.0785 m) with similar stature so that the angular velocity of the gait would be comparable among them. However, this producted a non-homogeneous distribution of weight. Hence, the weight of each subject was used as a normalization factor in the computation of physiological and mechanical parameters, as described in Chapter 4. Age, gender, body mass, leg length, and walking speeds of the selected subjects are provided in Table 3.1. For simplicity and clearness, the four speeds have been renamed as follows: very slow *(s1)*, slow *(s2)*, free *(s3)*, and fast *(s4)*.

TABLE 3.1: Subjects' gender, age [years], mass [kg], leg length [m], walking speed [m/s] and simulation label.

Sim Label	**Gender**	**Age [years]**	**Mass [kg]**	**Leg Length [m]**	**Walking Speed [m/s]**			
					s1	**s2**	**s3**	**s4**
GIL01	F	10.2	41.1	0.77	0.57	0.67	1.01	1.40
GIL02	F	14.6	66.0	0.90	0.49	0.80	1.21	1.52
GIL06	F	14.1	81.9	0.81	0.50	0.81	1.11	1.42
GIL08	F	14.5	61.9	0.94	0.56	0.70	1.12	1.62

3.1.2 Dataset 2: *Muscle function of overground running across a range of speeds*

The *Muscle function of overground running across a range of speeds*[2] project is a repository of overground running data along with a working musculoskeletal model to perform simulations and derive the function of individual muscles [96]. The original dataset comprised of nine subjects (five males, four females; age, 27.7 ± 8.0 years; mass, 73.1 ± 8.6 kg; height, 1.76 ± 0.07 m; leg length, 0.93 ± 0.05 m) volunteered to participate in the study. All subjects were experienced runners and at the time of testing were not suffering from any musculoskeletal injury likely to adversely affect their sprinting ability. Prior to data collection, a test leg, henceforth referred to as the ipsilateral leg, was randomly chosen by tossing a coin. All experiments were conducted on a straight indoor synthetic running track. The total track was 110 m long, which provided subjects with up to 60 m to accelerate to a steady-state speed, 20 m to maintain the steady-state speed and 30 m to safely decelerate to rest. All data were collected inside the volume where subjects were required to maintain the steady-state speeds.

Marker-derived kinematic data were acquired using a MC system (VICON, Oxford Metrics, Oxford, UK), by mounting small reflective markers over specific locations on the trunk, legs, and arms. Marker trajectories were recorded using 22 optical infrared cameras sampling at 250 Hz over a distance of 11.5 m. GRFs and Centre Of Pressure (COP) data were measured using eight force plates (Kistler Instrument Corp., Amherst, NY, USA) sampling a 1050 Hz. GRFs were low-pass filtered at 60 Hz, using a fourth-order Butterworth filter to remove high frequency noise. EMG data were sampled at 1500 Hz using a telemetered system (Noraxon Telemyo 2400T G2, Noraxon USA Inc., Scottsdale, AZ, USA). Pairs of Ag/AgCl surface electrodes were mounted, according to the guidelines published in [97], on the skin to measure the activity of 11 lower-limb muscle groups: gluteus maximus, gluteus medius, medial hamstrings (i.e., combined signals from semimembranosus and semitendinosus), lateral hamstrings (i.e., combined signals from biceps femoris long head and short head), rectus femoris, vastus medialis, vastus lateralis, medial gastrocnemius, lateral gastrocnemius, soleus and tibialis anterior.

Within this dataset, the data referred to a healthy male subject (age, 19 years; mass, 75.9 kg; height, 1.82 m; leg length, 1 m), running at four different speeds $s1 = 3.56$ m/s, $s2 = 5.20$ m/s, $s3 = 7.00$ m/s, and $s4 = 9.49$ m/s, were used in the present study.

[2] https://simtk.org/home/runningspeeds

3.2 Movement Modeling

The *Movement Modeling* block (Fig. 3.2) represents the second step of the workflow in which the MC and GRFs data are used to scale the generic musculoskeletal model to the subject-specific anthropometric properties, and to adjust the same in order to reduce the offsets in residual forces and moments. During this step, three-dimensional joint angles and moments are estimated by solving the Inverse Kinematics (IK) and Inverse Dynamics (ID) problems, respectively. The *Movement Modeling* block was implemented based on the use and extensions of OpenSim[3] functionalities through the available Application Programming Interface (API) [33, 98], by developing the C++ custom code needed to perform batch processing of movement within OpenSim.

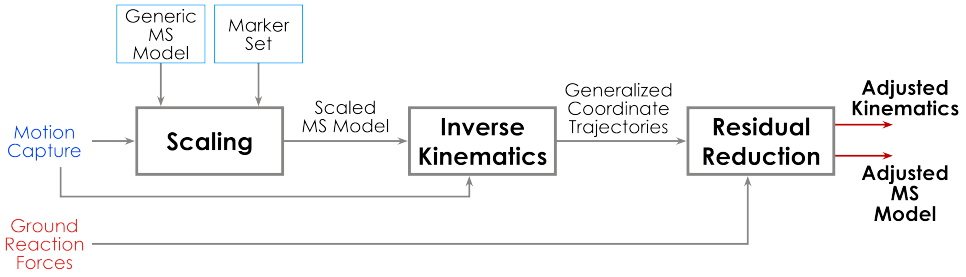

FIGURE 3.2: Movement Modeling. MC data are used to scale a generic musculoskeletal model to a subject-specific anthropometry. The scaled model is then adjusted by including the GRFs within the Residual Reduction Analysis (RRA) in order to guarantee the consistency between kinematic and kinetic data.

3.2.1 Musculoskeletal Model

The adopted musculoskeletal model is described by a three-dimensional, 37 Degrees Of Freedom (DOFs), computer model (Fig. 3.3). The model includes six body segments for each leg: pelvis, femur, tibia-fibula, talus, foot, and toes. Each arm is represented by humerus, ulna, radius, and hand. The joint definition are derived by [99, 100], and the anthropometry by [40]. Ninetytwo Musculotendon Units (MTUs) represent the main muscle groups: 43 for each leg, and 6 lumbar muscles. Muscle lines of action were identical to those in Hamner et al. [101]. The physiological parameters of muscles are in accordance to mean values reported by [102]. The arm joints are actuated by ideal torque motors[4].

[3] https://simtk.org/home/opensim
[4] https://simtk.org/api_docs/opensim/api_docs/classOpenSim_1_1CoordinateActuator.html

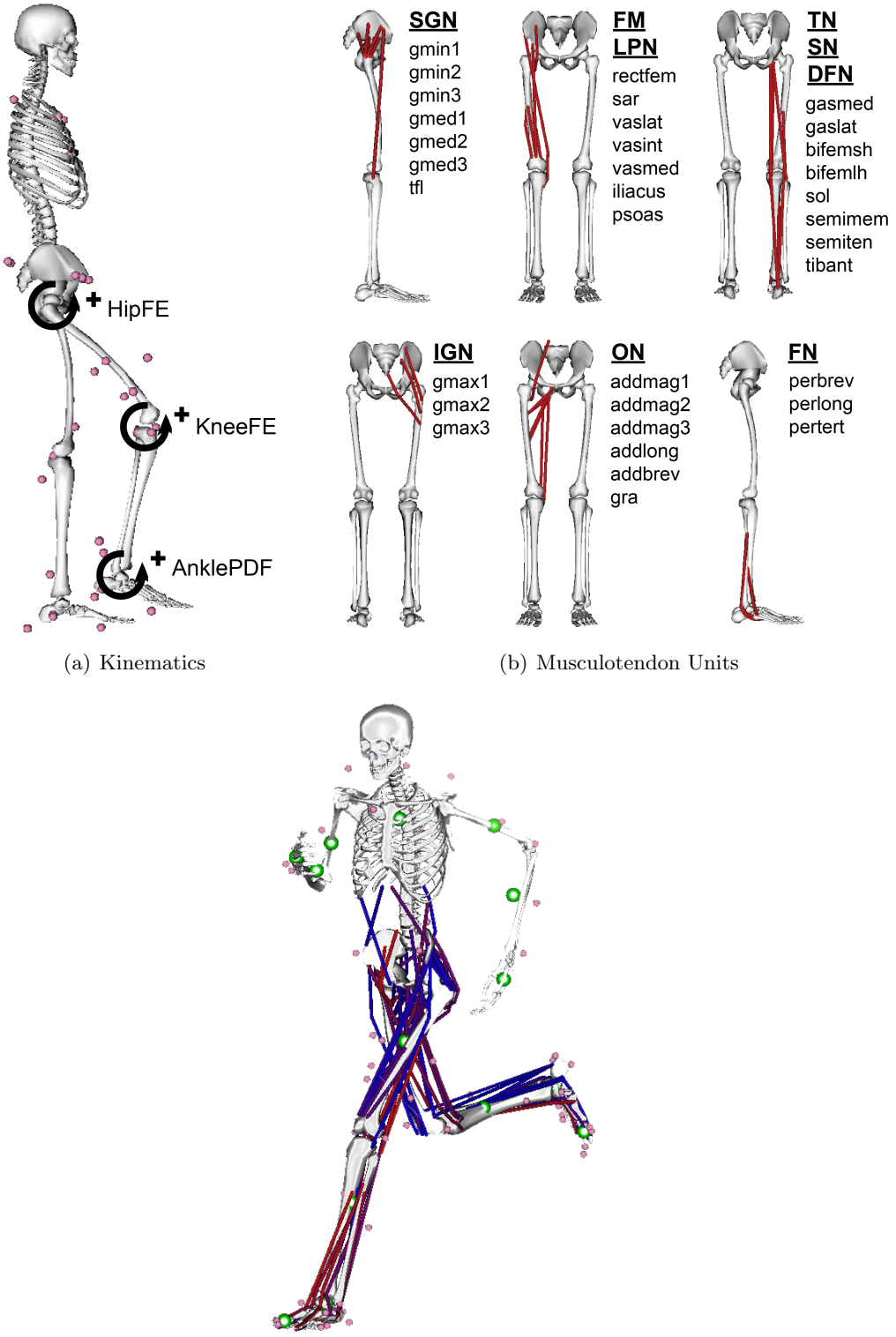

(a) Kinematics

(b) Musculotendon Units

(c) Full-body model

FIGURE 3.3: (A) Adopted skeletal structure with virtual markers position and Hip Flexion-Extension, Knee Flexion-Extension, Ankle Plantar-Dorsi Flexion Degrees of Freedom definition. (B) Adopted Musculotendon Unit defintion and insertion: Superior Gluteal Nerve (SGN), Inferior Gluteal Nerve (IGN), Femoral Nerve (FN) and Lumbar Plexus Nerve (LPN), Obtural Nerve (ON), Tibialis Nerve (TN), Sciatic Nerve (SN), Deep Fibular Nerve (DFN), and Fibular Nerve (FN). (C) Full-body representation of the musculoskeletal model.

3.2.2 Scaling

Scaling is performed based on a combination of measured distances between x-y-z marker locations and manually-specified scale factors. The marker locations are obtained using MC equipment. The unscaled model has a set of virtual markers placed in the same anatomical locations as the experimental markers. The dimensions of each segment in the model are scaled so that the distances between the virtual markers match the distances between the experimental markers. Manual scale factors, which may come from other anthropometric analyses, can also be used as an alternative to the measurement-based scaling for any body segment. Once the dimensions of the segments have been scaled to match the subject, the Scale[5] step were used to move some or all of the virtual markers on the model so that they coincide with the experimental marker locations. The scaling step scales the mass properties (i.e., mass and inertia tensor) of the model, as well as the dimensions of the body segments. Many of the elements attached to the body segments, such as muscle actuators and wrapping objects are also scaled.

3.2.3 Inverse Kinematics

The IK[6] steps through each time frame of experimental data and positions the model in a pose that *best matches* experimental marker and coordinate data for that time step. This *best match* is the pose that minimizes a sum of weighted squared errors of markers and/or coordinates (Eq. 3.2).

$$\min_{q} \left[\sum_{i \in \text{markers}} w_i \| x_i^{exp} - x_i(q) \|^2 + \sum_{j \in \text{unprescribed coords}} \omega_j \left(q_j^{exp} - q_j \right)^2 \right] \tag{3.2}$$
$$q_j = q_j^{exp} \text{ for all prescribed coordinates } j$$

where q is the vector of generalized coordinates being solved for, x_i^{exp} is the experimental position of the i-th marker, $x_i(q)$ is the position of the corresponding marker on the model, and q_j^{exp} is the experimental value for coordinate j. Prescribed coordinates are set to their experimental values. The Least Square Problem (LSP) is solved using a general quadratic programming solver, with a convergence criterion of 0.0001 and a limit of 1000 iterations.

[5] http://simtk-confluence.stanford.edu:8080/display/OpenSim/Scaling
[6] http://simtk-confluence.stanford.edu:8080/display/OpenSim/Inverse+Kinematics

3.2.4 Residual Reduction Analysis

Residual Reduction Analysis (RRA)[7] is a form of forward dynamics simulation that uses a tracking controller to follow model kinematics determined from the IK. However, without muscles the skeleton of the model can be used to determine a mass distribution and joint kinematics that are more consistent with GRFs.

Typically, modeling assumptions, noise, and other erros from MC data lead to dynamic inconsistency, essentially: the GRFs and acceleration estimated from measured marker kinematics for a subject do not satisfy Newton's Second Law, $F = ma$. In RRA, Static Optimization (SO) is utilized to adjust kinematics to reduce the magnitude of residuals (i.e., non-physical forces applied to the model accounting for differences in measured forces and accelerations) from ID. In a separate step the total mass of the model and location of the Centre Of Mass (COM) of a targeted segment (typically the most massive, e.g., torso) are adjusted to eliminate offsets in residual forces and moments.

3.2.5 Inverse Dynamics

The ID[8] determines the generalized forces at each joint responsible for a given movement. Given the kinematics describing the movement of a model and perhaps a portion of the kinetics applied to the model, the ID analysis was performed [103, 104]. Classical mechanics mathematically expresses the mass-dependent relationship between force and acceleration, $F = ma$, with equations of motion.

$$M(q)\ddot{q} + C(q, \dot{q}) + G(q) = \tau \tag{3.3}$$

where, assuming N DOFs, $q, \dot{q}, \ddot{q} \in \mathbb{R}^N$ are the vectors of generalized positions, velocities, and accelerations, respectively, $M(q) \in \mathbb{R}^{N \times N}$ is the system mass matrix, $C(q, \dot{q}) \in \mathbb{R}^N$ is the vector of Coriolis and centrifugal forces, $G(q) \in \mathbb{R}^N$ is the vector of gravitational forces, and $\tau \in \mathbb{R}^N$ is the vector of generalized forces.

The motion of the model is completely defined by the generalized positions, velocities, and accelerations. Consequently, all of the terms on the left-hand side of the equations of motion are known. The remaining term on the right-hand side is unknown. ID solves Eq. 3.3 to yield the net forces and torques at each joint which produce the movement.

[7] http://simtk-confluence.stanford.edu:8080/display/OpenSim/Residual+Reduction+Algorithm
[8] http://simtk-confluence.stanford.edu:8080/display/OpenSim/Inverse+Dynamics

3.2.6 Forward Dynamics

In contrast to ID where the motion of the model was known and we wanted to determine the forces and torques that generated the motion, in Forward Dynamics (FD)[9], a mathematical model describes how coordinates and their velocities change due to applied forces and torques (i.e., moments). From Newton's Second Law, the accelerations of the coordinates can be described in terms of the inertia and forces applied on the skeleton as a set of rigid-bodies.

$$\ddot{q} = [M(q)]^{-1} \{\tau + C(q, \dot{q}) + G(q) + F\} \tag{3.4}$$

where $\ddot{q}$ is the coordinate accelerations due to joint torques, τ, Coriolis and centrifugal forces, $C(q, \dot{q})$, as function of coordinates, q, and their velocities, $\dot{q}$, gravity, $G(q)$, and other forces, F, applied to the model. $[M(q)]^{-1}$ is the inverse of the mass matrix.
In this context, a set of differential equations that model musculoskeletal dynamics can be provided as follows:

$$\begin{aligned} \tau_m &= [R(q)]\, f(a, l, \dot{l}) && \text{Moments due to muscle forces} \\ \dot{l} &= \Lambda(a, l, q, \dot{q}) && \text{Muscle contraction dynamics} \\ \dot{a} &= A(a, x) && \text{Muscle activation dynamics} \end{aligned} \tag{3.5}$$

The net muscle moments, τ_m, are a result of the moment arms, $R(q)$, multiplied by muscle forces, f, which are a function of muscle activation, a, and muscle fiber lengths, l, and velocities, $\dot{l}$. Muscle fiber velocities are governed by muscle contraction dynamics, Λ, which is dependent on the current muscle activations and fiber lengths as well as the coordinates and their velocities. Finally, activation dynamics, A, describes how the activation rates, $\dot{a}$, of the muscles respond to input neural excitations, x, generally termed the model's controls.

[9] http://simtk-confluence.stanford.edu:8080/display/OpenSim/Forward+Dynamics

3.3 Neuromusculoskeletal Modeling

The *Neuromusculoskeletal Modeling* block (Fig. 3.4) represents the third step of the workflow. The three-dimensional joint angles and moments estimated during the previous step are used together with the experimentally recorded EMG signals, within a proper Hill-type based musculotendon model, to estimate the activation and contraction dynamics that determine specific musculotendon forces. Moreover, the musculotendon moment arms are computed for each MTU with respect to each joint in order to determine the musculotendon moments. In this context, the EMG signals were used to iteratively check the estimated muscle activation profiles as a parameter through which evaluate the goodness of the simulation based muscle force recontruction [105].

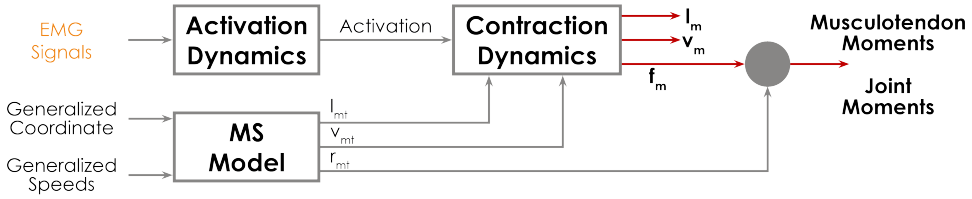

FIGURE 3.4: Neuromusculoskeletal Modeling. The experimentally recorded EMG signals are used to check the estimated activation dynamics for each MTU. The contraction dynamics is then obtained by coupling the activation dynamics with the estimated kinematics. Musculotendon length, l_m, muscle fiber contraction velocity, v_m, and muscle force, f_m are used to compute the musculotendon moments and the corresponding contribution to the total joint moments for each MTU acting on each joint.

The adopted Hill-type MTU model (Fig. 3.5) is known as *Thelen2003Muscle*[10] [106], which represents the muscle mechanical response using five parameters:

1. *Maximum Isometric Force* (MIF), is the peak force that a muscle can produce at its optimal muscle length, and is related to a muscle's cross-sectional area.
2. *Optimal Fiber Length* (OFL), is the length of sarcomeres at which there is optimal overlap of the actin and myosin myofilaments, thus producing a peak force.
3. *Tendon Slack Length* (TSL), is the length over which the tendon develops a force proportional to its strain.
4. *Maximum Contraction Velocity* (MCV), is the maximum speed at which a muscle changes length during a contraction.
5. *Pennation Angle* (PA), is the angle between the tendon and the muscle fibers.

[10] http://simtk-confluence.stanford.edu:8080/display/OpenSim/Thelen+2003+Muscle+Model

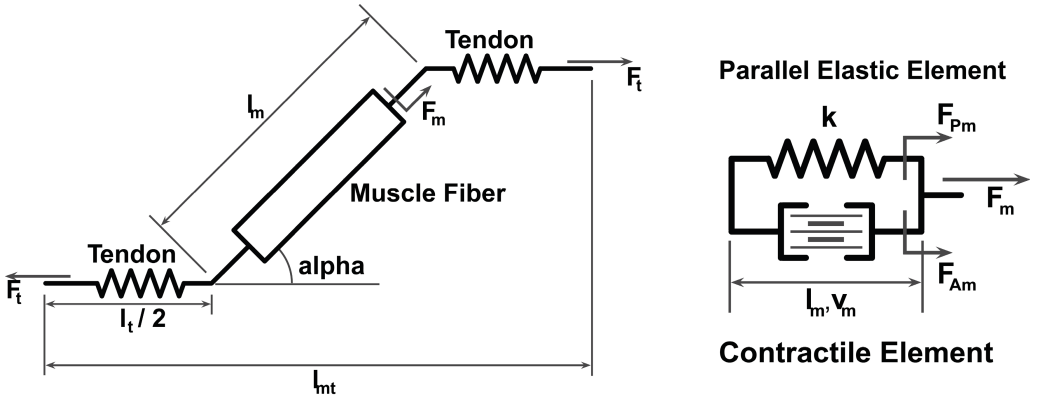

(a) Musculotendon Unit (b) Muscle fibers

FIGURE 3.5: (A) Schematic of muscle-tendon unit showing muscle fiber in series with tendon. The pennation angle, ϕ, of the muscle fiber relative to the tendon and that the total tendon length, l_t, is twice that of the tendon on either end of the muscle fiber, $l_t/2$. (B) Schematic of muscle fiber with contractile element and parallel elastic element. The force produced by the contractile element, F_m, is a function of l_m (muscle fiber length) and v_m (muscle fiber contraction velocity), while the tendon force, F_t, is a function of l_t. The total muscle fiber force, F_m, is the sum of F_{Am} and F_{Pm}.

The muscle have *control* inputs called excitations, and the model represents the Electro-Mechanical Delay (EMD) from these excitations (i.e., the electrical neural signal sent to the motor-neuron junction) to activation (i.e., the level of force production) with a first order differential equation [20, 38]. Using Newton's third law, and assuming that the MTUs are massless, the differential equation of the MTU is:

$$f_{iso}\left(a(t)f_{AL}(l^M)f_v(l^M) + f_{PL}(l^m)\right)\cos(\alpha) - f_{iso}f_{SE}(l^T) = 0 \tag{3.6}$$

Rearranging the above equation and solving for $f_v(l^M)$ yields:

$$f_v(\dot{l}^M) = \frac{\frac{f_{SE}(l^T)}{\cos(\alpha)} - f_{PL}(l^M)}{a(t)f_{AL}(l^M)} \tag{3.7}$$

The Force-Velocity (FV) curve is usually inverted to compute the fiber velocity, as follows:

$$\dot{l}^M = f_v^{-1}\left\{\frac{\frac{f_{SE}(l^T)}{\cos(\alpha)} - f_{PL}(l^M)}{a(t)f_{AL}(l^M)}\right\} \tag{3.8}$$

which is then integrated to simulate the musculotendon dynamics.

In general, the previous equation has four singularity conditions:

1. $a(t) \to 0$
2. $f_{AL}(l^M) \to 0$
3. $\alpha \to 90°$
4. $f_v(\dot{l}^M) \leq 0$ or $f_v(\dot{l}^M) \geq F^m_{len}$

In order to avoid the aforementioned singularities, the adopted implementation is based on the following assumptions:

1. $a(t) \to a_{min} > 0$. The activation dynamic equation smoothly approaches a minimum value that is greater than zero. The time derivative of activation da/dt is computed as follows:
$$\frac{da}{dt} = \frac{u - a}{\tau(u - a)} \tag{3.9}$$
where u is excitation, a is activation, and $\tau(u, a)$ is a variable time constant:
$$\tau(u, a) = \begin{cases} t_{act}(0.5 + 1.5a) & \text{if } u > a \\ t_{deact}/(0.5 + 1.5a) & \text{otherwise} \end{cases} \tag{3.10}$$
Typical values[11] for activation and deactivation time constants, and for the miniminum activation are 10 ms, 40 ms, and 0.01, respectively.
2. $f_{AL}(l^M) \to 0$. The active Force-Length (FL) curve of the Thelen muscle is a Gaussian, which is always greater than 0.
3. $\alpha \to 90°$. This singularity cannot be removed without changing the first equation, and still exists in the present implementation.
4. $f_v(\dot{l}^M) \leq 0$ or $f_v(\dot{l}^M) \geq F^m_{len}$. In order to make the FV curve invertible, the muscle contraction velocity, v^M, is linearly extrapolated when $F^M < 0$ (during a concentric contraction) and when $F^M > 0.95F^m_{len}$ (during an eccentric contraction).
5. A unilateral constraint has been implemented to prevent the fiber from approaching a fiber length that is smaller than 0.01*OFL, or a fiber length that creates a PA greater than the maximum PA specified by the pennation model.

[11] http://simtk-confluence.stanford.edu:8080/display/OpenSim/First-Order+Activation+Dynamics

Given the MTU model, the muscle excitations, activations and corresponding generated forces were computed, within OpenSim, by using two different optimization-based approaches: Static Optimization (SO) and Computed Muscle Control (CMC) [48, 107].
With respect to the SO analysis, the objective function (Eq. 3.11) represents a pure *Torque-based Muscle Force computation procedure* [108]:

$$\begin{aligned} u &= \min \sum_{i=1}^{M} \left(\frac{F_{m,i}}{F^0_{m,i}} \right)^2 \\ \tau_j &= \sum_{i=1}^{M} r_{ij} \times F_{m,i} \qquad \text{i=1,2,...,M; j=1,2,...N} \\ 0 &\leq F_{m,i} \leq F^0_{m,i} \end{aligned} \tag{3.11}$$

where $F_{m,i}$ is the muscle force of the i-th muscle and $F^0_{m,i}$ is the corresponding MIF. r_{ij} is the posture-dependent moment arm for the i-th muscle relative to the j-th joint, and τ_j is the torque about the j-th joint. The sum over M elements corresponds to the number of MTUs crossing the Hip, Knee, and Ankle joint in the model. N is the number of DOFs. The distribution of muscle force is computed for a specific set of joint torques. The cost function is the sum of the squared muscle forces expressed as a fraction of the MIF for each muscle. A set of constraints was considered such that the resulting muscle forces summed to the specific joint torque, and muscle forces were positive and less than or equal to the achievable MIF.
With respect to the CMC analysis, the objective function remains the same of Eq. 3.11, however a significant change is introduced in the muscle activation-to-force condition (see equality contraint ($C_j = 0$) in Eq. 3.12), implementing in this way a kind of *Torque/Kinematic-based Muscle Force computation procedure* [108], as follows:

$$\begin{aligned} u &= \min \sum_{i=1}^{M} \left(\frac{F_{m,i}}{F^0_{m,i}} \right)^2 \\ \tau_j &= \sum_{i=1}^{M} r_{ij} \times F_{m,i} \qquad \text{i=1,2,...,M; j=1,2,...N} \\ 0 &\leq F_{m,i} \leq F^0_{m,i} \\ C_j &= \ddot{q}^*_j - \ddot{q}_j \qquad\qquad \text{j=1,2,...N} \end{aligned} \tag{3.12}$$

where $F_{m,i}$ is the muscle force of the i-th muscle and $F^0_{m,i}$ is the corresponding MIF. r_{ij} is the posture-dependent moment arm for the i-th muscle relative to the j-th joint, and τ_j

is the torque about the j-th joint. The sum over M elements corresponds to the number of MTUs crossing the Hip, Knee, and Ankle joint in the model. N is the number of DOFs. The model accelerations $\ddot{q}_j$ are driven toward the desired accelerations $\ddot{q}_j^*$, where q_j represents the j-th model coordinate. The desired accelerations were computed using the following Proportional-Derivative (PD) control law:

$$\ddot{\vec{q}}^*(t+T) = \ddot{\vec{q}}_{exp}(t+T) + \vec{k}_v[\dot{\vec{q}}_{exp}(t) - \dot{\vec{q}}(t)] + \vec{k}_p[\vec{q}_{exp}(t) - \vec{q}(t)] \tag{3.13}$$

where $\vec{q}_{exp}$ are the experimentally-derived coordinates, $\ddot{\vec{q}}^*$ are the desired accelerations, and $\vec{q}$ are the model coordinates. $\vec{k}_v = 30$ and $\vec{k}_p = 900$ are the feedback gains on velocity and position errors, which were experimentally set. It is worth noting that, in both Eq. 3.11 and Eq. 3.12, the muscle activation $a_{m,i} = F_{m,i}/F^0_{m,i}$ always varies between 0 and 1. The optimization problem formulated in Eq. 3.12 was solved by considering musculotendon actuators as *ideal* force generator, and by taking into account the physiological Force-Length-Velocity (FLV) relationship (Fig. 3.6) that characterizes each MTU [109]: $F_{m,i} = a_{m,i} f\left(F^0_{m,i}, l_{m,i}, v_{m,i}\right)$.

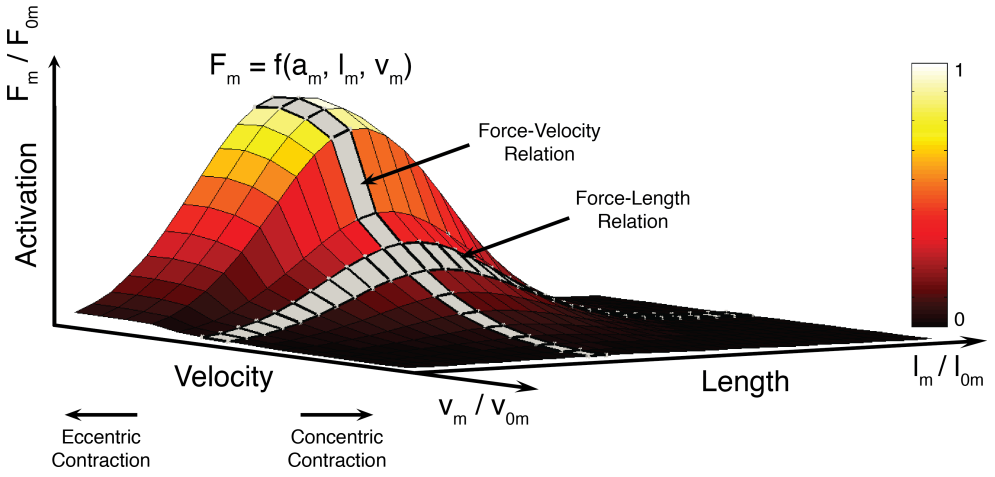

FIGURE 3.6: The Active Force-Length-Velocity (FLV) surface of muscle is defined by the muscle's Optimal Fiber Length (OFL), Maximum Shortening Velocity (MSV), and Maximum Isometric Force (MIF). Active muscle force generation can be constrained to this surface and scaled by the level of muscle activation. Force-Length and Force-Velocity curves are highlighted in gray.

To compensate for the residual forces that account for dynamic inconsistencies between kinematic and kinetic data, a set of reserve actuators were introduced [110]. These fictitious actuators account for forces the model could not resolve with musculotendon actuators alone. Here, five different sets of reserve actuators were considered (Table 3.2)

in order to better assess the impact of these actuation contributions in the muscle force optimization process.

TABLE 3.2: Values of Reserve Actuators Maximum Generable Force (i.e., labeled as r5, r10, r20, r40, r80) for each Degrees of Freedom (DOF). Adopted Actuator Types are Point Actuator (PA), Torque Actuator (TA), and Coordinate Actuator (CA).

DOFs	**Maximum Generable Force**					**Act**
	r5	**r10**	**r20**	**r40**	**r80**	**Type**
FX, FY, FZ [N]	2000	2000	2000	2000	2000	PA
MX, MY, MZ [Nm]	2000	2000	2000	2000	2000	TA
HipFE, AA, Rot [Nm]	5	10	20	40	80	CA
KneeFE [Nm]	5	10	20	40	80	CA
AnklePDF [Nm]	5	10	20	40	80	CA
Subtalar [Nm]	5	10	20	40	80	CA
Mtp [Nm]	5	10	20	40	80	CA
Lumb Ext, Bend, Rot [Nm]	100	100	100	100	100	CA
Arm [Nm]	1000	1000	1000	1000	1000	CA

3.4 Joint Stiffness Estimation

The *Joint Stiffness Estimation* block (Fig. 3.7) represents the fourth step of the workflow. It was implemented through a set of custom MATLAB routines, that post-process the physiological and geometric parameters estimated within the aforementioned blocks, to provide a physiologically consistent representation of the mechanisms regulating multi-joint *stiffness* and *quasi-stiffness* during the locomotion.

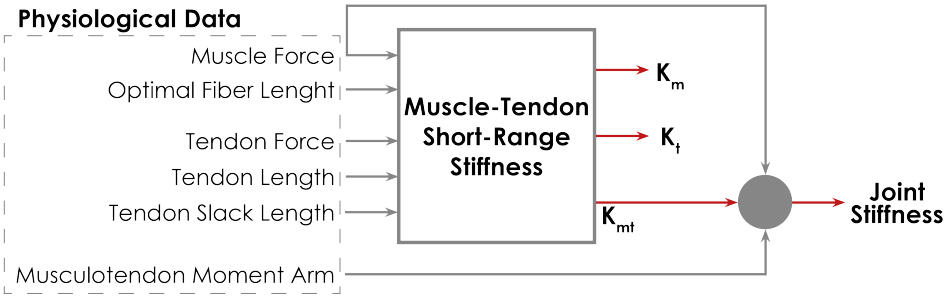

FIGURE 3.7: Muscle-Tendon Short-Range Stiffness computational model. The physiological and geometrical parameters (i.e., Muscle and Tendon Forces, Tendon Length, and Musculotendon Moment Arms) estimated in the Neuromusculoskeletal Modeling block are used together with model parameters (i.e., Optimal Fiber Length and Tendon Slack Length) to compute the Musculotendon Stiffness and the corresponding Joint Stiffness.

3.4.1 Quasi-Stiffness and Passive Motion

Often, *quasi-stiffness* and *stiffness* are inaccurately used interchangeably. Yet, they are separate concepts, except for when the joint is constrained to be passive around a fixed equilibrium position and in quasi-static conditions. *Quasi-stiffness* is strongly related with the use of Kinematic Networks (K-nets) [111] and the concept of the Passive Motion Paradigm (PMP) [112]. Considering the stance phase during the human locomotion, the whole body can be represented as an open kinematic chain, where the body's Center of Gravity (COG) needs to follow a pre-planned trajectory. By using the PMP it is possible to relate the trajectory of the COG in the Cartesian Space (CS) with the torque at the joints via an elastic field associated with a time-varying *quasi-stiffness*. Hence, the general dynamic equation (Eq. 3.3) can be rewritten in the following form:

$$M(\theta)\ddot{\theta} + C(\theta, \dot{\theta}) + G(\theta) = \Theta K_{qs}(t) \tag{3.14}$$

where $M(\theta, t)$ and $C(\theta, \dot{\theta})$ are the inertial and Coriolis matrices [8], θ is the vector of joint angles $[\theta_1, \theta_2, ..., \theta_n]^T$, $G(\theta)$ is a vector of torques representing the contribution of gravity to each joint, Θ is a diagonal matrix of angles θ_i and K_{qs} is the vector of joint *quasi-stiffness* so that the vector of joint torques is equal to:

$$\tau = \Theta K_{qs}(t) = \begin{bmatrix} \theta_1 & 0 & 0 \\ 0 & \ddots & 0 \\ 0 & 0 & \theta_n \end{bmatrix} \begin{bmatrix} K_{qs,1} \\ \vdots \\ K_{qs,n} \end{bmatrix} \tag{3.15}$$

The *quasi-stiffness* vector $K_{qs}(t)$ can be thought as a set of *virtual springs* with time varying characteristics positioned at the joint level, where each joint is independently controlled. Given an initial, fixed, reference position and an initial load, a change in *quasi-stiffness* moves the joint angles θ to a new equilibrium position. Eq. 3.14 is representative of an open loop system where the torque is imposed indirectly via an elastic field (Eq. 3.15). It is immediate to see that given the dependency of $M(\theta, t)$ and $C(\theta, \dot{\theta})$ from θ and $\dot{\theta}$, the control of the trajectory becomes highly non-linear.

3.4.2 Stiffness and Feedback Linearization

The basic idea of feedback linearization is to construct a control law to cancel all nonlinearities of a nonlinear dynamical system via full-state nonlinear feedback, allowing traditional linear control techniques to be easily implemented on the nonlinear system [113]. In contrast to *quasi-stiffness*, K_{qs}, the term *stiffness*, K_j, represents the parameter that generates a position dependent reaction force when a deviation of the limb from the intended trajectory occurs. To meet the trajectory tracking requirement, let us consider a simple proportional controller. Let $\theta_d(t)$, $\dot{\theta}_d(t)$ and $\ddot{\theta}_d(t)$ be representatives of the desired trajectory, while defining the error between the actual and desired trajectory as

$$e(t) = \theta_d(t) - \theta(t) \tag{3.16}$$

Let

$$\begin{aligned} \omega_j^2 &= diag(M^{-1}K_j) \\ \ddot{e}(t) + \omega_j^2 e(t) &= 0 \end{aligned} \tag{3.17}$$

be the resonance frequency, ω_j^2, of the system, and the relationship between the resonance frequency and the trajectory error. Eq. 3.16 and Eq. 3.17 can be equivalently rewritten in the following form:

$$\begin{aligned} \ddot{\theta} &= \ddot{\theta}_d - \ddot{e}(t) \\ \ddot{e}(t) &= -\omega_j^2 e(t) \end{aligned} \tag{3.18}$$

By substituting Eq. 3.18 in the left hand side of Eq. 3.14, and solving for $K_{qs}(t)$ we have the control input:

$$K_{qs}(t) = \Theta^{-1}\left[M(\theta)\left(\ddot{\theta}_d + \omega_j^2 e(t)\right) + C(\theta, \dot{\theta}) + G(\theta)\right] \tag{3.19}$$

Hence, substituting Eq. 3.19 on the right hand side of Eq. 3.14 we obtain:

$$\begin{aligned} M(\theta)\left[\left(\ddot{\theta}_d - \ddot{\theta}\right) + \omega_j^2 e(t)\right] &= 0 \\ M(\theta)\left[\ddot{e}(t) + \omega_j^2 e(t)\right] &= 0 \end{aligned} \tag{3.20}$$

Since the inertial matrix, M, is positive definite, from Eq. 3.20, considering the relationship between the resonance frequency and the joint stiffness [114]:

$$\omega_j = \sqrt{\frac{K_j}{M}} \tag{3.21}$$

we obtain the linear differential equation that governs the error between the actual and desired trajectories, as follows, with $\xi = 1/M$:

$$\ddot{e}(t) + \xi K_j e(t) = 0 \tag{3.22}$$

3.4.3 Stiffness vs Quasi-Stiffness

When comparing Eq. 3.22 with Eq. 3.14 we can observe that *quasi-stiffness* K_{qs} and *stiffness* K_j have two different reference points (Fig. 3.8). *Stiffness* generates a position dependent torque variation that aims at bringing the limb back to the intended trajectory if a disturbance occurs. Conversely, *quasi-stiffness* represents the gain to be applied to the angular position to obtain the torque necessary for the movement. Furthermore, the *stiffness* reference point changes in time, moving synchronously with the intended trajectory. Instead, the *quasi-stiffness* reference point is a fixed angular position in space, usually referred as the angle that the joints assume during quiet standing.

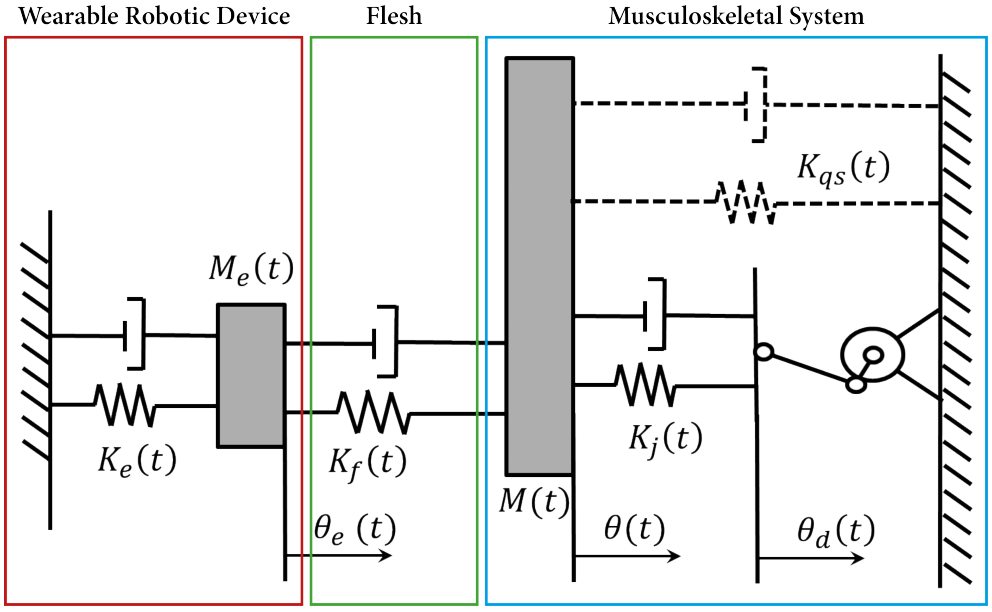

FIGURE 3.8: Mechanical schematics of a plausible interaction between a human limb and a wearable robot device. M_e and K_e are the inertia and stiffness of the environment; K_f represents the stiffness coefficient of the flesh (i.e., tissue); M, K_j, and K_{qs} are the inertia, stiffness, and quasi-stiffness of the human musculoskeletal system.

By assuming the previously described mechanical and control model, the joint *quasi-stiffness* was computed from the slope of the torque-angle relationship performing an ID analysis. On the other hand, the *stiffness* estimation was performed by implementing a Short-Range Stiffness (SRS) model-based approach inspired to previous studies of the

upper [115] and lower limb [29]. The SRS of each MTU (i.e., i=1,2,...,M), $K_{mt,i}$ (Eq. 3.23), results from the *stiffness* of the muscle fibers, $K_{m,i}$ (Eq. 3.24), in series with the *stiffness* of the tendon, $K_{t,i}$ (Eq. 3.25).

$$K_{mt,i} = \frac{K_{m,i}K_{t,i}}{K_{m,i} + K_{t,i}} \quad \text{i=1,2,...,M} \tag{3.23}$$

where $K_{m,i}$ is a function of muscle force, $F_{m,i}$, muscle OFL, $l^0_{m,i}$, and of a dimensionless scaling constant [116, 117], λ, as follows:

$$K_{m,i} = \frac{\lambda F_{m,i}}{l^0_{m,i}} \quad \text{i=1,2,...,M} \tag{3.24}$$

$K_{t,i}$ is function of the tendon force, $F_{t,i}$, and of the effective tendon elongation given by the difference between the instantaneous tendon length, $l_{t,i}$, and the TSL, $l^s_{t,i}$ [115, 116].

$$K_{t,i} = \frac{F_{t,i}}{l_{t,i} - l^s_{t,i}} \quad \text{i=1,2,...,M} \tag{3.25}$$

It should be stressed that Eq. 3.25 was derived as follows. For simplicity, here the index i is omitted. Let

$$\begin{aligned} \sigma = E\epsilon = \frac{F_t}{A_t} \qquad & \text{Tendon Strength} \\ \epsilon = \frac{l_t - l^s_t}{l^s_t} \qquad & \text{Tendon Strain} \end{aligned} \tag{3.26}$$

and, assuming that the tendon behaves like purely elastic bar,

$$K_t = \frac{E_t A_t}{l_t} \tag{3.27}$$

be an equivalent definition of tendon stiffness, where E_t is the tendon elastic module (i.e., Young's Modulus), A_t is the tendon Cross-Sectional Area (tCSA), and l_t is the effective tendon length. By sustituting Eq. 3.26 in Eq. 3.27 we obtain:

$$\begin{aligned} E &= \frac{\sigma}{\epsilon} = \frac{F_t}{A_t\epsilon} = \frac{F_t l_t}{A_t\epsilon} \\ K_t &= \frac{E_t A_t}{l_t} = \frac{F_t \cancel{l_t}}{\cancel{A_t}\epsilon} \cdot \frac{\cancel{A_t}}{\cancel{l_t}} = \frac{F_t}{l_t - l^s_t} \end{aligned} \tag{3.28}$$

that is exactly Eq. 3.25. This formulation can lead to singularities as the current length of the tendon is equal to the TSL. However, such singularities were solved by considering the tendon stiffness only when the tendon length is greater than the TSL, in accordance

with the fact that the force varies with the strain only when the tendon length is greater than the TSL; otherwise the tendon force is zero [38].

The corresponding aforementioned joint *stiffness* K_j (Eq. 3.29) results as function of $K_{mt,i}$, the vector θ describing the joint angles, and of the moment arms of each MTU about each joint.

$$K_j = J^T \tilde{K} J + \frac{\partial J^T}{\partial \theta} \overrightarrow{F}_m \tag{3.29}$$

where $\tilde{K}$ is a diagonal matrix in which the non-zero elements represent the *stiffness* for each MTU in the model, and $\overrightarrow{F}_m$ is the vector of muscle forces. J is the Jacobian matrix relating changes in joint angles to changes in muscle length (i.e., muscle moment arms) [118]. The second term in Eq. 3.29 accounts for how angle dependent changes in muscle moment arms influence joint *stiffness*.

3.5 Gaussian Mixture Model based estimation of musculotendon stiffness

To better reproduce human behaviors using robots, the latter must be endowed with learning capabilities enabling them to acquire new knowledge from human examples. Most works have focused on developing learning algorithms to encode trajectories using vision or kinesthetic systems to capture the teacher demonstrations (i.e., Learning from Demonstration) [119]. Nevertheless, the new variable impedance capabilities of recent robotic devices demand to reformulate these methods in order to exploit their new control schemes in performing more complex tasks. Thus, to deepen our understanding and be able to model human-robot interaction we have to search for new approaches. Such methodologies should allow for the description of the uncertainty related to the measurement of the human physiological parameters, and for those variables that cannot be measured in-vivo. These techniques must capture the basis of human features so to adapt what has been learned by the robot to new tasks. Hence, the objective is not to replicate exactly what humans do, but to formalize the underlining rules to control the task. To this end, the aim of this section is to describe a preliminary study conducted to estimate the muscle-tendon stiffness of human lower limb during the execution of a normal gait cycle, using a Gaussian Mixture Model (GMM) probabilistic approach [120]. A GMM is a parametric probability density function represented as a weighted

sum of Gaussian component densities. GMM parameters are commonly estimated from training data by using the iterative Expectation-Maximization (EM) algorithm [121] or Maximum A Posteriori (MAP) estimation [122] from a well-trained prior model.
Time-dependent geometrical and inertial data came from the observation of each subject during the execution of the walking movement carried out at different speeds (Subsection 3.1.1). At each instant, the behaviors of the i-th muscle of one leg ($i = 1, 2, .., M$) were defined as the set $\zeta^i = \{\tau, K_{mt}\} \in \mathbb{R}^D$, where $D = 2$ is the dimensionality of the system. Each behavior was approximated by the sum of G Gaussian components. The parameter K_{mt} (Eq. 3.23) was estimated as a function of the time by means of the probability density function described in Eq. 3.30.

$$p\left(\zeta^i\right) = \sum_{g=1}^{G} \pi_g \mathcal{N}\left(\zeta^i; \mu_g, \Sigma_g\right) \tag{3.30}$$

where π_g are priors probabilities, and $\mathcal{N}\left(\zeta^i; \mu_g, \Sigma_g\right)$ represents a set of Gaussian distributions defined by μ_g and Σ_g, respectively mean vector and covariance matrix of the g-th distribution.
The EM algorithm was iterated to estimate the optimal parameters $\phi^i = \left(\pi_g^i, \mu_g^i, \Sigma_g^i\right)$ for each mixture. The algorithm can be separated in two cyclic phases: expectation and maximization. Naming n the number of trials used to train the model, and T the number of observations acquired during each trial, the toal number of data samples is $N = nT$. The iteration stops when the increase of the log-likelihood $\mathcal{L} = \sum_{j=1}^{N} \log\left[p\left(\zeta_j^i | \varphi^i\right)\right]$ at each iteration becomes smaller than a defined threshold δ, given by $\frac{\mathcal{L}(t+1)}{\mathcal{L}(t)} < \delta$. The algorithm optimizes the parameters of the G Gaussian components by maintaining a monotone increasing likelihood during the local search of the maximum. The Bayesian Information Criteria (BIC) [123] was used to estimate the number of mixtures G, as reported in Eq. 3.31.

$$S_{BIC} = -2\mathcal{L} + n_p \log N \tag{3.31}$$

where $n_p = (G-1) + G\left(D + 1/2D(D+1)\right)$ is the number of free parameters required for a mixture of G components with full covariance matrix. The log-likelihood measures how well the model fits the data, while the second term aims to avoid data over-fitting to keep the model general. An approximated value of K_{mt} was estimated by using the Gaussian Mixture Regression (GMR). The conditional expectation of human muscle-tendon stiffness, K_{mt}, was computed starting from the consecutive values τ, known a

priori. This means that the muscle-tendon stiffness was directly related to the time instant τ. The model was trained by considering how the muscle-tendon stiffness (computed using the analytical formulation provided in Subsection 3.4.3) change during a specific walking movement, executed at four different speeds. A Gaussian component g was defined by the parameters (π_g, μ_g, Σ_g), with means and covariance matrix so that:

$$\begin{aligned} \mu_g &= \{\mu_{\tau,g}, \mu_{K,g}\} \\ \Sigma_g &= \begin{bmatrix} \Sigma_{\tau,g} & \Sigma_{\tau K,g} \\ \Sigma_{K\tau,g} & \Sigma_{K,g} \end{bmatrix} \end{aligned} \tag{3.32}$$

The conditional expectation and its covariance was estimated using Eq. 3.33:

$$\begin{aligned} \widehat{K}_{mt} &= E[K_{mt}|\tau] = \sum_{g=1}^{G} \beta_g \widehat{K}_{mt,g} \\ \widehat{\Sigma}_K &= Cov[K_{mt}|\tau] = \sum_{g=1}^{G} \beta_g^2 \widehat{\Sigma}_{K,g} \end{aligned} \tag{3.33}$$

where β_g is the weight of the g-th Gaussian component through the mixture, $\widehat{K}_{mt,g}$ is the conditional expectation of $K_{mt,g}$ given τ, and $\widehat{\Sigma}_{K,g}$ is the conditional covariance of $K_{mt,g}$ given τ, defined as follows:

$$\begin{aligned} \beta_g &= \frac{\pi_g \mathcal{N}(\tau|\mu_{\tau,g}, \Sigma_{\tau,g})}{\sum_{g=1}^{G} \mathcal{N}(\tau|\mu_{\tau,g}, \Sigma_{\tau,g})} \\ \widehat{K}_{mt,g} &= E[K_{mt,g}|\tau] = \mu_{K,g} + \Sigma_{K_\tau,g} (\Sigma_{\tau,g})^{-1} (\tau - \mu_{\tau,g}) \\ \widehat{\Sigma}_{K,g} &= Cov[K_{mt,g}|\tau] = \Sigma_{K,g} + \Sigma_{K_\tau,g} (\Sigma_{\tau,g})^{-1} \Sigma_{\tau K,g} \end{aligned} \tag{3.34}$$

Thus, the generalized form of the behaviors $\widehat{\zeta^i} = \{\tau, K_{mt}\}$ was generated by keeping in memory only the means and covariance matrices of the Gaussian components calculated through the GMM. In this way, the computational load was minimized, not having to compute every time the Gaussians.

3.6 Locomotive Underactuated Implement Guided via Elastic Elements (L.U.I.G.E.E.)

Humanoid robotics offers a unique research tool for understanding the human brain and body. Human body representations have been used for centuries to help in understanding and documenting the shape and function of its compounding parts. Since the Da Vinci drawings, human body atlases have evolved significantly and can nowadays describe the human anatomy with great precision, using multi-level biological scales spanning multiple dimensions. In parallel, the body physiology, its systems and their functions, the mechanisms of human motion, the pathological and healing processes are among the many topics being studied and described in different domains of science.
The synthesis of human motion is a complex procedure that involves accurate reconstruction of movement sequences, modeling of musculoskeletal kinematics, dynamics and actuation, and characterization of reliable performance criteria. Many of these processes have much in common with the problems found in robotics research. It is clear that these human-friendly robots will look very different than today's industrial robots and generating coordinated natural motion in human-like robotic structures has proved to be a challenging task. Moreover, the characterization and control of humanoid systems has also an impact beyond robotics. It can provide the support to understand biological functions of the human body (biomechanics), tools to design machines and spaces where humans operate (ergonomics), simulation environments to study the effects of musculoskeletal alterations (surgical simulation), to design and study rehabilitation systems, and support to synthesize realistic computer animations.

3.6.1 Background and motivation

The proposed assembly is a bio-inspired four-segmented underactuated bipedal robot, originally inspired to the *Jena Walker II*[12] [124], and *BioBiped1*[13] [125]. The total mass of the implement is about 2 kg and its height is about 40 cm. Previous studies have implemented the apparatus in virtual simulation environment [126] developing a prototype for simulating human walking [127] and testing an impedance-based control approach for driving the mechanism to imitate human gait [128].

[12] http://lauflabor.ifs-tud.de/doku.php?id=projects:projects_biped_robots
[13] http://www.biobiped.de/index/

In this thesis, the design and prototype was improved in order make a robot capable to maintain a quiet standing posture using only a completely passive actuation structure. Furthermore, the reconstruction of the continuous-time state space parameters proper of the assembly's control of quiet standing was also investigated [129]. The reconstruction was based on a hybrid non-linear Extended Kalman Filter (EKF) in order to combine a base-excited inverted pendulum kinematic model of the robot with the discrete-time position measurements.

The position of the robot COM was measured using the Tracker Video Analysis and Modeling Tool[14] from a web-camera recording [130]. The modeling and simulation phases were conducted in two stages by using OpenSim and SimWise 4D[15]. The former is the aforementioned freely available, user extensible software system that lets users develop models of human musculoskeletal structures and create dynamic simulations of movement. The latter is a proprietary solution for design and engineering professionals developing products involving assemblies of three-dimensional parts. The two multi-body dynamics simulation environments were used to define an effective human-like skeletal structure, and to determine the spring stiffness positioning and natural lengths adopting a top-down heuristic approach.

3.6.2 Design and prototyping

The simulated model and the corresponding prototype comprise of four segments for each leg: thigh, shank, foot and toes, plus one body segment called waist, which represents with its COM and dimensions the upper part of the skeleton. Table 3.3 provides the volume, mass and dimensions of the principal robot body parts.

Each leg has a total of 6 DOFs (Fig. 3.9):

- *Hip Flexion-Extension* (HipFE) and *Hip AdductionAbduction* (HipAA) obtained a universal joint;
- *Knee Flexion-Extension* (KneeFE) implemented via a single DOF revolute joint allowing the rotation of the shank with respect to the thigh;
- *Ankle Plantar-Dorsi Flexion* (AnklePDF) and *Ankle Inversion-Eversion* (AnkleIE) implemented coupling two single DOF revolute joints;

[14] http://www.opensourcephysics.org/items/detail.cfm?ID=7365
[15] https://www.design-simulation.com/SimWise4d/index.php

- *Toe Flexion-Extension* (ToeFE) given by a single rotational DOF, and needed to accomodate the movement of the foot with respect to the ground.

TABLE 3.3: Robot bodies name, volume, mass and dimensions. Hip and Ankle represent the blocks that interconect the waist to the thigs and the shanks to the feet.

Body Name	**Volume [mm^3]**	**Weight [kg]**	**Width (X) [mm]**	**Length (Y) [mm]**	**Height (Z) [mm]**
Waist	2.22 e+5	0.231	150	102	99
Hip	5.89 e+4	0.061	42	67	81
Thigh	7.66 e+4	0.079	54	150	42
Shank	7.08 e+4	0.074	54	142	54
Ankle	3.28 e+4	0.034	42	50	41
Foot	2.81 e+4	0.029	48	104	46
Toe	1.61 e+4	0.019	50	48	27

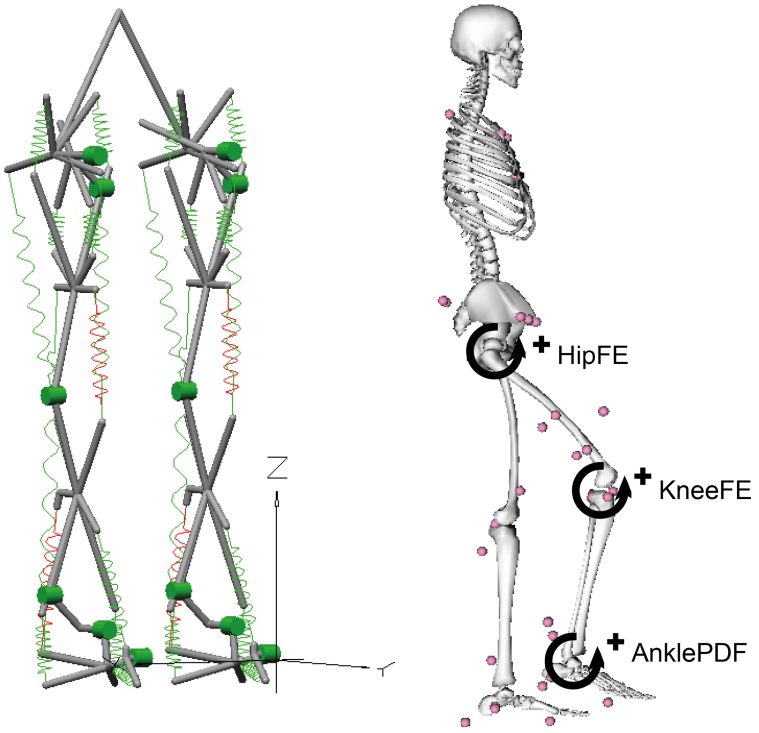

FIGURE 3.9: On the left hand-side, the kinematic structure of the robot and the definition of the available Degrees Of Freedom (DOFs; i.e., green cylinders). On the right hand-side, the corresponding tree major DOFs (i.e., Hip Flexion-Extension, HipFE; Knee Flexion-Extension, KneeFE; Ankle Plantar-Dorsi Flexion, AnklePDF) along the sagittal plane considered in the human model.

In this study, the assembly is completely passive. Thirteen linear springs (Fig. 3.10 and Table 3.4) were inserted according to the position of the major muscle groups as depicted in Fig. 3.11.

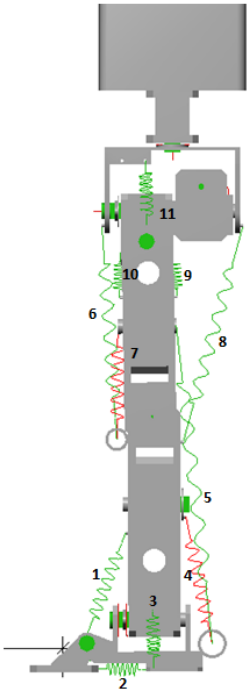

FIGURE 3.10: Positioning of springs.

ID	Path	Length [mm]	K [N/mm]
1	Ankle Bracket - Shank	63.5	0.305
2	Toe - Ankle Bracket	25.4	0.228
3	Shank - Ankle Bracket	38.1	0.525
4	Ankle Bracket - Shank	69.9	0.223
5	Thigh - Ankle Bracket	127.0	0.715
6	Shank - Hip Bracket	114.3	0.441
7	Shank - Thigh	76.2	0.543
8	Shank - Hip Bracket	152.4	0.072
9	Thigh - Hip Swing Arm	25.4	0.531
10	Thigh - Hip Swing Arm	25.4	0.531
11	Hip Bracket - Hip Swing Arm	38.1	0.525
12	Hip Bracket - Hip Swing Arm	38.1	0.525
13	Shank - Ankle Bracket	38.1	0.525

TABLE 3.4: ID and path (i.e., attachment and insertion bodies) of each spring. The lengths [mm] and stiffness coefficients [N/mm] values of each spring.

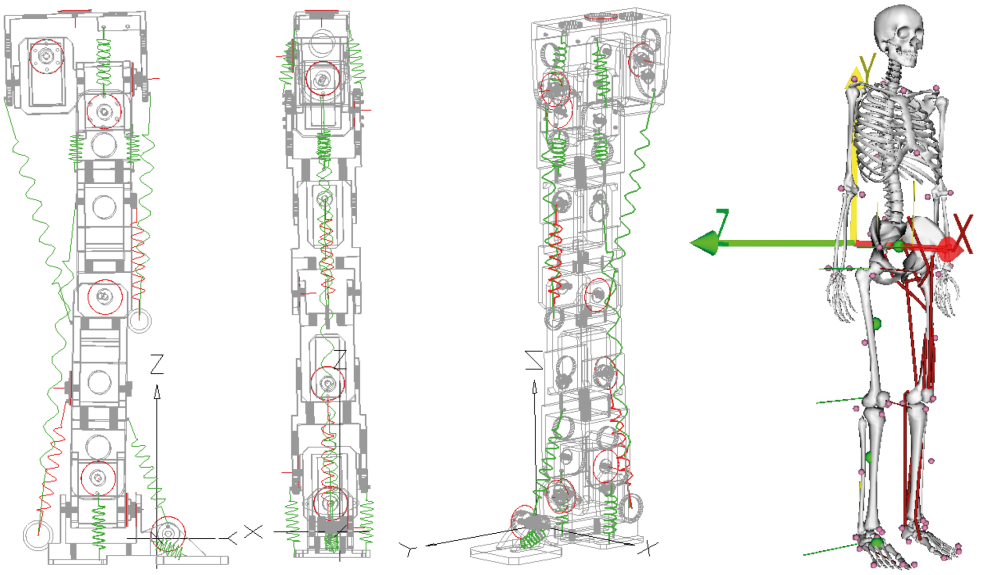

FIGURE 3.11: On the left hand-side, three views of the elastic actuation structure, spanning the Hip, Knee, and Ankle joints, are represented. On the right hand-side, the corresponding major human muscle groups are depicted, including from the top to the bottom: gluteus, psoas, bicep femoris and rectus femoris, vasti, gastrocnemius, soleus and tibialis anterior.

Spring 1, 4, and 5 around the foot controlled the equilibrium position of the ankle as it rotates around the plantar flexion axis (i.e., AnklePDF). Spring 5 also contributed to the shank's equilibrium position about the thigh (i.e., KneeFE). This action was then

balanced by spring 7 along the front of the knee. Spring 2 was the only spring without a paired mate. This was because while standing the toe would always produce a downward force on the ground and a short natural length of the spring prevented the toe from curling downward when the foot was raised. This then established a stable position for the ToeFE. Spring 3-13 was a matched pair on each ankle that prevented the foot from rolling around the inversion / eversion axis (i.e., AnkleIE). Spring 6 and 8 balanced the hips to the shanks of the robot. These were then combined with spring sets 9 and 10 to balance the hips to the thighs and thus established an equilibrium position for the anterior / posterior rotation of the pelvis about the thigh flexion axis (i.e., HipFE). Finally, a pair of spring 11-12 connected each leg to the hip to establish equilibrium of the lateral rotation of the thigh abduction / adduction (i.e., HipAA).

For propertly choose and positioning each spring a top-down approach was adopted [129]. It consisted of allowing the top piece of the assembly to rotate freely while pinning the part immediately under it to the ground. In the first stem this corresponds to letting the hips rotate while holding the thighs fixed. The stiffness for spring sets 6, 8, 9 and 10, which were associated with hip rotation, was then experimentally changed until the hip joint could reach a stable position. Of these, the primary foci were spring sets 6 and 8 since the other two were a balanced pair. After finding an upright equilibrium position for the hips, the top-down approach was applied to the thighs which could then rotate around the knees while the shanks were held fixed. This movement was used to determine the constants of the springs across the knees (i.e., spring sets 5 and 7). Then, the shanks were let free to rotate with the connected feet held fixed to infer the values for spring sets 1 and 4. Last, the feet were held fixed to produce a fullbody simulation of the model with a floor constraint. While this was an oversimplified floor constraint, it produced a completely stable standing model with no outside control. This theoretically demonstrated that the spring-stabilizing concept was valid.

For this project, tension springs have been chosen for use. When subjected to compression, the tension spring either acts as a rigid member or buckles, producing either an incredibly large reactive force or almost no force at all. In order to overcome this issue, the springs' natural lengths were shortened so that when the assembly moved, the springs always remained in tension. This prevented the nonlinear force reaction elicited by the compression of a tension-spring and pre-tensioned the entire system.

Finally, linear contact mechanics was implemented between the feet and the floor with a coefficient of friction of 0.5 and a coefficient of restitution of 0.5 [131]. These constraints

allowed the feet to rest on the floor and slide along it without falling through. The feet could also rise up off of the floor if the assembly were to fall over. Notice that, using the aforementioned constraints the floor is able to provide a force pushing the robot upward or to resist lateral movement with friction but it cannot hold the feet down to the floor in case the robot would fall.

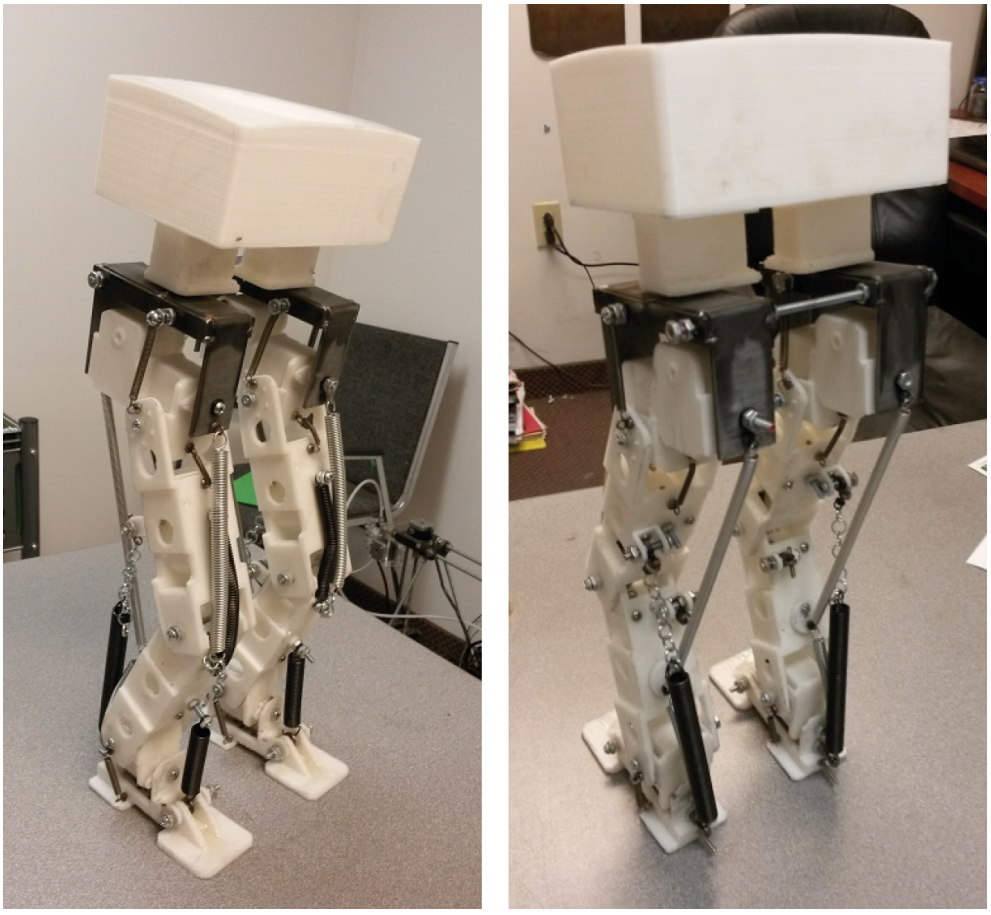

FIGURE 3.12: Front and rear views of the self-standing locomotive underactuated implement guided via elastic elements.

Each body part was fabricated using a plastic-extrusion type rapid prototyping machine. This method was chosen for its relatively quick turn-around, and because most of the links were hollow (Fig. 3.12). The joints of the robot were implemented using steel screws. The attachments for the springs were screwed directly into the link, which are made of PLA plastic. The spring attachments were custom made for easily adjusting the pretensioning of the springs in order to obtain the proper equilibrium point of the structure. Since the strength of PLA is generally low and the bracket connecting the hip with the waist is required to remain thin, this piece was fabricated using a 12-gage metal sheet. Changing the material to increase strength was necessary due to the high

force generated by one of the strongest springs attached on the bracket simulating the vastus medialis. The material was chosen for its low cost and easiness to be fabricated by press-bracketing. Additional strengthening at the foot was provided with an alluminum insert so to attach the gastrocnemius. Alluminum was chosen for its favorable mechanical properties and the easiness to be machined within our facility.

3.6.3 EKF-based estimation of viscoelastic joint parameters

The EKF is widely used in many engineering fileds to quantify the state of linear systems encompassing quickness in the estimation and quasi-optimal results. Here, an EKF with augmented states was utilized. The perturbation to the humanoid was delivered using a base-excitation. Among the advantages of EKF-based methods is that the excitation does not need to be a canonical input but can be delivered using an arbitrary input [132]. This method allows for fast estimations on a single trial, offering the potential to estimate joint stiffness during walking when proper robot actuation is implemented.
The impedance of a mechanical system is often modelled as a second order system [8]. Using such a model requires computing the first and second derivatives (i.e., $\dot{\theta}$, and $\ddot{\theta}$, respectively) of the joint angles (i.e., θ) [133]. Here, the identification of the stiffness and damping parameters of the assembly was investigated using a time series analysis of the measurement by means of an EKF. As a first approximation, the assembly system can be modeled as a base-excited inverted pendulum with one DOF (i.e., the rotation around the ankle joint), which can be represented as follows:

$$I\ddot{\theta} + b\dot{\theta} + k\theta = mgh \cdot \sin(\theta) + u + w_S \tag{3.35}$$

where for small displacement $\sin(\theta) \cong \theta$, yielding:

$$I\ddot{\theta} + b\dot{\theta} + (k - mgh)\,\theta = u + w_S \tag{3.36}$$

where I is the inertia of the whole system with respect to the ankle, b is the damping coefficient, k is the stiffness coefficient, m is the mass of the assembly, h is the distance between waist and ankle COMs, and g is the acceleration of gravity. $u = b\dot{\phi} + k\phi$, is the torque at the base due to a horizontal displacement d, where $\tan(\phi) = d/h \cong \phi$. w_S is the uncertainties of the system modeled as a Gaussian noise. The corresponding

augmented state space model can be defined by adding a number of states equal to the number of parameters that must be estimated (i.e., the damping coefficient, b, and the stiffness coefficient, k), so that the states can be defined as follows:

$$\begin{aligned} x_1 &= \theta && \text{Angular Position} \\ x_2 &= \dot{\theta} && \text{Angular Velocity} \\ x_3 &= b + w_B && \text{Damping Coefficient} \\ x_4 &= K_S + w_{K_S} && \text{Stiffness Coefficient} \end{aligned} \tag{3.37}$$

where $K_s = k - mgh$. The terms w_B and w_{K_S} are artificial noise terms that must be added to the system for each of the desired parameter in order for the Kalman filter to modify its estimates [134]. Hence, the EKF can be applied as follows:

$$EKF = \begin{cases} \dot{x} = f(x, w, u, t) \\ y = h(x, v) \\ w \sim (0, Q) \\ v \sim (0, R) \end{cases} \tag{3.38}$$

where f and h represent the process and observation functions, respectively, w and v are random noise of the augmented system state x, and the measurements vector y, Q and R are the corresponding covariance matrices. The subscript indicates the j-th discrete experimental measure. The filter was initialized as follows:

$$EKF_{init} = \begin{cases} \hat{x}_0 = E[x_0] \\ P_0 = E[(x_x - \hat{x}_0)(x_x - \hat{x}_0)^T] \end{cases} \tag{3.39}$$

where x_0 and P_0 represent the initial state and the covariance, respectively. The prediction phase was implemented as:

$$EKF_{pred} = \begin{cases} \hat{x}_j = f(x_{j-1}, u_j) \\ P_j = F_{j-1} P_{j-1} F_{j-1}^T + Q_{j-1} \end{cases} \tag{3.40}$$

and the update step as follows:

$$EKF_{update} = \begin{cases} G_j = P_j H_j^T \left(H_j P_j H_j^T + R \right)^{-1} \\ \hat{x}_j = \hat{x}_j + G_j \left(y_j - h(\hat{x}_j) \right) \\ P_j = \left(I - G_j H_j \right) P_j \end{cases} \tag{3.41}$$

where F and H are the Jacobian matrices of functions f and h, respectively. G represents the Kalman Gain, indirectly computed from the noise. Position and velocity information were corrupted imposing a Gaussian noise $N(0, 0.01)$. Finally, the EKF was tuned using the following parameters:

$$\begin{aligned} I_h &= mh^2 = 0.2672 \ kg \ m^2/rad \\ m &= 1.67 \ kg \\ h &= 0.4 \ m \\ g &= 9.81 \ m/s^2 \\ k &= 10 \ Nm/rad \\ K_S &= 3.45 \\ b &= \sqrt{I_h k_s} = 0.96 \end{aligned} \tag{3.42}$$

with initial state equal to $x_0 = [0.20 b K_S]^T$, P_0 identity matrix, Q diagonal matrix with elements equal to 0.01 and $R = 0.001$. It is worth noting that also the mass/inertial properties of the fasteners, springs, and other metal parts were considered within the solution of Eq. 3.35 and on the parameterization of the EKF filter (Eq. 3.42) because they have a significant effects on the overall system mass/inertia properties.

Chapter 4

Validation Procedures and Results

The evaluation of the proposed techniques was based on the available data chosen from the previously described datasets (Section 3.1).

The first, *Multiple Speed Walking Simulations* (Subsection 3.1.1), was principally used to investigate the mechanisms regulating multi-joint stiffness and quasi-stiffness during the stance phase of walking. The same dataset was also used to evaluate the impact of introducing the Force-Length-Velocity-Activation (FLVA) muscle properties within the muscle force optimization solution.

The second, *Muscle function of overground running across a range of speeds* (Subsection 3.1.2), was used to investigate how the musculotendon force estimates vary using different optimization settings: from the pure Static Optimization (SO) to the Computed Muscle Control (CMC) approaches with ideal force generators, with physiological FLVA properties, and with different sets of reserve actuators.

4.1 Dataset 1: *Multiple Speed Walking Simulations*

4.1.1 General evaluation

All trials were analyzed over a single stance phase. The obtained results, for each subject, were grouped with respect to the four different speeds: *s1* - 0.53 ± 0.035 m/s; *s2* - 0.75 ± 0.061 m/s; *s3* - 1.12 ± 0.071 m/s; *s4* - 1.49 ± 0.088 m/s. The weight of each subject was used as a normalization factor for the physiological and mechanical parameters in order to make the results directly comparable among the subjects.
A second step in the general evaluation of the obtained results included the estimation of Maximum Residual Forces (MRFs), Maximum Residual Moments (MRMs), and Maximum Position Error (MPE). The obtained values were compared with the available thresholds provided by the OpenSim documentation[1] and literature [105].
The MRFs were obtained during the third trial (i.e., *s3*) along x and z-axis, and during the fourth trial (i.e., *s4*) along the y-axis, with 4.314 N, 3.005 N, and 8.718 N, respectively. The MRMs were obtained during the third trial (i.e., *s3*) along x and y-axis, and during the first trial (i.e., *s1*) along the z-axis, with 1.216 Nm, 0.268 Nm, and 8.983 Nm, respectively. Similarly, the MPEs were encountered during the first trial (i.e., *s1*) on the HipFE, during the second and fourth trials (i.e., *s2*, and *s4*) on the HipAA, during the third trial (i.e., *s3*) on the AnklePDF, with 3.27°, 1.03° and 1.76°, and 2.7°, respectively.

4.1.2 Activation, Kinematics and Dynamics

In order to evaluate the ability of the subject-specific model to properly estimate the muscle activity across different walking speeds, the estimated muscle activations (Section 3.3) were compared to the experimentally recorded Electromyographic (EMG) profiles. A cross-correlation analysis between the EMG profiles and the corresponding estimated muscle activations was performed. The obtained cross-correlation sequences were normalised so that the auto-correlations at zero lag were identically 1.
Fig. 4.1 shows the ability of the subject-specific model to properly estimate the muscle activity across different walking speeds in comparison with the experimentally recorded EMG profiles. In some cases, the computed activation patterns were substantially different from experimental data. However, EMG data were not available for all lower

[1] http://simtk-confluence.stanford.edu:8080/display/OpenSim/Getting+Started+with+CMC

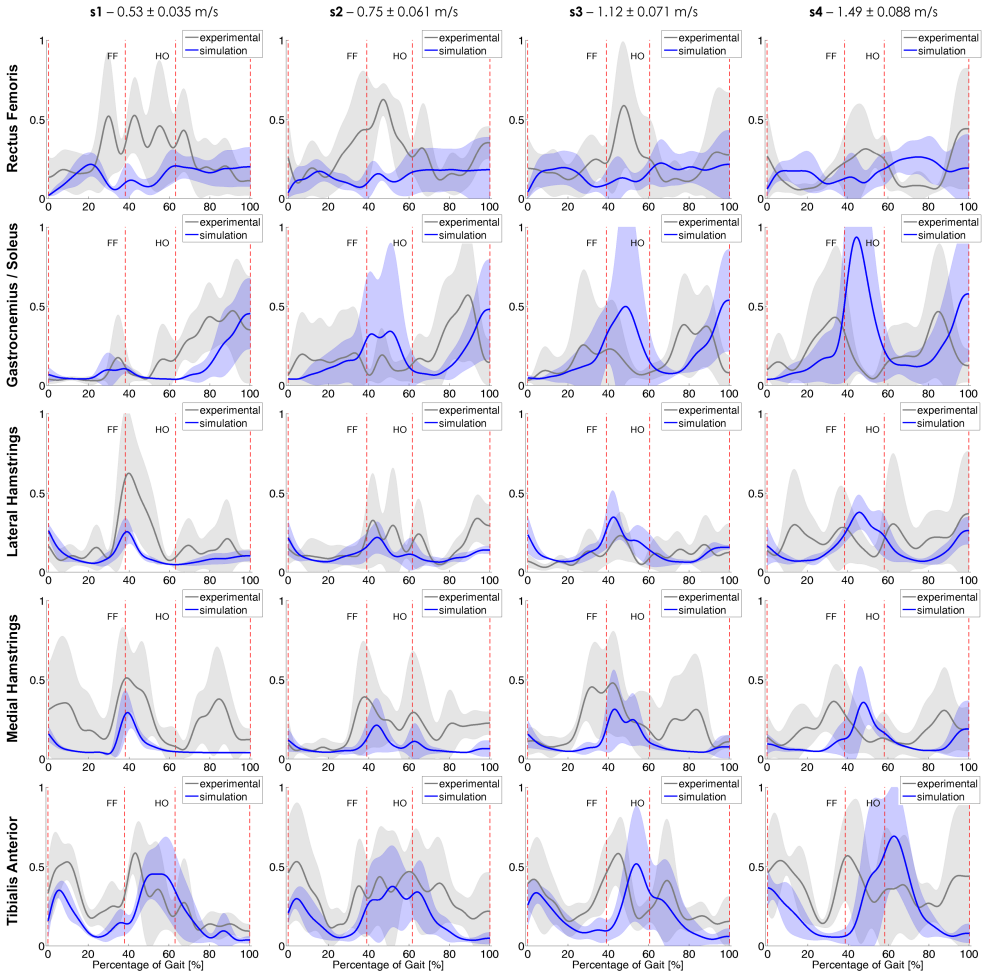

FIGURE 4.1: Comparison between right lower limb EMG envelopes (i.e., gray line and shaded area) and simulated muscle activity (i.e., blue line and shaded area). The results are expressed as mean±one standard deviation across the four trials, during the stance phase of gait. Among the stance limb events, Foot Flat (FF) and Heel Off (HO) are highlighted as vertical red dotted lines.

extremity muscles, making it impossible to compare simulated activation patterns for all major muscle groups. The simulated activations could have been forced to follow experimental EMG data more closely. However, as well documented in [93], the compensations required by CMC algorithm (Section 3.3) to accommodate large imposed changes in muscle excitations often cause substantial deviations in excitation patterns of other muscles and may also lead to poorly tracked kinematics.

Since the adopted workflow is not a pure EMG-driven approach, I believe that the results of testing the simulations kinematics, sagittal joint moments, and muscle excitations are adequate for this study. To support this claim, Fig. 4.2 shows the corresponding results of the cross-correlation analysis performed between the EMG profiles and the corresponding estimated muscle activations. The obtained cross-correlation sequences across

the major muscle groups reported maximum values of 0.8975±0.023 for *s1*, 0.9394±0.045 for *s2*, 0.9051±0.044 for *s3*, and 0.8968±0.063 for *s4*.

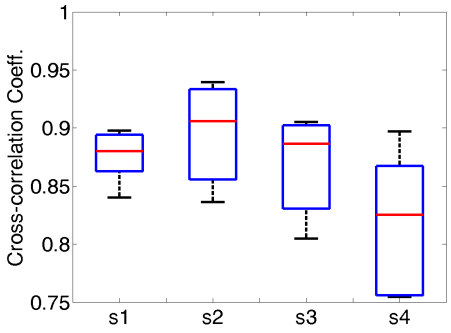

FIGURE 4.2: Results of cross-correlation analysis on muscle activations. In each box plot (i.e., one for each speed: *s1* - 0.53 ± 0.035 m/s; *s2* - 0.75 ± 0.061 m/s; *s3* - 1.12 ± 0.071 m/s; *s4* - 1.49 ± 0.088 m/s), the central mark is the median, the edges of the box are the 25th and 75th percentiles, the whiskers extend to the most extreme data points not considered outliers.

Each trial were also analysed from a kinematic (Fig. 4.3) and dynamic (Fig. 4.4) point of view in order to assess the ability of the subject-specific model to properly track the experimentally recorded trajectories and to predict dynamically consistent sagittal joint moments about the Hip Flexion-Extension (HipFE), Knee Flexion-Extension (KneeFE), and Ankle Plantar-Dorsi Flexion (AnklePDF).

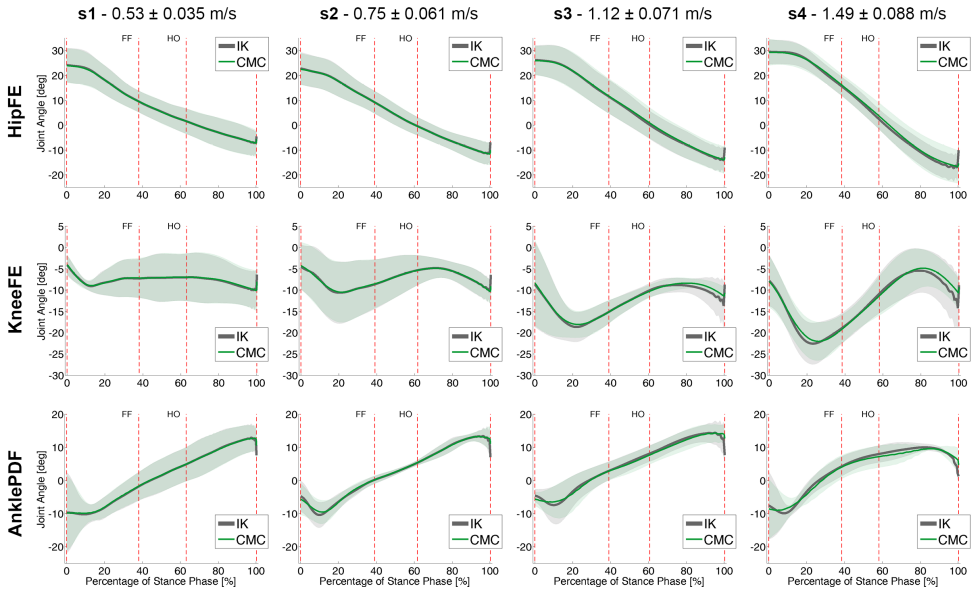

FIGURE 4.3: Right lower limb joint angles [deg] (HipFE, KneeFE, and AnklePDF) during the stance phase of gait. The results are expressed as mean±one standard deviation across the four trials, during the stance phase of gait. Among the stance limb events, Foot Flat (FF) and Heel Off (HO) are highlighted as vertical red dotted lines.

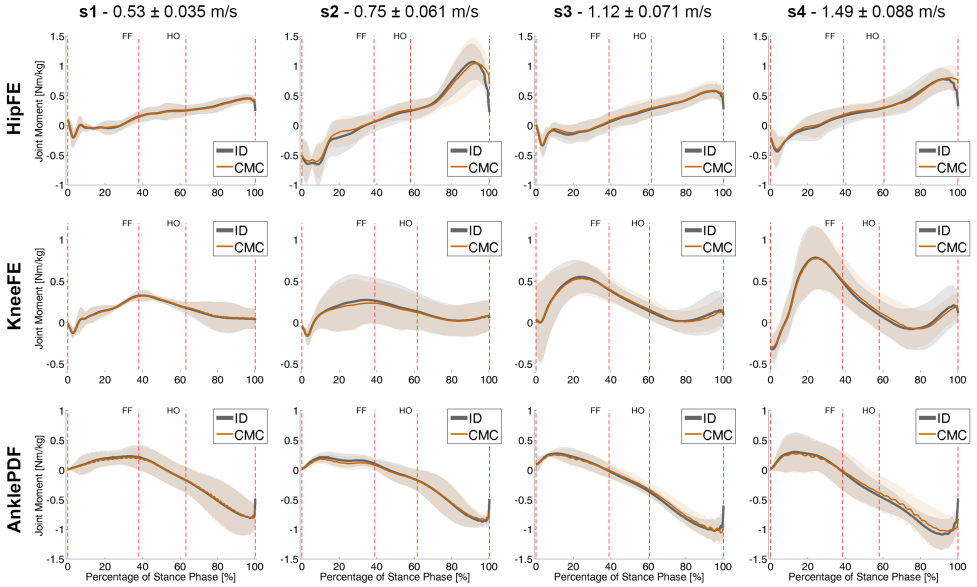

FIGURE 4.4: Right lower limb joint moments [Nm/kg] (HipFE, KneeFE, and AnklePDF) during the stance phase of gait. The results are expressed as mean±one standard deviation across the four trials, during the stance phase of gait. Among the stance limb events, Foot Flat (FF) and Heel Off (HO) are highlighted as vertical red dotted lines.

The predicted joint angles and joint moments, were compared to the reference values obtained from Inverse Kinematics (IK) and Inverse Dynamics (ID). Before computing mean and standard deviation, to compensate for the non-homogeneous distribution of weights, the joint moments were normalized by the weight of each subject. The Root Mean Square Errors (RMSEs) computed between the experimental and simulated profiles for the HipFE, KneeFE, and AnklePDF are provided in the Table 4.1.

TABLE 4.1: Root Mean Square Errors (RMSEs) of Kinematics [deg] and Dynamics [Nm/kg] estimates.

	KINEMATICS: Joint Angles				**DYNAMICS: Joint Moments**			
	s1	***s2***	***s3***	***s4***	***s1***	***s2***	***s3***	***s4***
HipFE	1.4798	0.7600	1.0688	1.0066	0.0182	0.0039	0.0284	0.0467
KneeFE	2.8234	1.4467	1.8430	1.4902	0.0091	0.0022	0.0262	0.0520
AnklePDF	2.0846	1.1751	1.4710	1.6813	0.0041	0.0009	0.0247	0.0446

4.1.3 Mechanics

From a mechanical point of view, the focus was on the evaluation of the estimated joint stiffness and inter-joint stiffness profiles (Section 3.4). Here, the inter-joint stiffness is the

existing relationship between joints due to bi-articular Musculotendon Units (MTUs). Moreover, the definitions of joint stiffness, based on the Short-Range Stiffness (SRS) model, and the definition of joint quasi-stiffness (Section 3.4) were directly compared and evaluated from a quantitative point of view.

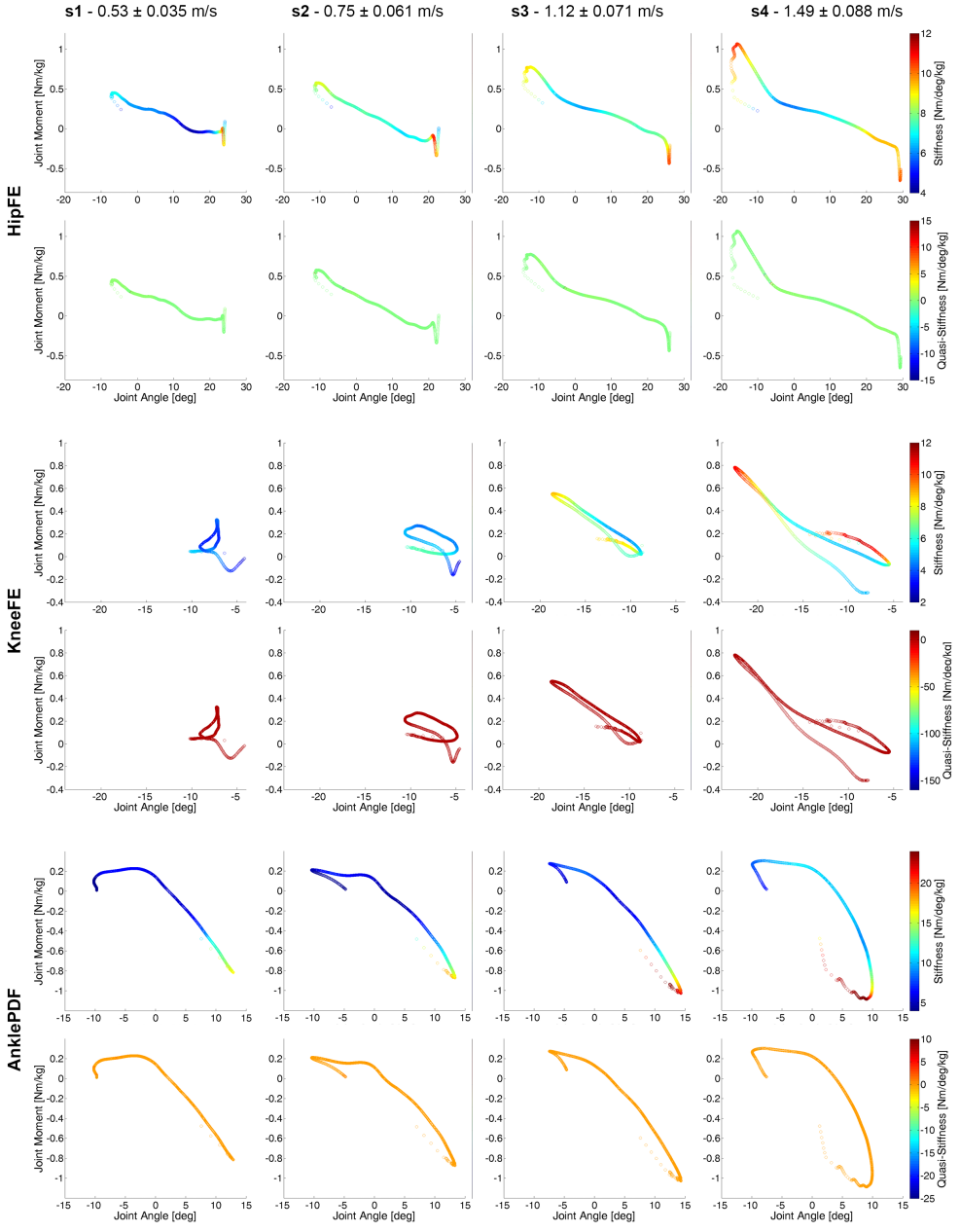

FIGURE 4.5: Estimated values of Hip, Knee, and Ankle Joint Stiffness and Quasi-Stiffness ([Nm/deg/kg]), for each speed. The joint moment (y-axis) was plotted as function of joint angle (x-axis). The color of each profile varies as function of the Stiffness and Quasi-Stiffness values within the ranges depicted in each color bar. The obtained results are plotted as mean values, by grouping the values of the four subjects with respect to the four distinct speeds.

Fig. 4.5 shows the joint moment (y-axis) plotted as function of joint angle (x-axis). The color of each profile varies as function of the stiffness and quasi-stiffness values within the ranges depicted in each color bar. By observing the graphs, as a whole, it is possible to see how the joint angles and moments change at different speeds.

There is a clear difference between stiffness and quasi-stiffness estimates. The former varies progressively during the execution of the movement, according to the dynamics of the lower limb and the interaction of the same with the ground. The latter presents an almost constant profile, except in some points related to significant events during the analyzed movement. With this regard, in Fig. 4.6 an enlargement of the results obtained for the Hip joint, at speed *s2* - 0.75 ± 0.061 m/s is provided, in order to better clarify the aforementioned differences.

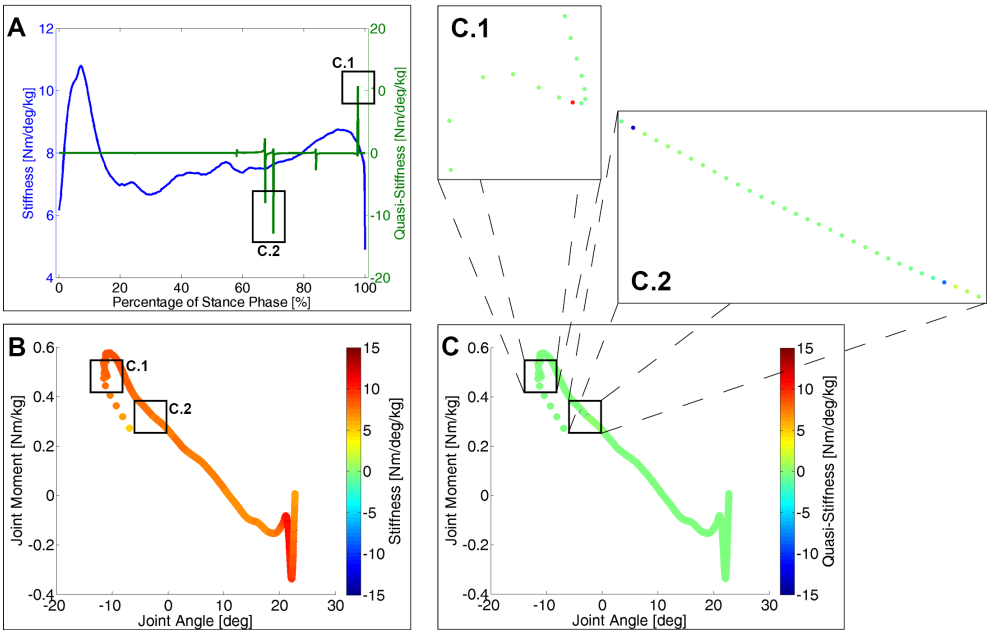

FIGURE 4.6: A representative comparison between specific points along the Stiffness and Quasi-Stiffness profiles (i.e., taken from Fig.4.5) for the Hip joint, at speed *s2* - 0.75 ± 0.061 m/s. (A) Joint Stiffness and Quasi-Stiffness [Nm/deg/kg] plotted as function of the percentage of stance phase (x-axis). (B) Joint Stiffness estimates plotted along the Torque-Angle curve. (C) Joint Quasi-Stiffness estimates plotted along the Torque-Angle curve. The color bar intervals were normalized within the same range to provide a direct comparison between (B) and (C). (C.1 - C.2) Enlargements of two specific windows as highlighted also in graphs (A) and (B).

Finally, the inter-joint stiffness profile regulation during the four different trials was evaluated (Fig. 4.7). It was found to be symmetric. Furthermore, the inter-joint stiffness between Hip and Ankle was negligible (i.e., order of magnitude of 10^{-14} Nm/deg/kg), in agreement with the absence of tri-articular muscles connecting the Ilium with the Foot. Since the stiffness is a positive definite tensor it is expected to be symmetric,

and these results confirm that all the algorithms were properly implemented. The inter-joint stiffness is not negligible for the pair Hip-Knee and Knee-Ankle. However, the magnitude of these stiffness time-profiles is smaller than those proper of the joints.

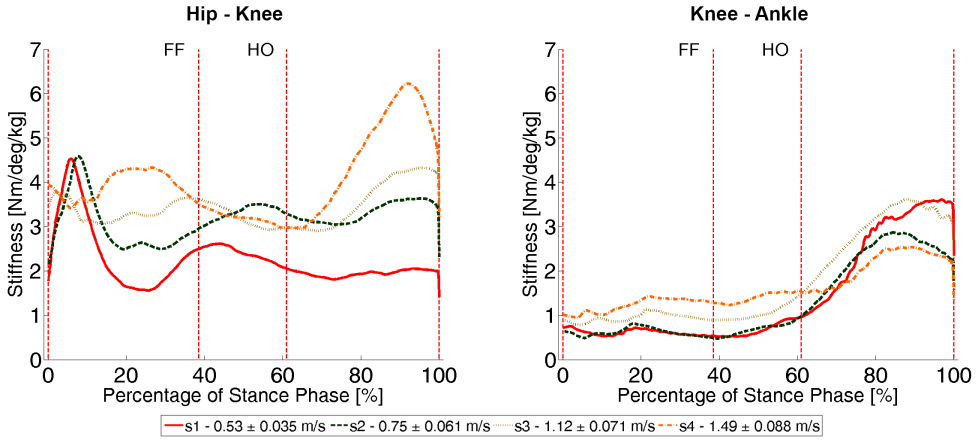

FIGURE 4.7: Estimated values of Hip-Knee and Knee-Ankle Inter-Joint Stiffness ([Nm/deg/kg]) relationship, for each speed. The obtained results are plotted as mean values, by grouping the values of the four subjects with respect to the four distinct speeds. Among the stance limb events, Foot Flat (FF) and Heel Off (HO) are highlighted as vertical red dotted lines.

4.2 Dataset 2: *Muscle function of overground running across a range of speeds*

4.2.1 General evaluation

All trials were anlysed over a single gait cycle beginning and ending at ipsilateral foot-strike. Results were time-normalised to a full stride cycle: from a foot strike to the next foot strike and then provided for each speed: *s1* - 3.56 m/s; *s2* - 5.20 m/s; *s3* - 7.00 m/s; *s4* - 9.49 m/s.

MTUs data were grouped into functional muscle compartments by summing the contributions from each MTU within the group (Table 4.2). Stride length, stride frequency, peak joint moment and peak joint stiffness were calculated for a single stride for each trial. Stride length was defined as the anterior distance travelled by consecutive ipsilateral foot-strikes, calculated from the heel marker at the time of initial foot-ground contact. Stride frequency was calculated by dividing running speed by stride length.

TABLE 4.2: Innervation zones, corresponding muscle groups from which experimental EMG were recorded and the associated MTUs in the adopted model. For each MTU, Maximum Isometric Force (MIF), Optimal Fiber Length (OFL), Tendon Slack Length (TSL), and Pennation Angle (PA) at OFL are provided.

Innervation Zones	**Muscle Groups**	**EMG**	**MTU**	**MIF [N]**	**OFL [m]**	**TSL [m]**	**PA [rad]**
Superior Gluteal Nerve	Gluteus Minimus		gmin1	810	0.069785	0.016420	0.174530
			gmin2	855	0.065219	0.020350	0.000000
			gmin3	969	0.039898	0.053548	0.017453
	Gluteus Medius	*	gmed1	2457	0.049845	0.072671	0.139630
		*	gmed2	1719	0.080209	0.050309	0.000000
		*	gmed3	1959	0.063704	0.052265	0.357800
	Tensor Fasciae Latae		tfl	699	0.099706	0.446050	0.052360
Inferior Gluteal Nerve	Gluteus Maximus	*	gmax1	1719	0.138380	0.097448	0.087266
		*	gmax2	2457	0.146150	0.106380	0.000000
		*	gmax3	1656	0.144880	0.130800	0.523000
	Gemellus		gem	492	0.026262	0.042676	0.000000
Femoral Nerve	Iliacus		iliacus	3219	0.097906	0.129310	0.250000
	Gracilis		grac	486	0.252820	0.277680	0.143120
	Quadricep Femoris		quadfem	1143	0.056950	0.025311	0.000000
	Rectus Femoris	X	rectfem	3507	0.125600	0.361100	0.242600
	Sartorius		sar	468	0.424860	0.147590	0.022690
	Vastus Lateralis	X	vaslat	5613	0.107320	0.151330	0.321140
	Vastus Intermedius		vasint	4095	0.092961	0.145320	0.078540
	Vastus Medialis	X	vasmed	3882	0.106720	0.122730	0.516620
Lumbar Plexus Nerve	Psoas		psoas	3339	0.094994	0.176420	0.185000
Obtural Nerve	Adductor Group		addmag1	1143	0.09505	0.032776	0.261800
			addmag2	1029	0.134390	0.099956	0.261800
			addmag3	1464	0.143620	0.272980	0.261800
			addlong	1881	0.114810	0.148340	0.123910
			addbrev	1287	0.108460	0.052601	0.106470
	Gracilis		gra	486	0.252820	0.277680	0.143120
Tibialis Nerve	Gastrocnemius Medialis	X	gasmed	4674	0.068869	0.461420	0.350000
	Gastrocnemius Lateralis	X	gaslat	2049	0.074574	0.454330	0.210000
	Lateral Hamstrings	*	bifemlh	2688	0.109580	0.367080	0.202460
		*	bifemsh	2412	0.119860	0.164850	0.214680
	Soleus	X	sol	10647	0.058013	0.290070	0.576000
	Tibialis Posterior		tibpost	4764	0.042903	0.344130	0.244350
Sciatic Nerve	Medial Hamstrings	*	semimem	3864	0.087532	0.376390	0.261800
		*	semiten	1230	0.222470	0.304930	0.226900
Deep Fibular Nerve	Tibialis Anterior	X	tibant	2715	0.078736	0.282320	0.174530
Fibular Nerve	Peroneous Group		perbrev	1305	0.056610	0.182290	0.200000
			perlong	2829	0.054958	0.386950	0.261800
			perter	540	0.091290	0.115560	0.226890
Foot Nerve	Flexor Group		flexdig	930	0.048664	0.420670	0.244350
			flexhal	966	0.056089	0.39379	0.296700
	Extensor Group		extdig	1536	0.076618	0.412640	0.200000
			exthal	486	0.092418	0.359890	0.174530

'X' experimental EMG signals for single MTU; '*' experimental EMG signals for combined MTU

Table 4.3 shows that the percentage increase in stride length was greater than that in stride frequency as running speed increased from 3.56 m/s to 7.0 m/s, while the opposite effect was observed at 9.49 m/s. Peak joint moments showed the higher values at the maximum speed of 9.49 m/s with a constant increasing profile among the four trial in the hip and ankle joints. On the other hand, the knee joint moment showed a significant increase from 3.56 m/s to 5.20 m/s, while an opposite trend was observed from 5.20 m/s to 9.49 m/s. Peak joint stiffness reached the absolute maximum value in the hip joint at 5.20 m/s. Knee joint showed an increasing trend from 3.56 m/s to 5.20 m/s and the same is for the ankle joint from 3.56 m/s to 7.00 m/s, although the increase of the knee (i.e., 17.77 Nm/deg) is slightly lower than that of the ankle (i.e., 19.02 Nm/deg).

TABLE 4.3: Magnitude of stride length, stride frequency; Peak joint moments, and peak values of joint stiffness during HipFE, KneeFE, and AnklePDF, across the four speeds: *s1* - 3.56 m/s; *s2* - 5.20 m/s; *s3* - 7.00 m/s; *s4* - 9.49 m/s.

	s1 - 3.56 m/s	**s2 - 5.20 m/s**	**s3 - 7.00 m/s**	**s4 - 9.49 m/s**
		Stride Length [m]		
	2.68	3.58	4.14	4.40
		Stride Frequency [Hz]		
	1.33	1.45	1.69	2.16
		Peak Joint Moment [Nm]		
HipFE	95.95	150.44	260.22	445.62
KneeFE	243.46	305.68	279.61	226.04
AnklePDF	3.03	5.76	10.79	16.36
		Peak Joint Stiffness [Nm/deg]		
HipFE	100.48	124.22	113.55	110.91
KneeFE	96.01	113.78	105.56	108.51
AnklePDF	93.75	110.92	112.95	110.09

The MRFs, estimated for the second dataset, were obtained during the fourth trial (i.e., *s4*) along x and z-axis, and during the third trial (i.e., *s3*) along y-axis, with 1.44 Nm, 1.67 Nm, and 11.54 Nm, respectively. On the other hand, the MRMs were obtained during the third trial (i.e., *s3*) along x-axis, during the fourth trial (i.e., *s4*) along y-axis, and during the second trial (i.e., *s2*) along the z-axis, with 19.22 N, 33.48 N, and 9.39 N, respectively. The MPE across the four trials was of 25 mm in pelvis translation during the second trial (i.e., *s2*).

The same parameters were evaluated also with respect to five different sets of residual and reserve actuators (Section 3.3). In this case, the MRFs were obtained during the third trial (i.e., s3) along x, y and z-axis, with 1.42 Nm, 1.66 Nm, and 9.35 Nm, respectively. The MRMs were obtained during the third trial (i.e., s3) along x-axis and y-axis, and during the second trial (i.e., s2) along the z-axis, with 19.17 N, 13.48 N, and 9.49 N, respectively. The MPE across the three trials was of 18 mm in pelvis translation during the second trial (i.e., s2).

4.2.2 Activation, Kinematics and Dynamics

Similarly to the evaluation done for the first dataset, the ability of the subject-specific model to properly estimate the muscle activity across different walking speeds was compared with the experimentally recorded EMG profiles (Fig. 4.8). The assessment was limited to a subset of MTUs for which an experimentally recorded EMG signal was available. Fig. 4.8 shows a comparison between the simulated muscle activation, computed with the SO and CMC approaches (Section 3.3), and the experimentally recorded EMG signals. In particular, the SO solutions are based on the use of two different sets of residual and reserve actuators (i.e., SO rr01 and SO rr02 that corresponds to the first and fifth columns of Table 3.2, respectively).

A cross-correlation analysis (Fig. 4.9) between the EMG profiles and the corresponding estimated muscle activations was performed. The obtained cross-correlation sequences were normalized so that the auto-correlations at zero lag were identically 1.0. The cross-correlation sequences (Fig. 4.9 - XCORR) reported mean values in the range 0.74±0.04 between SOrr01 and EMG env, 0.76±0.05 between SOrr02 and EMG env, and 0.75±0.04 between CMC and EMG env. All three simulated muscle activation solutions are strictly correlated to the experimental EMG profiles in terms of wave form. However, in terms of amplitude the CMC-based solutions seem to be better than pure SO-based estimates (Fig. 4.9 - RMSE). This directly reflects on the generated MTU forces and SRS.

Then, the attention was focused on assess the ability of the subject-specific model to properly track the experimentally recorded trajectories (Fig. 4.10(A)) and to predict dynamically consistent sagittal joint moments (Fig. 4.10(B)) about the HipFE, KneeFE, and AnklePDF (Section 3.3) across the four trial performed by the subject. The predicted joint angles and joint moments were compared with the solutions obtained from the IK and ID, respectively. Here, just a cumulative representation of the joint angles

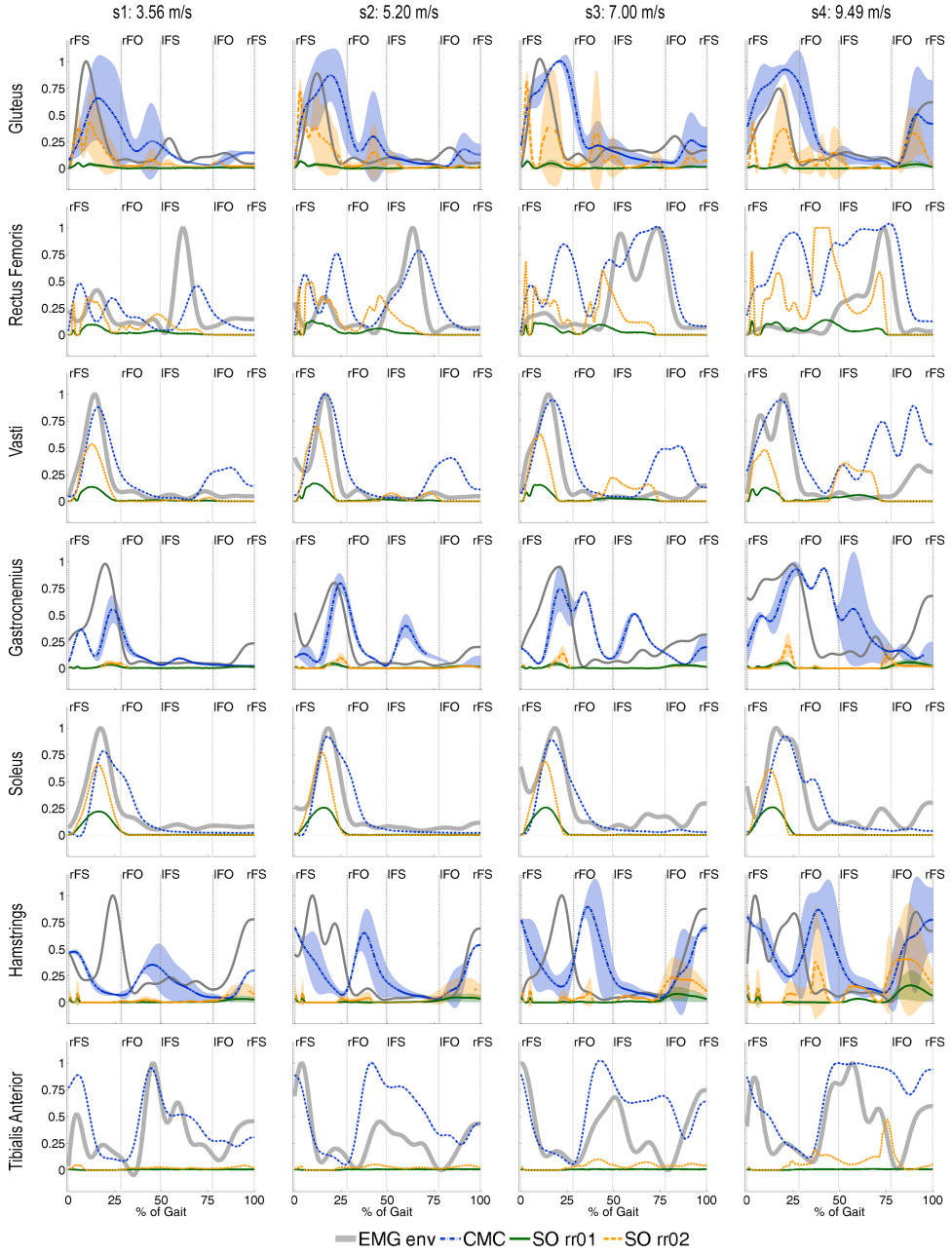

FIGURE 4.8: Comparison between right lower limb EMG envelopes (i.e. gray line) and simulated muscle activity across running speeds, during a single gait cycle beginning and ending at ipsilateral foot-strike. Combined MTU activations are expressed as mean±one standard deviation. Blue dotted lines represent the estimates obtained with the dynamic approach (i.e., CMC). Yellow and green lines are for the estimates obtained with the static approach (ie., SO) using two different sets of residual and reserve actuators. The vertical dotted lines represent the major gait events: Right Foot Strike (rFS), Right Foot Off (rFO), Left Foot Strike (lFS), and Left Foot Off (lFO).

and moments tracking was provided with the purpose to give an overall assessment. Considering the IK results as reference value of the experimentally recorded Motion Capture (MC) data, the simulated joint angles tracked the experimental data with a RMSE of 5.56°, 9.18°, and 6.71° for the HipFE, KneeFE, and AnklePDF, respectively.

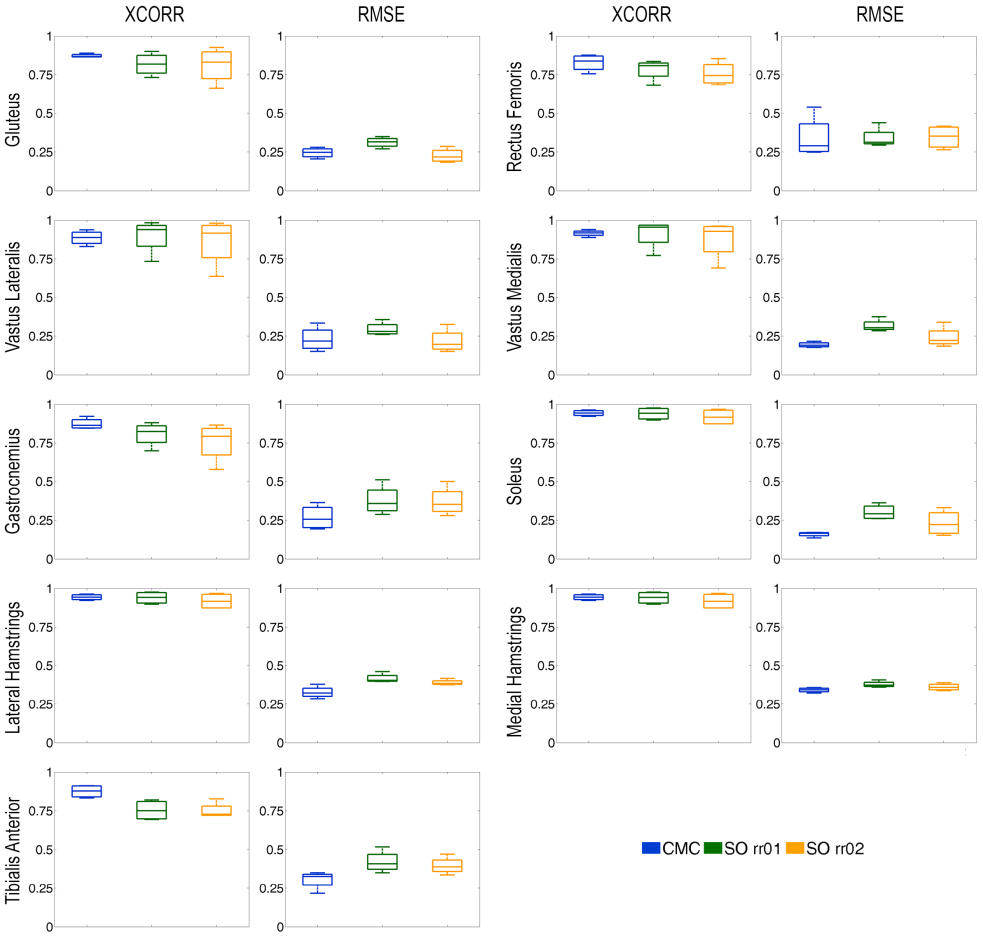

FIGURE 4.9: Maximum values of the cross-correlation (XCORR) functions and Root Mean Square Errors (RMSEs) computed between EMG signal profile and corresponding estimated muscle activations, across running speeds, during a single gait cycle beginning and ending at ipsilateral foot-strike. Blue box plots are referred to the dynamic approach (i.e., CMC). Yellow and green box plots are for the estimates obtained with the static approach (ie., SO) using two different sets of residual and reserve actuators.

Considering the range of values assumed by the IK results, these RMSEs corresponds to a mean error of about 5%, across all speeds and DOFs. Fig. 4.10(B) shows that the simulated joint moments [Nm] computed by summing the moments generated by MTUs at each joint matched the experimental joint moments computed by solving the ID. The RMSE computed between ID and simulation results are of 48.3 Nm, 36.67 Nm, and 30.3 Nm for the HipFE, KneeFE, and AnklePDF, respectively. The aforementioned values corresponds to a mean error of about 6.71%, across all speeds and DOFs. Moreover, the range of values obtained for the HipFE, KneeFE and AnklePDF are within the range of values obtained on the complete original dataset by Dorn et al. [96].

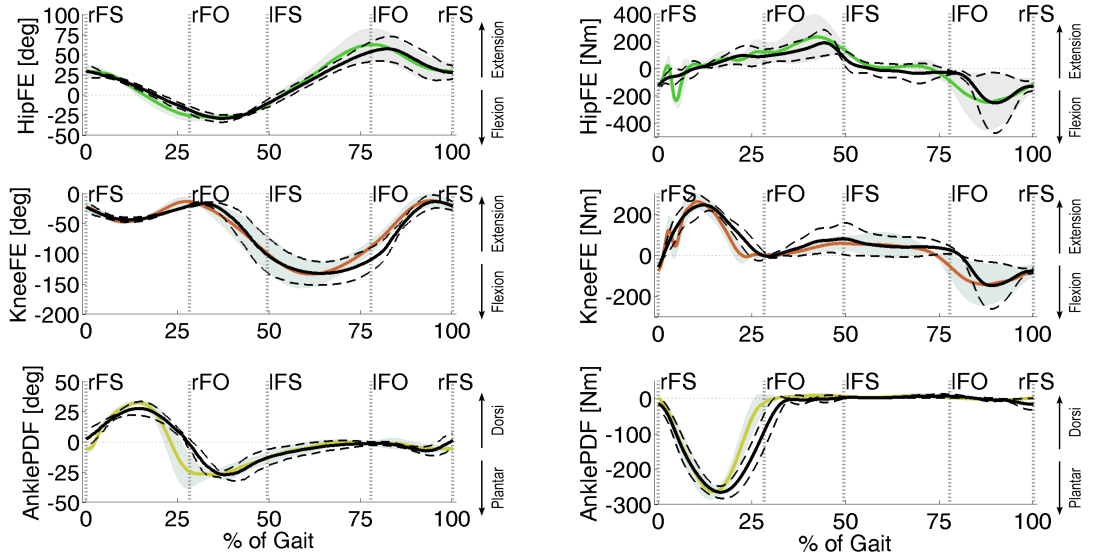

(a) Kinematics (b) Dynamics

FIGURE 4.10: (A) Right lower limb joint angles [deg]. (B) Right lower limb joint moments [Nm]. HipFE, KneeFE, and AnklePDF during a single gait cycle beginning and ending at ipsilateral foot-strike. The results are expressed as mean±one standard deviation across running speeds. Colored lines and corresponding shaded areas are reference values from IK and ID solutions; black solid lines represent mean values, with the corresponding standard deviation as black dashed lines referred to the simulation estimates. The vertical dotted lines represent the major gait events: Right Foot Strike (rFS), Right Foot Off (rFO), Left Foot Strike (lFS), and Left Foot Off (lFO).

4.2.3 Mechanics

From a mechanical point of view, Fig. 4.11 shows the obtained estimates of joint stiffness [Nm/deg] for the HipFE, KneeFE and AnklePDF. All three joint stiffness mean values tend to increase as the speed increases, but with different rates. The mean values plus and minus one standard deviation for the CMC-based estimates across the four speeds are: 45.62±16.86 Nm/deg (*s1*), 53.65±19.72 Nm/deg (*s2*), 60.31±14.08 Nm/deg (*s3*), 73.75±22.97 Nm/deg (*s4*) for the hip; 26.65±19.02 Nm/deg (*s1*), 30.93±20.23 Nm/deg (*s2*), 35.84±21.18 Nm/deg (*s3*), 51.54±32.5 Nm/deg (*s4*) for the knee; and 46.85±14.87 Nm/deg (*s1*), 57.28±16 Nm/deg (*s2*), 62.82±16.5 Nm/deg (*s3*), 76.87±18.18 (*s4*) Nm/deg for the ankle.

Also in this case, the inter-joint stiffness for each combination of two joints was found to be symmetric. Furthermore, the inter-joint stiffness between Hip and Ankle was negligible (i.e., 0.7±0.014 Nm/deg), in agreement with the absence of tri-articular muscles connecting the Ilium with the Foot. The inter-joint stiffness is not negligible for the pair

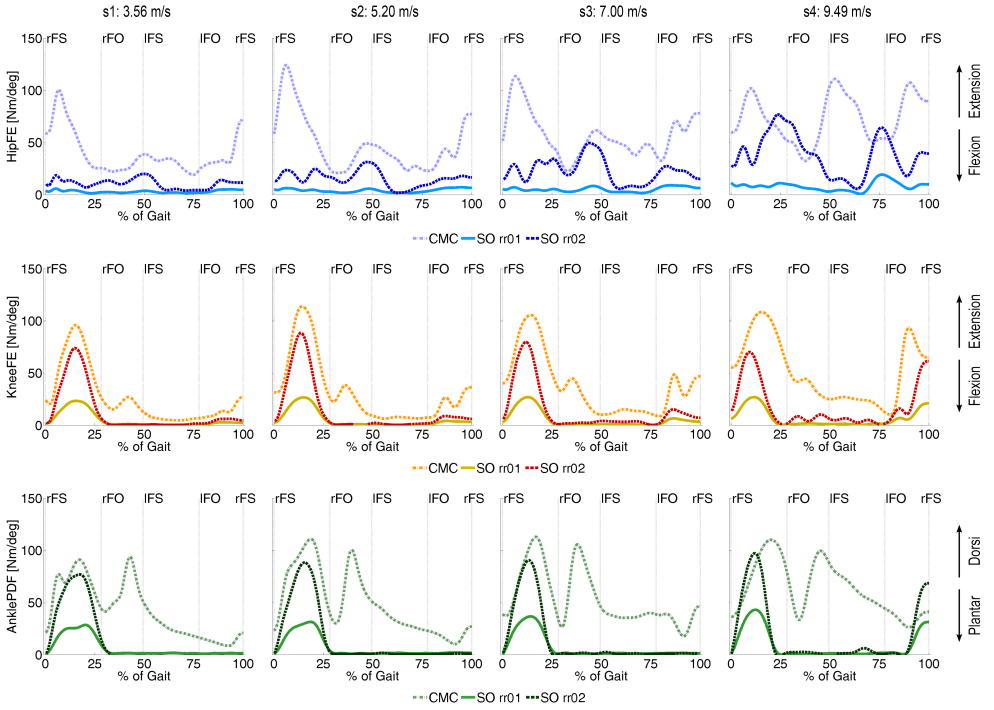

FIGURE 4.11: Comparison of estimated joint stiffness [Nm/deg] during a single gait cycle beginning and ending at ipsilateral foot-strike. HipFE, KneeFE, and AnklePDF joint stiffness estimates across running speeds, for the SO approach using two different sets of residual and reserve actuators, and for the CMC approach. The vertical dotted lines represent the major gait events: Right Foot Strike (rFS), Right Foot Off (rFO), Left Foot Strike (lFS), and Left Foot Off (lFO).

Hip-Knee and Knee-Ankle (Fig. 4.12). However, the magnitude of these stiffness time profiles is again smaller than those proper of the joints.

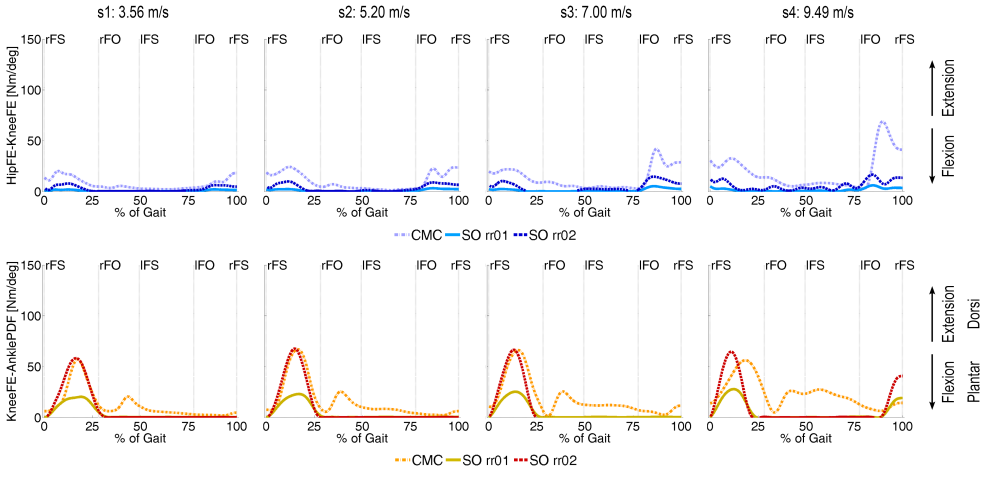

FIGURE 4.12: Comparison of estimated inter-joint stiffness [Nm/deg], between Hip and Knee, and between Knee and Ankle, during a single gait cycle beginning and ending at ipsilateral foot-strike, across running speeds, for the SO approach using two different sets of residual and reserve actuators, and for the CMC approach. The vertical dotted lines represent the major gait events: Right Foot Strike (rFS), Right Foot Off (rFO), Left Foot Strike (lFS), and Left Foot Off (lFO).

4.3 Preliminary Evaluations

As part of the research activity described in this thesis, they are worth mentioning some preliminary evaluations with respect to two major issues.
The first, is about how different human muscle models affect the estimation of lower limb joint stiffness during running [109]. The set of preliminary results provided here, despite assuming equal muscle activations which has been calculated via CMC, shows significant differences in the joint stiffness estimates obtained by adopting either *Thelen2003Muscle* (Section 3.3) or *Millard2012EquilibriumMuscle*[2] model.

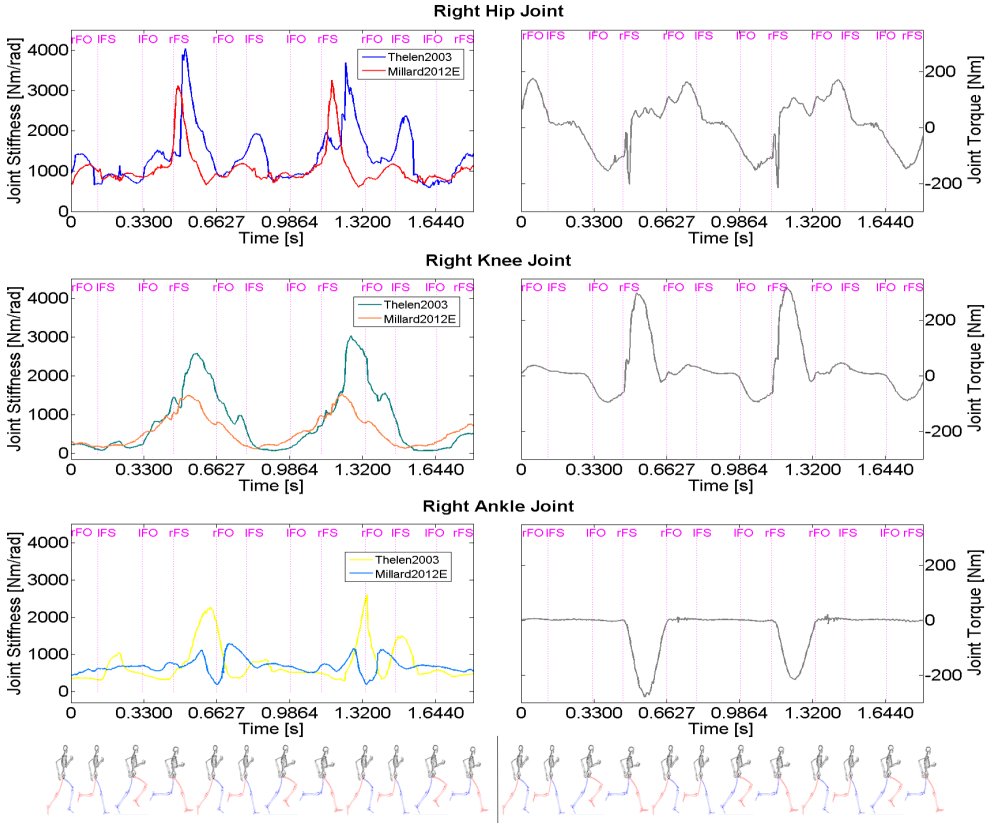

FIGURE 4.13: Right Lower Limb Joint Stiffness and Joint Torque estimated values.The x-axis reports the time-samples, while y-axis expresses the joint stiffness [Nm/rad] and joint torque [Nm]. The labels lFO, lFS, rFO, rFS stand for Left Foot-Off, Left Foot-Strike, Right Foot-Off, and Right Foot-Strike respectively.

Fig.4.13 shows a misalignment of the peaks of the stiffness time profiles with respect to the different phases of movement, in particular for the hip and ankle joints. A delay can be noticed between the instants in which the foot impacts the ground and the instant in which the stiffness peaks gererated by either model occur. Notice that Thelen's model has an average delay of 112 ms compared to the 57 ms of Millard's model. Furthermore, Thelen's model produces stiffness peaks with a much larger amplitude compared to the

[2] http://simtk-confluence.stanford.edu:8080/display/OpenSim/Millard+2012+Muscle+Models

model of Millard. The stiffness peaks for both hip and knee occurs almost synchronously within each model. The ratio of hip/knee stiffness at the peak is different for the two models: 1.8 (Thelen's model), 2.3 (Millard's model). It is bigger in Millard's model indicating a predominancy of hip stiffness over the other joints. Finally, the ankle stiffness is drammatically different between the two models. Similar considerations hold true for the left lower limb joints. What was discussed previously is still valid for the estimates of inter-joint stiffness. It was found symmetric and not negligible for the pairs Hip-Knee and Knee-Ankle, as depicted in Fig. 4.14.

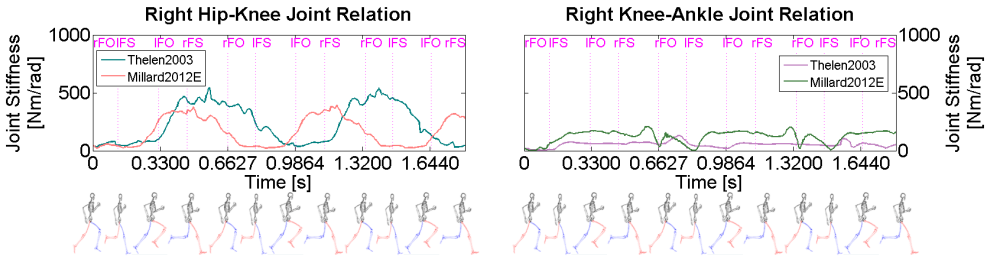

FIGURE 4.14: Right Lower Limb Inter-Joint Stiffness. The x-axis reports the time-samples, while y-axis expresses the joint stiffness [Nm/rad]. The labels lFO, lFS, rFO, rFS stand for Left Foot-Off, Left Foot-Strike, Right Foot-Off, and Right Foot-Strike respectively.

The second issue concerns the human muscle-tendon stiffness estimation during normal gait cycle based on Gaussian Mixture Model (GMM) [120]. The preliminary results provided here regard a study in which unlike the analytical techniques already widely validated in literature, a probabilistic approach based on the GMM was adopted for the computation of the muscle-tendon unit stiffness.

Normal gait cycle data collected from four different subjects (Subsection 3.1.1) were used to train a model of the muscle-tendon stiffness (Section 3.5). The four different velocities were subdivided into training and testing sets. In order to compare data recorded at different speed, time instants were normalized between 0 and 1, corresponding to the beginning and the ending of the gait cycle. 43 models, one for each muscle, for 2 legs, by considering 4 velocities for each subject, were obtained. That is, the muscle-tendon stiffness was related at the time that characterizes the analyzed movement. This approach has been adopted for each of the 4 subject, using a leave-one-out technique in relation to the velocities: three for training the model and one for testing. No experiments have been conducted to compare different subjects' gaits. A total of 1376 models have been obtained as a function of the *gait phase*. Some examples referred to the major muscles involved in the task are reported in Fig. 4.15. On y-axis the muscle-tendon stiffness values of Gluteus Medialis, Bicep Femoris, Iliacus, Psoas, Vastus Lateralis, and Soleus are provided as function of the *gait phase*, represented on x-axis by the time instants normalized between 0 and 1. The stiffness of the Gluteus appears to be underestimated

compared to that calculated with the analytical approach (Section 3.4). An overestimation is evident for Psoas, Bicep Femoris and Iliacus. By far, the best looking results are observed on Vastus and Soleus muscles, commonly excited during the KneeFE movements.

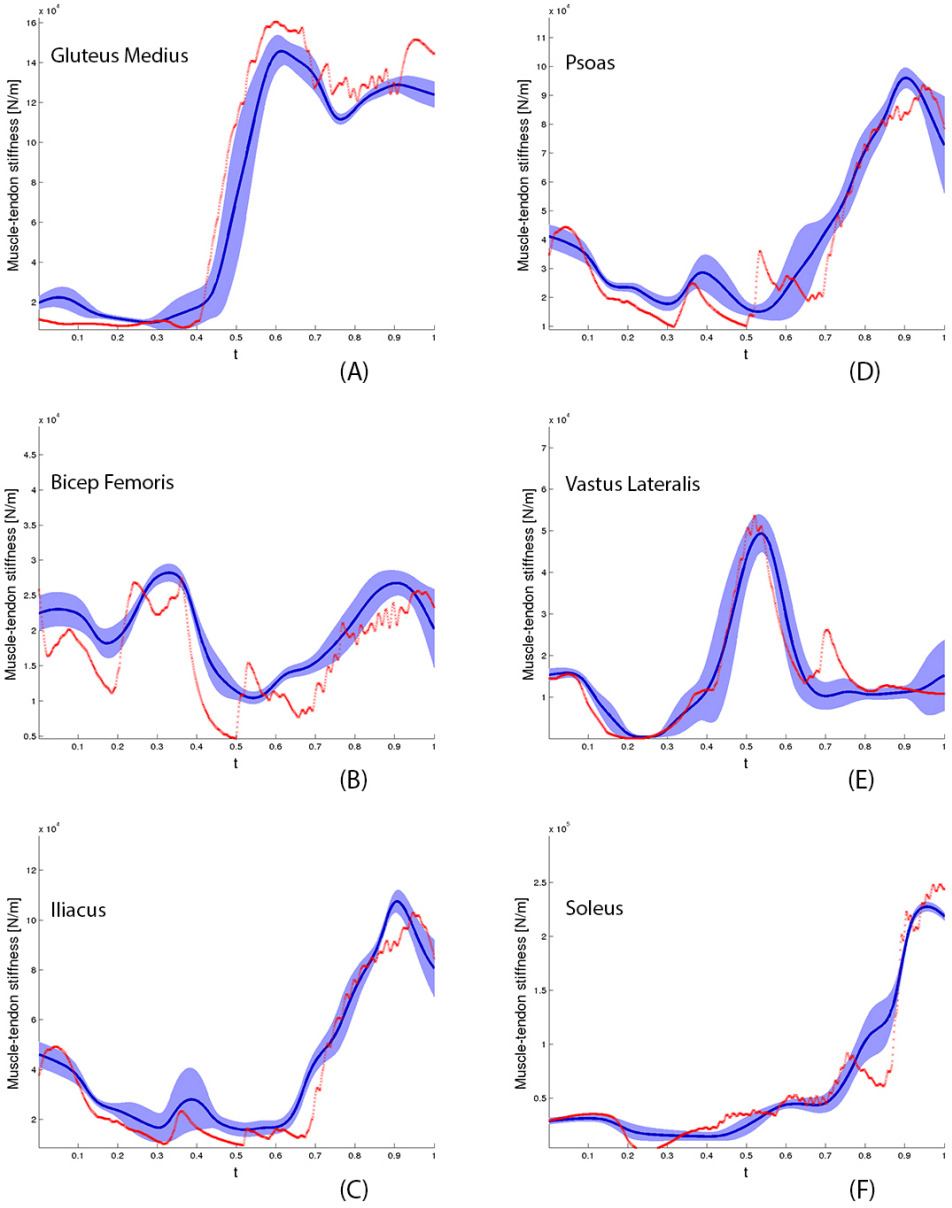

FIGURE 4.15: Muscle-Tendon Stiffness values computed using the analytical approach (RED) and the corresponding estimated values using the GMR approach (BLUE).

The RMSE between the values computed by using the analytical approach and those estimated through the Gaussian Mixture Regression (GMR) has been computed to evaluate the effectiveness of the proposed GMM-based technique. On the RMS values for each velocity, the mean error and the standard deviation were computed, in order to obtain the error related to each muscle of each subject. The resulting eight graphs are reported in Fig. 4.16. On the x-axis, the reported muscles are listed in the following

order: 1. Gluteus Medius 1, 2. Gluteus Medius 2, 3. Gluteus Medius 3, 4. Gluteus Minimus 1, 5. Gluteus Minimus 2, 6. Gluteus Minimus 3, 7. Semimembranosus, 8. Semitendinosus, 9. Bicep Femoris (long head), 10. Bicep Femoris (short head), 11. Sartorius, 12. Adductor Longus, 13. Adductor Brevis, 14. Adductor Magnus 1, 15. Adductor Magnus 2, 16. Adductor Magnus 3, 17. Tensor Fasciae Latae, 18. Pectineus, 19. Gracilis, 20. Gluteus Maximus 1, 21. Gluteus Maximus 2, 22. Gluteus Maximus 3, 23. Iliacus, 24. Psoas, 25. Quadricep Femoris, 26. Gemellus, 27. Piriformis, 28. Rectus Femoris, 29. Vastus Medialis, 30. Vastus Intermedius, 31. Vastus Lateralis, 32. Gastrocnemius Medialis, 33. Gastrocnemius Lateralis, 34. Soleus, 35. Tibialis Posterior, 36. Flexor Digitorum, 37. Flexor Hallucis, 38. Tibialis Anterior, 39. Peroneus Brevis, 40. Peroneus Longus, 41. Peroneus Tertius, 42. Externsor Digitorum, 43. Extensor Hallucis.
On the y-axis are showed the RMS values expressed in N/m, in accordance with the unit of measure of the MTU stiffness. The figures are respectively related to GIL01 subject, left (A) and right (B) leg limbs, GIL02 subject, left (C) and right (D) leg limbs, GIL06 subject, left (E) and right (F) leg limbs, and GIL08 subject, left (G) and right (H) leg limbs.
Results show a positive trend with an error amounting to an order of magnitude less compared to the dispersion of the measured dataset. In general, a higher accuracy in the adductor group is noticeable, while a greater deviation emerges on gluteus and tibialis muscle groups. As with regard to the muscles that control the hip movements (among others, gluteus and adductors), oscillations are observable, which could be imputable to the actions put in place to maintain the torso in an upright position during locomotion. On the other hand, several oscillations are shown on the tibialis muscle group. These are directly connected to the ankle joint displacement during the foot-ground contact, in particular during the stages of transition from single to double support and vice versa.

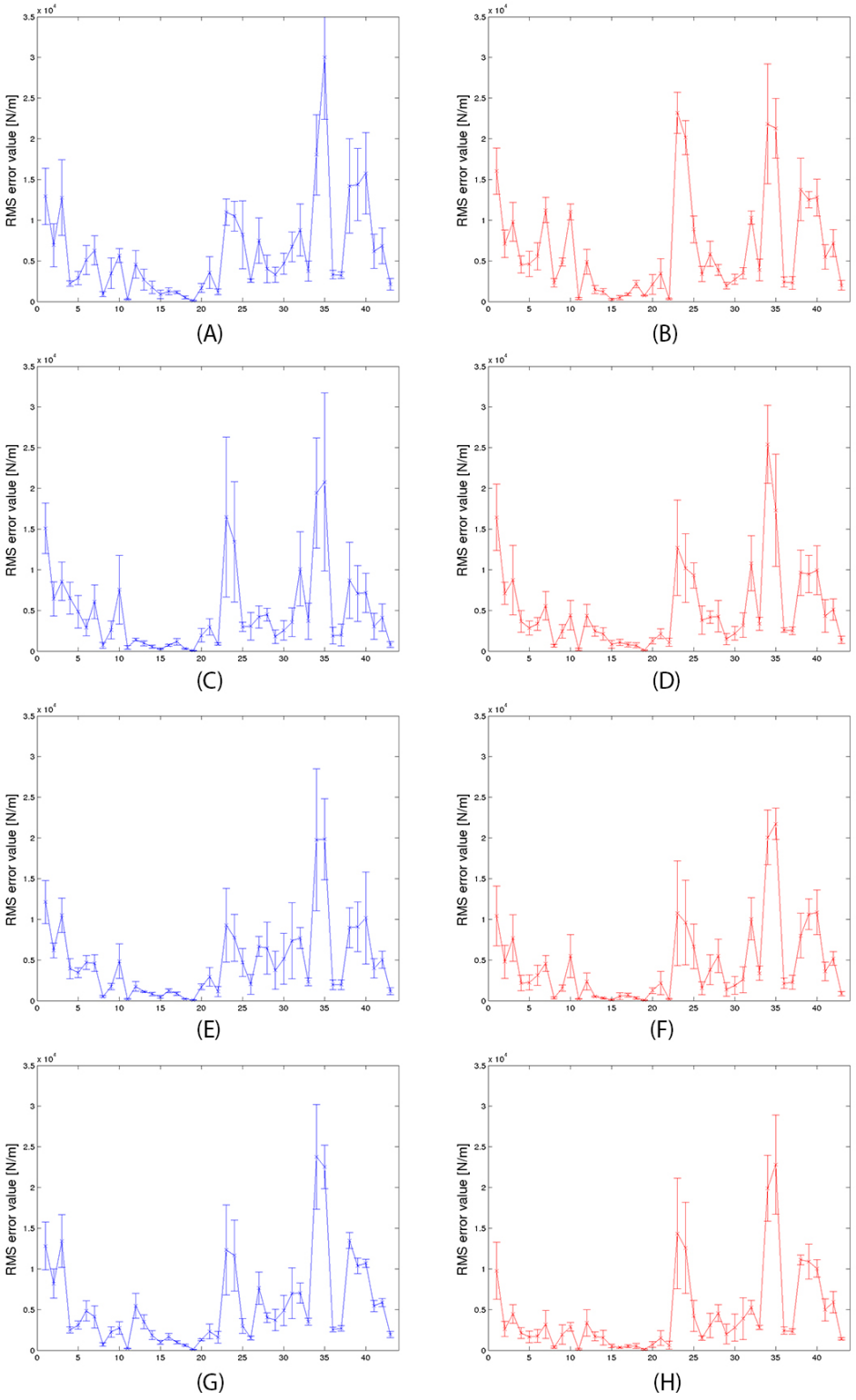

FIGURE 4.16: Root-Mean-Square (RMS) Errors. It has been computed for each muscle, of each subject (from top to bottom: GIL01, GIL02, GIL06, GIL08). On the left side (Graph A, C, E, G) the values of right leg. On the right side (Graph B, D, F, H) the values of left leg.

4.4 Robot mechanical parameter estimation

The virtual model of the robot was tested in a number of ways to determine the stability of the system. The hips were moved to a variety of positions in the simulation and then allowed to move freely. Among the number of tests, the assembly was moved into a squatting position where the center of the hips was located about 110 mm below the equilibrium position (Z = 0), as shown in Fig. 4.17. Furthermore, the implement was dropped onto the floor from about 50 mm, as shown in Fig. 4.18.

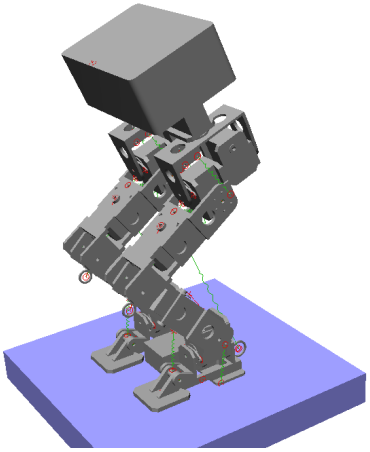

FIGURE 4.17: Initial squatting position.

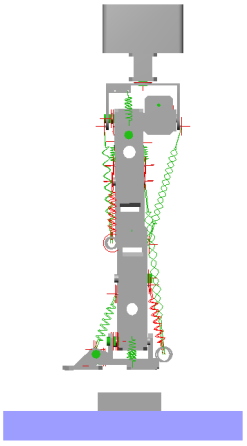

FIGURE 4.18: Initial 50 mm drop position.

With respect to the evaluation of the theoretical model, in all tests where the virtual model did not initially tip over, the assembly returned to its original position. During the squat test, after the model was released, the hip's location moved back to its standing position within 2 seconds, as shown in Fig. 4.19. For the drop test, after the initial shock subside, the assembly remained standing in its position. These tests showed that the theoretical model was robust enough to initial displacements, maintaining its equilibrium position, as shown in Fig. 4.20.

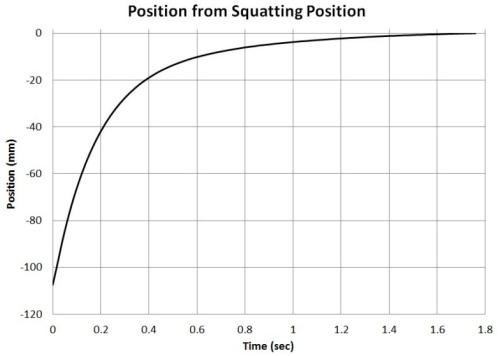

FIGURE 4.19: Hip position returning to equilibrium position after squat movement.

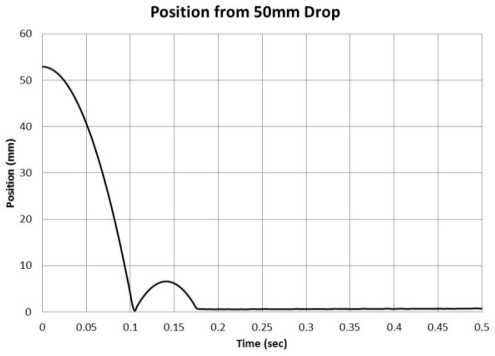

FIGURE 4.20: Vertical displacement of hips from 50 mm drop onto floor.

Within SimWise 4D, the robot position was also perturbed by sliding the ground of 25 mm, in order to observe the waist angular displacement with respect to the ankle joint. The input perturbation and the corresponding waist displacement were then used within the previously described Extended Kalman Filter (EKF) (Subsection 3.6.3) in order to estimate the viscoelastic properties (i.e., damping and stiffness coefficients) of the ankle joint. Given this input perturbation, the last plot of Fig. 4.21 shows the obtained damping [Ns/m] and stiffness [Nm/rad] coefficients. They appear to be underestimated relative to the reference profiles obtained from Eq. 3.42 that are 0.96 Ns/m and 3.45 Nm/rad, respectively. The waist displacement, tracked with a RMSE of 0.0074 rad, ranges from -0.19 rad to -0.08 rad at its maximum, and reaches the minimum displacement of 0.0044 rad in 10.2 seconds.

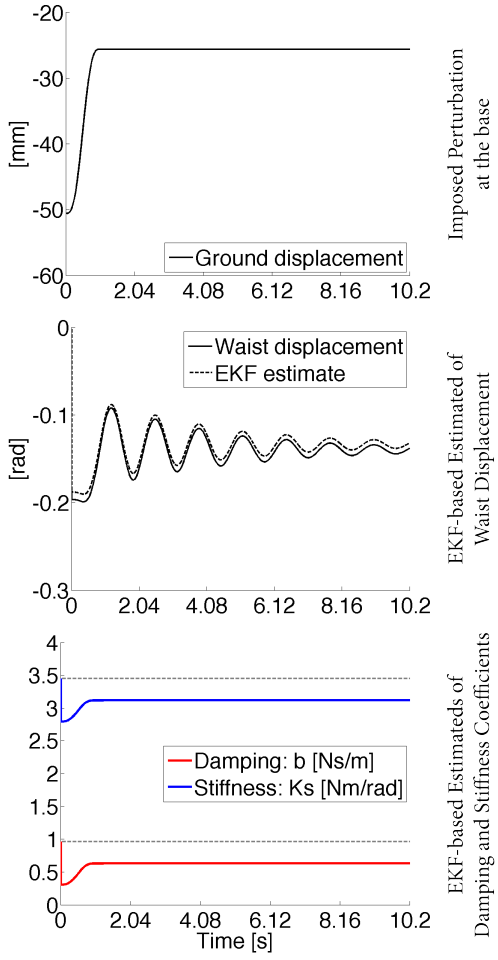

FIGURE 4.21: Simulation Test

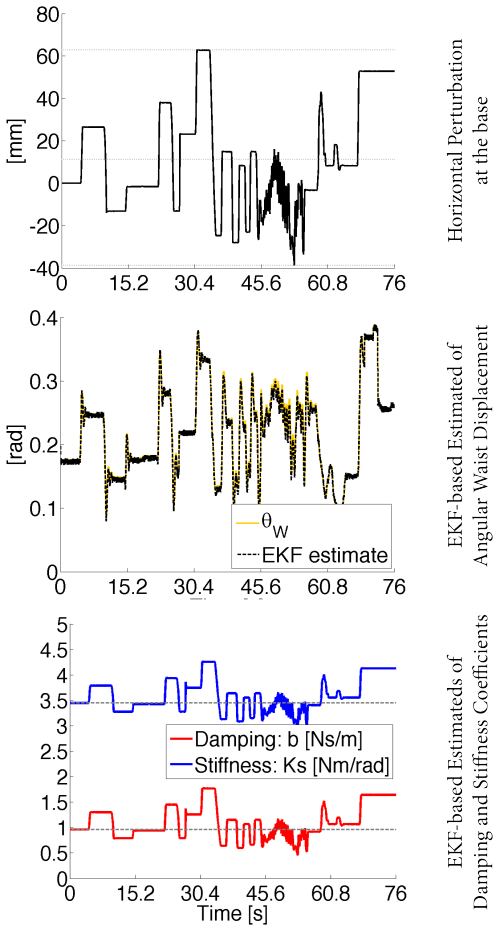

FIGURE 4.22: Real Robot Test

A second evaluation was conducted on the real robot, by placing it on a mobile base and moving it as in the same fashion of the simulation. The position of the robot COM was measured using the Tracker Video Analysis and Modeling Tool from a web-camera recording (Section 3.6), as illustrated in Fig. 4.23. The horizontal perturbation of the base [mm], the corresponding EKF-based estimates of the waist angular displacement [rad] computed with respect to the ankle,

and finally the obtained damping [Ns/m] and stiffness [Nm/rad] coefficients are provided in Fig. 4.22. The RMSE between tracked angle and estimates was of 0.0052 rad (i.e., about 0.3 deg). In this case, both coefficients move around the reference values. The horizontal sections, visible in both profiles, correspond to a joint angle $\theta = 0$. It should be noted that while the stiffness of the springs around the ankle are constant, the moment arm of the spring changes as function of θ and therefore a change in the stiffness is to be expected. Furthermore, there exist a slight play of the ankle mechanism where the assembly does not return to $\theta = 0$ after every perturbation therefore producing a bias in the estimation of stiffness and damping. The high-frequency movement observable in Fig. 4.22 are mainly due to the imposed perturbation. Since, the exact damping of the system is not really known a priori, it was assumed to be less than the critical damping. This hyphotesis is confirmed by the fact that the damping is lower than the guess. If it was higher the system would not oscillate.

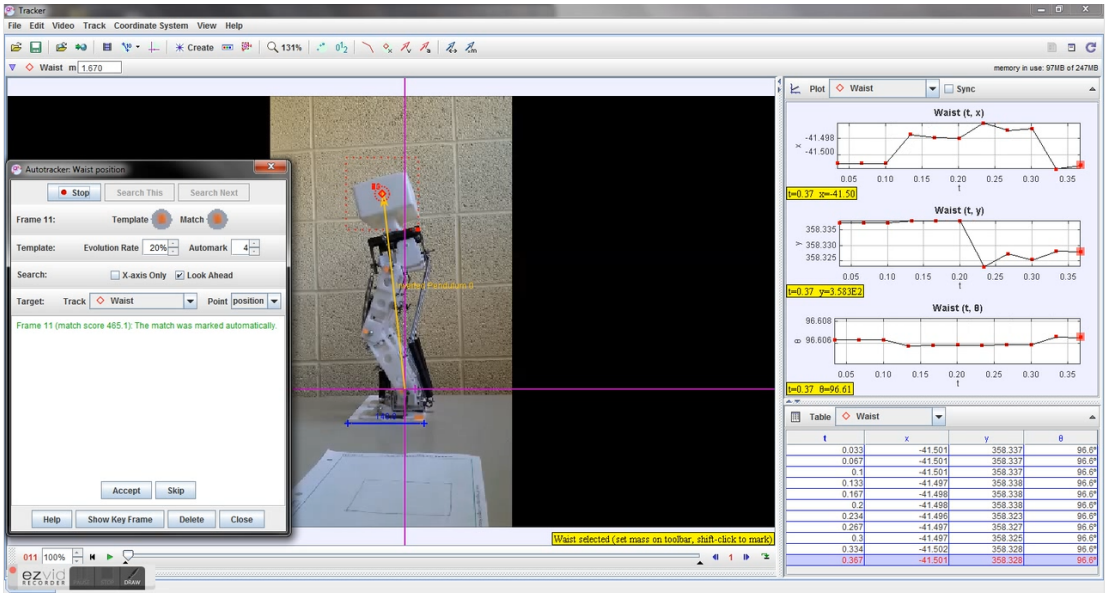

FIGURE 4.23: Screenshot of the robot COM estimation procedure applied to a video recording of the experiment.

A third evaluation was conducted, in OpenSim, to compare the execution of a simple locomotion task (i.e., walking) between human and robot. The kinematics of each body that makes up the robot model was analyzed to obtain the corresponding joint angle between human and robot, in order to estimate the joint displacement error with respect to the imposed trajectory. Then, the attention was focused on the estimated joint stiffness comparing human and robot.

The human joint stiffness was normalized with respect to the weight of the subject to have a direct term of comparison with the robot. Based on the estimated human joint stiffness, several experiments were performed to evaluate the performance of our elastic robot as a function of the different settings. Eight different stiffness constants were applied to all the springs of the system: 0.005 N/mm, 0.010 N/mm, 0.015 N/mm, 0.020 N/mm, 0.025 N/mm, 0.030 N/mm, 0.035

N/mm and 0.040 N/mm. These constants were chosen empirically as they better represented the normalized joint stiffness of the adopted human model. For each of the stiffness constants four sets of spring resting lengths were imposed, starting from the spring lengths provided in Table 3.4 and varying in the range ± 10 mm. The stiffness of the robot was derived using the same algorithm described for the human (Subsection 3.4.3). The torque of the motors divided by the moment arm constituted the active force, and the springs were passive elements much like the tendons in humans.

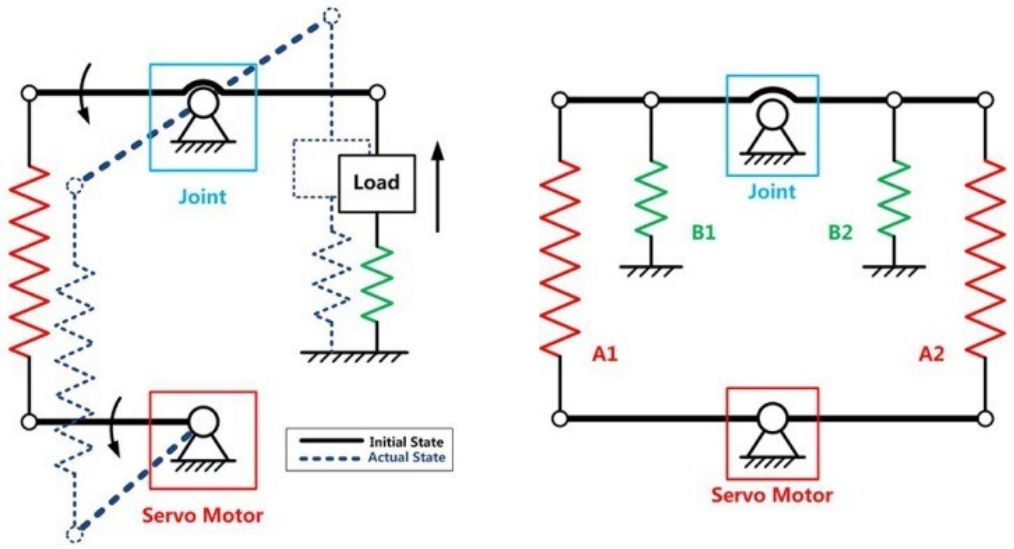

(a) Motor-Spring working principle (b) Active and Passive Springs

FIGURE 4.24: Scheme of the two types of connection for the spring: either to the motor or to the body. It was defined *active* a spring connected between a motor and a link and *passive* a spring connected between two segments.

Within OpenSim, the robot model was equipped with additional bundles connected to a set of virtual motors that actuated the robot by pulling the springs and therefore move the links. Two types of connection between springs and motors were considered (Fig. 4.24): (A) a single spring connection, where only one spring connected to a motor and a link is extended when the motor is in use. The force generated is used to restore the spring original length and therefore pull the load. (B) A spring-pair connection, where a servo motor connects with a joint via two springs, one on each side of the joint. Thus reproducing an agonist-antagonist muscle behavior similar to the correspondent one in a human limb. In this context, a spring connected between a motor and a link (i.e., A1 and A2 in Fig. 4.24(b)) was defined *active*, while a spring not directly connected between a motor and a link (i.e., B1 and B2 in Fig. 4.24(b)) was defined *passive*. Using this formalism, the typical behavior that characterize the human muscle, based on agonist-antagonist and / or flexion-extension pairs, can be reproduced through an artificial structure. The motors were strategically placed to pull the springs.

Both the simulations of the robot using 0.015 N/mm and 0.025 N/mm stiffness constant guarantee the same tracking of the hip and knee trajectories and are overlapping in the following graphs (Fig. 4.25(A)). The difference of hip angle between robot and human is minimal, with a maximum error of 11° at heel down. An oscillatory trend of the profile related to the robot (i.e., red solid line) can be noticed starting with the impact of the foot with the ground. This phenomenon is most likely derived from the difference in inertia of the torso between the two models. The lighter torso of the robot cannot act as a low pass filter as in the case of the human; thus, transmitting some higher frequency vibration to the lower body. The knee joint angle is tracked much more smoothly (Fig. 4.25(B)), even though the deviation from the human reference can be substantial just right before the swing phase (i.e., 25°).

Fig. 4.25(C) shows the kinematic analysis of the ankle joint. In this particular joint the choice of stiffness and resting length for the springs is much more important. A wide range of variability related to the different setup considered can be noticed. Substantial fluctuations emerge in the stages of transition from single to double support and vice versa, as well as an obvious difficulty to correctly track the angle that characterizes the human ankle joint (i.e., green solid line). This discrepancy can derive from the substantial difference in foot size between robot and human. The former has much larger feet to help maintain stability and redistribute the weight on the ground.

The elements on the joint stiffness matrix's diagonal are depicted in Fig. 4.26(A-C) as a function of the gait cycle. The best tracking results are obtained using 0.015 N/mm and 0.025 N/mm stiffness constants at the spring level. Stiffness tracking is quite accurate, and in particular, the shorter length of the spring corresponds with their resting length. The hip and ankle stiffness are comparable, while the knee's stiffness is lower, and about half in magnitude. The stiffness of the hip has little variation with respect to the different phase of the gate cycle (Fig. 4.26(A)). Knee's stiffness starts high with an absolute maximum immediately after the heel strike for then decreasing throughout the movement (Fig. 4.26(B)). Ankle's stiffness is the highest of all, showing a marked maximum in mid-cycle where the double support phase occurs (Fig. 4.26(C)).

The elements of the joint stiffness matrix located outside of the diagonal are presented in Fig. 4.27(A-B). Since, it was found to be symmetric, only the upper part of the matrix is represented here. The hip-ankle inter-joint stiffness was found to be zero. This is the direct consequence of not having any triarticular muscles spanning between such two joints. There is a noticeable difference in magnitude between the hip-knee and knee-ankle inter-joint stiffness where the latter has a much lower magnitude.

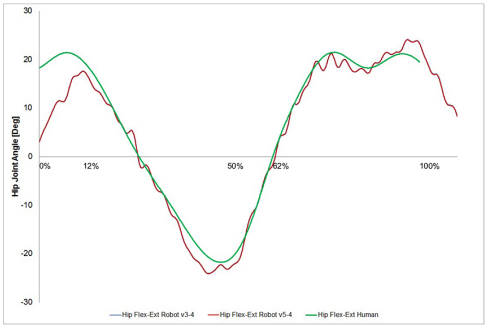

(A)

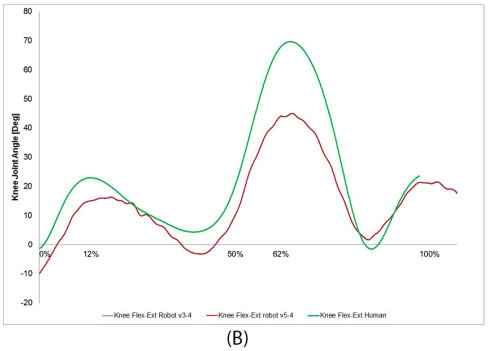

(B)

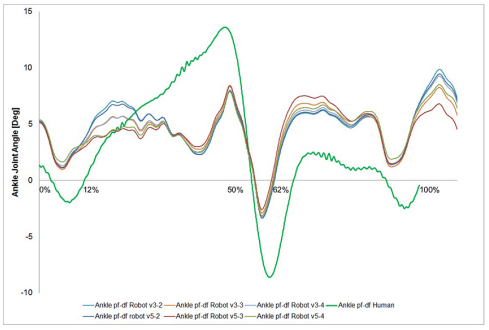

(C)

FIGURE 4.25: Comparison of obtained joint angles.

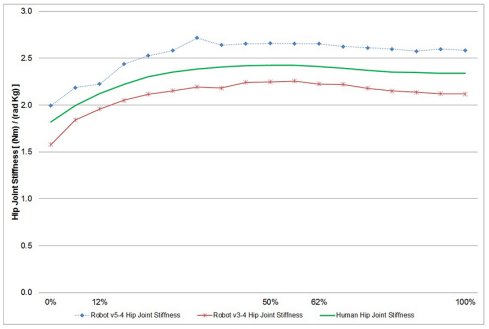

(A)

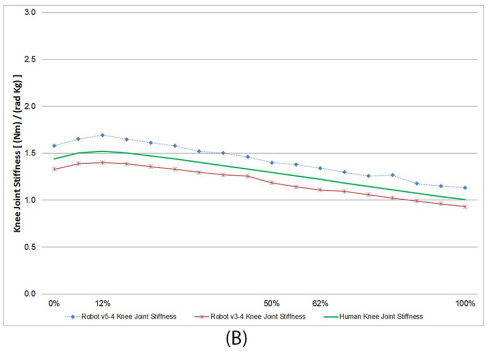

(B)

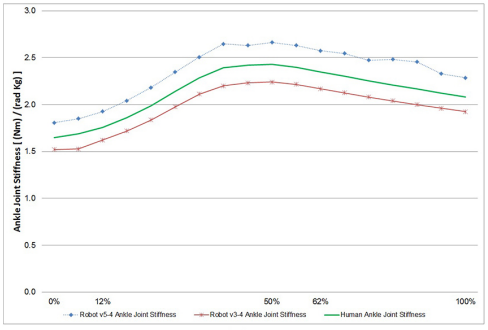

(C)

FIGURE 4.26: Comparison of the estimated robot joint's stiffness

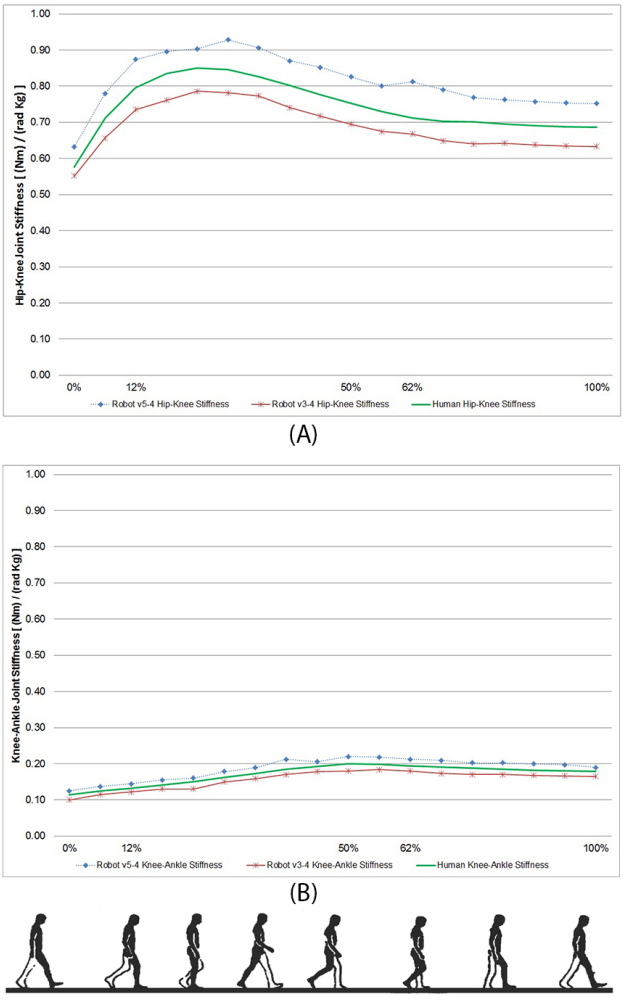

FIGURE 4.27: Comparison of the estimated robot inter-joint's stiffness with respect to the reference value obtained from the human model. (A)Hip-Knee Joint Stiffness relation. (B) Knee-Ankle Joint Stiffness relation.

Chapter 5

Discussion and Conclusion

This work presents a physiologically accurate and computationally fast novel Neuromusculoskeletal (NMS) model of the human lower limb musculotendon and joint *stiffness* and *quasi-stiffness*. The proposed computational framework uses Electromyographic (EMG) signals, Motion Capture (MC) data and Ground Reaction Forces (GRFs) to predict the force developed by 43 musculotendon actuators. The estimated forces are then used to compute the musculotendon stiffness and the corresponding joint stiffness and quasi-stiffness. The estimations at each Musculotendon Unit (MTU) is constrained to simultaneously satisfy the joint angles and the joint moments generated with respect to five Degrees Of Freedom (DOFs), including: Hip Adduction-Abduction (HipAA), Hip Flexion-Extension (HipFE), Hip Internal-External Rotation (HipIER), Knee Flexion-Extension (KneeFE), and Ankle Plantar-Dorsi Flexion (AnklePDF).

Advanced methods were used to perform accurate muscle-driven dynamic simulations based on two public available datasets (Section 3.1). In particular, a generic three-dimensional model of the human musculoskeletal structure was scaled to the anthropometric characteristics of each subject involved in the study (Subsection 3.2.2). Each resulting model was adjusted using the Residual Reduction Analysis (RRA) in order to guarantee the dynamic consistency between kinematic and kinetic data (Subsection 3.2.4). Finally, the aforementioned physiological and mechanical parameters were estimated using two different optimization techniques, namely Static Optimization (SO) and Computed Muscle Control (CMC), as well as using two different implementation of the Hill-type muscle force model, in order to evaluate the effects of using kinematic constraints and Force-Length-Velocity-Activation (FLVA) physiological properties in muscle force optimization solutions (Subsection 3.3). Finally, the proposed computational framework was validated on the first dataset (Section 4.1) with respect to the possibility of providing a physiologically sound estimation of joint stiffness and quasi-stiffness, in order to characterize the mechanical properties of the whole limb during normal gait cycle at different speeds. The focus was on the neuromuscular mechanisms regulating these mechanical parameters during the

stance phase of walking. On the other hand, with respect to the second dataset (Section 4.2), the focus was on the use of a pure SO and CMC solutions computed with ideal force generators, with physiological FLVA properties, and with different sets of reserve actuators.
This research provides effective solutions and readily available software tools to improve the human interaction with robotic assistive devices, advancing the research in neuromusculoskeletal modeling to better understand the mechanisms of actuation provided by human muscles and the rules that govern the lower limb joint stiffness regulation. The obtained results suggest that the neuromusculoskeletal modeling technology can be exploited to address the challenges on the development of musculoskeletal humanoids, new generation human-robot interfaces, motion control algorithms, and intelligent assistive wearable devices capable to effectively ensure a proper dynamic coupling between human and robot.

5.1 The role of Stiffness and Quasi-Stiffness

Several studies have already investigated the moment-angle relationship (i.e., quasi-stiffness) for single lower limb joint during walking, running and sprinting. Butler et al. [22] provided a current update of the lower extremity stiffness literature as it pertains to both performance and injury. Winter et al. [135] showed that the torque-angle relationship dominates behavior near the movement operating-range extremes, and the excitation and activation processes are most significant for fast voluntary movements. Shamaei et al. [26] investigated the hip behavior in each stage of stance phase using the slope of a linear fit to the moment-angle graph in that stage and name it the quasi-stiffness of that particular stage. For the examined gait trials, whose speed varies in the range 0.75-1.75 m/s, the estimated quasi-stiffness ranging from a minimum value of 91 Nm/rad to a maximum of 1775 Nm/rad during extension, and from a minimum of 9 Nm/rad to 1400 Nm/rad during flexion. G*ü*nther and Blickhan [136] reported that the knee joint is always stiffer and more extended than the ankle joint. Moreover, the knee torque characteristic on the average shows the higher nonlinearity. Stefanyshyn and Nigg [137] investigated the moment-angle relationship of the ankle joint during running and sprinting. The results indicated that the average quasi-stiffness of the ankle joint was 5.68 Nm/deg during running and 7.38 Nm/deg during sprinting. Loram and Lakie [138] executed direct measurement of human ankle stiffness during quiet standing, showing that the stiffness was substantially constant, increasing only slightly with ankle torque. Their measurement suggested that the triceps surae muscles maintain balance via a spring-like element which is itself too compliant to guarantee stability. For this reason, it seems that the brain cannot set ankle stiffness and then ignore the control task because additional modulation of torque is required to maintain balance. They suggested that the triceps surae muscle maintain balance by predictively controlling the proximal offset of the spring-like element in a ballistic-like manner. Rouse et al. [139] investigated the sensitivity of ankle stiffness

measurements while standing to foot placement on a perturbator robot. The stiffness estimates ranged from 2.6 to 3.1 Nm/rad/kg. Plocharski and Plocharski [140] investigated the ankle stiffness in dynamic conditions during walking. The highest value of stiffness was found during an isometric trial with a plantarflexion perturbation (1282±1028 Nm/rad, at 41 ms after the perturbation onset) and at the exact same timing during the dynamic trial (707±802 Nm/rad). On the other hand, during the hold-release time, both the isometric and dynamic stiffness values were within a close range of each other (859±519 Nm/rad and 877±678 Nm/rad, respectively). Lee and Hogan [141] investigated the ankle impedance from pre-swing through swing to early stance, by using a wearable ankle robot and a modified linear time-varying ensemble-based system identification methods. The obtained results showed an ankle joint stiffness ranging from about 10 to 70 Nm/rad. Rouse et al. [32] found that for the stance phase between 20% and 70% of heel strike to toe-off stiffness and quasi-stiffness were unexpectedly similar and increased somewhat monotonically from 2 to 10 Nm/rad/kg.

The same authors proposed also a theoretical work related to the conceptual differences between stiffness and quasi-stiffness [28], experimentally comparing ankle's stiffness and quasi-stiffness for normal gait. However, the present work is the first to produce a quantitative comparison between stiffness and quasi-stiffness variables for multiple joints at the same time, at different speeds during walking and running, investigating how different analyzes performed upstream (i.e., estimation of physiological parameters), affect the estimates of mechanical parameters. Moreover, the quasi-stiffness computation was done at each time frame, instead of considering whole phases of movement as performed in the aforementioned studies. This allowed us to provide a more in-depth analysis of the relationship between stiffness and quasi-stiffness. Our estimation produced similar order of magnitude of stiffness for velocities similar to those tested in literature. Moreover, the quasi-stiffness calculated in this work shows different magnitude and profile with respect to the stiffness, supporting our hypothesis based on which stiffness and quasi-stiffness have two different reference points (Subsection 3.4.3). Given the oscillatory behavior of the leg during gait, an increase in cadence maintaining the step-length constant increases not only the velocity but the acceleration of the body segments around the joints. This requires an increase in torque and, as a consequence, both quasi-stiffness and stiffness should increase since they are directly dependent upon the muscles' force generating the torque at the joints. The shape of the stiffness profiles is consistent among walking velocities; however, its magnitude does not increase monotonically as a function of the velocity. The increase of velocity is usually associated with the increase in muscle activation; however, such increase of muscle force/activation is not strictly associated with a monotonic increase in stiffness during movement as demonstrated for the upper limb by [142]. By observing Eq. 3.19, we can understand that quasi-stiffness is a non-linear function. The use of quasi-stiffness as open-loop control variable might be convenient when the movement can be approximated as quasi-static. Thus, the effect of inertial and Coriolis forces are negligible and the gravitational effect can be linearized for small displacements. As

the velocity and acceleration increase, controlling the trajectory using quasi-stiffness becomes more difficult and a linearized feedback control might be easier to apply.

With respect to the use of optimization solutions in muscle force computation, recent works [42, 51] highlighted the similarities between static and dynamic optimization techniques for the estimation of lower limb dynamics during bipedal locomotion at speed comprised between 1.2 and 3.5 m/s. The present work produced a quantitative comparison between SO and CMC estimates of joint torques and joint stiffness during running at speeds higher than 3.5 m/s. Our results are in accordance with the results presented in [50] for lower speeds. The use of FLVA muscle properties seem to have little influence on the static optimization solutions during running movements. However, the joint stiffness estimates show a significant differences when comparing the results obtained with the two approaches. When looking at movement performance, some level of stiffness is required in order to guarantee an efficient utilization of the stored elastic energy in the musculoskeletal system that occurs during the loading phase of movement [22]. As previously discussed, the amount of stiffness required has been reported to increase with the velocity of the activity. This increase in stiffness may be necessary to maintain the stability of the posture during the landing phase and allows for maximum energy return during the propulsive phase. Following this reasoning, and evaluating the aforementioned mean stiffness and quasi-stiffness values provided in literature for the knee and ankle joints, it seems that the SO approach under-estimates muscle forces when employed in the analysis of motor tasks characterized by rapid movements. This in turn under estimate the joint stiffness. It can be speculated that the SO does not account for the large spectrum of muscle co-contraction typically observed during the execution of different motor tasks such as walking and running [143]. The obtained results suggest that the CMC approach is preferable when is need to analyze a relatively fast movement. In this regard, it is also worth noting that the CMC algorithm solves the problem of muscle force distribution for known movement kinematics, based on a control algorithm that tracks the kinematics of a measured movement. This method is much faster than dynamic optimization approaches, because it requires only one forward integration of the state equations. Despite the fact that to solve the muscle redundancy, it still requires the use of an instantaneuous cost function (i.e., in opposition to dynamic optimization, the use of a time-integral cost function such as total metabolic cost is not possible), it efficiently enforces the musculoskeletal system dynamics.

5.2 Remarks on the preliminary results

The first consideration regards the use of different implementations of the Hill-type muscle model for estimating the lower limb joint stiffness during the running of an unimpaired individual. Results show that the choice of the muscle model influences the estimation of the muscle-tendon

stiffness and of the corresponding joint stiffness. It can be speculated that the difference in results depends on the contraction dynamics of the tendon which is implemented differently in the two models. This suggests that the force interaction between contractile elements and tendon are important factors as suggested by [117]. Future research will focus on providing a better characterization of the existing relationships between muscle models and stiffness estimation procedures, by analyzing also the behavior of muscle-tendon actuator models that is not based on classical Hill models (e.g., such as *Millard2012AccelerationMuscle*[1] [144]). This investigations might potentially be applied to the assessment of patient's muscle stiffness as function of muscle dynamics, so to properly plan the rehabilitation process.

On the other hand, with respect to the use of a probabilistic technique, namely Gaussian Mixture Model (GMM), for estimating the muscle-tendon stiffness of the human lower limb, the model was described and evaluated by using the first dataset (Section 4.1). The proposed approach took into account a set of analytical techniques proposed in literature in order to describe the uncertainty related to measurements of human physiological parameters in a probabilistic manner. In this regard, it should be stressed that the proposed GMM-based approach is able to estimate muscle-tendon stiffness as function of the *gait phase*, just via a probabilistic extrapolation of data collected at different speeds, avoiding the need for those variables that cannot be measured in-vivo. Results showed a positive trend with an acceptable error (amounting to an order of magnitude less compared to the dispersion of the measured dataset) especially for the muscles particularly involved in the task. As a future work, further studies regarding the influence of muscle models on impedance calculation, and the algorithms used for muscle forces estimation during movement are needed. Moreover, the GMM-based approach can be also exploited to account for failed demonstrations, in order to estimate the stiffness during the rehabilitation process of impaired individuals from data collected on able-bodied subjects. The aim is to improve the capability of this technique to characterize the cause-effect relationships between neuromuscular excitation patterns, muscle forces, and motions of the body and still have a limited amount of parameters to not over-fit the data.

5.3 Thoughts on the Locomotive Underactuated Implement Guided via Elastic Elements (L.U.I.G.E.E.)

The major contribution, with respect to the design, simulation and prototyping of L.U.I.G.E.E., is related to the realization of an artificial apparatus capable to maintain a quiet standing position using only a completely passive elastic actuation structure.

It should be noted that the system is not a simple inverted pendulum but has many more DOFs.

[1] https://simtk.org/api_docs/opensim/api_docs30/classOpenSim_1_1Millard2012AccelerationMuscle.html

The system was carefully designed so that the combination of springs spanning multiple joints acts as if the system was a global elastic structures. Stability is not guaranteed in such a type of system because the knees could buckle and the change in the moment arm at the spring that cross the knee could directly impact the stiffness at the ankle. To date very few robotic devices implement an elastic mechanical-network. Most of these devices are actuated by SEA [145]. The control of SEA can be difficult because the elastic elements positioned in series introduce a delay in the actuation that the control needs to compensate for. This problem can be solved by a predictive control strategy (e.g., Smith predictor [146]) given an accurate knowledge of the plant. This work is part of a larger project that aims to propose a control architecture using *Parallel Elastic Actuators* [147]. Thus, the maintenance of posture and the control of gait can be achieved via two separate control architectures.

In this installment, the mechanical properties of the passive elastic network, allowing the bipeds to stand and compensate for external perturbation, were estimated. The robot was excited at its base and the stiffness and damping at the ankle was estimated using an EKF. The methodology utilized here is similar to the one used for the estimation of the same physiologically relevant parameter in humans [132]. The EKF is ideally suited for this operation because it is capable of handling both noisy measurements of input and output, as well as modeling errors of the mechanical structure. It is important to notice that, even though passive, the control system is able to maintain the system in equilibrium after perturbations up to 25% of its height. Furthermore, even though the springs were not damped, the elastic network produces a damped response. This behavior was previously reported for pre-tensioned structures in [18], where muscle co-contraction was found to modulate damping in a multi-link biomechanic limb.

The mechanical properties of the proposed elastic network and the corresponding joint stiffness of our model, normalized with respect to the mass, were also compared with simulations of a human walking at a self-selected pace, with a speed of the latter of about 1 m/s. The stiffness of the springs implemented on the robot, necessary to replicate the normalized human stiffness during walking, was found to be drastically lower than the stiffness necessary to maintain a stable static balance. Even though additional springs were added on specific muscles groups for the simulation of walking, the overall parallel stiffness of the humanoid's muscle groups during walking was one order of magnitude lower than that necessary to stand. This result could be a consequence of multiple factors. First, *mass* might not be an appropriate parameter for the normalization of stiffness. Other physical parameters such as the moment of inertia of the whole body with respect to the ankle could be a better normalization factor. Second, assuming mass as an appropriate normalization factor, a low joint stiffness during locomotion, incapable of stabilizing standing could suggest that there might be other stabilization effects at play which might be of inertial origin. The human has a higher mass and a higher walking speed in absolute values which could give the subject enough momentum to stabilize locomotion. Third, human could use a set of control strategies that is not reflected in the modulation of joint stiffness that might

be controlled by the vestibular system. To account for the variation in stiffness between standing and locomotion springs could be made with new shape memory alloys where the stiffness could be varied by means of heat or electrical effects; however, these solutions tends to be quite expensive and the stiffness of the spring difficult to control. These limitations, notwithstanding constant spring stiffness, allows for the possibility to obtain joint stiffness profiles during locomotion that varies with time. Even if we assume that the moment arms of the spring do not vary considerably as a function of the joint angles, we can approximate any torque-angle profile with a series of linear change in torque at different angles. This could be obtained with a series of springs with different moment arms acting within limited angular segments. One of the biggest advantages of the elastic network proposed here is the possibility to render *out of diagonal* terms of the joint stiffness matrix that would be impossible with a classical direct drive of the links using a motor. In the future, the work will be carried on by investigating the aforementioned open issues, by improving the viscoelastic characterization of the whole assembly, and by introducing motors, control modules and sensors so that L.U.I.G.E.E. can move its first steps forward.

Bibliography

[1] R. Bortoletto, L. Tonin, E. Pagello, and E. Menegatti, "ICT for new generation prostheses," in *Neuro-Rehabilitation with Brain Interface*, 2015th ed., L. P. Ligthart, R. Prasad, and S. Pupolin, Eds. River Publishers, 2015, pp. 21–50.

[2] D. M. Wolpert and Z. Ghahramani, "Computational principles of movement neuroscience," *Nat. Neurosci.*, vol. 3, pp. 1212 – 1217, 2000.

[3] M. A. Akhras, R. Bortoletto, F. Madehkhaksar, and L. Tagliapietra, "Neural and Musculoskeletal Modeling: Its Role in Neurorehabilitation," in *Emerg. Ther. Neurorehabilitation II*, ser. Biosystems & Biorobotics, J. L. Pons, R. Raya, and J. González, Eds. Springer International Publishing, 2016, vol. 10, pp. 109–143.

[4] R. Barlett, *Introduction to Sports Biomechanics - Analysis of Human Movement Patterns*, 2nd ed., Routledge, Ed. Taylor & Francis e-Library, 2007.

[5] N. Bernstein, *The co-ordination and regulation of movements*. Pergamon Press, 1967.

[6] J. J. Kutch and F. J. Valero-Cuevas, "Challenges and new approaches to proving the existence of muscle synergies of neural origin." *PLoS Comput. Biol.*, vol. 8, no. 5, p. e1002434, Jan. 2012.

[7] J. Pelleg, *Mechanical Properties of Materials*. Springer Netherlands, 2013.

[8] D. Piovesan, A. Pierobon, P. DiZio, and J. R. Lackner, "Measuring multi-joint stiffness during single movements: numerical validation of a novel time-frequency approach." *PLoS One*, vol. 7, no. 3, p. e33086, Jan. 2012.

[9] E. J. Perreault, L. Hargrove, D. Ludvig, H. Lee, and J. Sensinger, "Considering Limb Impedance in the Design and Control of Prosthetic Devices," in *Neuro-Robotics*, ser. Trends in Augmentation of Human Performance, P. Artemiadis, Ed. Dordrecht: Springer Netherlands, 2014, vol. 2, pp. 59–83.

[10] F. Mussa-Ivaldi, N. Hogan, and E. Bizzi, "Neural, mechanical, and geometric factors subserving arm posture in humans." *J. Neurosci.*, vol. 5, no. 10, pp. 2732–43, Oct. 1985.

[11] M. L. Latash and V. M. Zatsiorsky, "Joint stiffness: Myth or reality?" *Hum. Mov. Sci.*, vol. 12, no. 6, pp. 653–692, Dec. 1993.

[12] J. McIntyre, F. Mussa-Ivaldi, and E. Bizzi, "The control of stable postures in the multijoint arm," *Exp. Brain Res.*, vol. 110, no. 2, Jul. 1996.

[13] E. J. Perreault, R. Kirsch, and P. Crago, "Effects of voluntary force generation on the elastic components of endpoint stiffness," *Exp. Brain Res.*, vol. 141, no. 3, pp. 312–323, Dec. 2001.

[14] J. L. Oliver and P. M. Smith, "Neural control of leg stiffness during hopping in boys and men." *J. Electromyogr. Kinesiol.*, vol. 20, no. 5, pp. 973–9, Oct. 2010.

[15] D. R. Lametti, G. Houle, and D. J. Ostry, "Control of movement variability and the regulation of limb impedance." *J. Neurophysiol.*, vol. 98, no. 6, pp. 3516–24, Dec. 2007.

[16] D. P. Ferris, M. Louie, and C. T. Farley, "Running in the real world: adjusting leg stiffness for different surfaces." *Proc. Biol. Sci.*, vol. 265, no. 1400, pp. 989–94, Jun. 1998.

[17] N. Hogan, "The mechanics of multi-joint posture and movement control," *Biol. Cybern.*, vol. 52, no. 5, pp. 315–331, Sep. 1985.

[18] S. Heitmann, N. Ferns, and M. Breakspear, "Muscle co-contraction modulates damping and joint stability in a three-link biomechanical limb." *Front. Neurorobot.*, vol. 5, p. 5, Jan. 2011.

[19] J. Winters and L. Stark, "Analysis of fundamental human movement patterns through the use of in-depth antagonistic muscle models." *IEEE Trans. Biomed. Eng.*, vol. 32, no. 10, pp. 826–39, Oct. 1985.

[20] F. E. Zajac and J. Winters, "Modeling Musculoskeletal Movement Systems: Joint and Body Segmental Dynamics, Musculoskeletal Actuation, and Neuromuscular Control," in *Mult. Muscle Syst.*, J. M. Winters and S. L.-Y. Woo, Eds. New York, NY: Springer New York, 1990, ch. 8, pp. 121–148.

[21] D. A. Winter, *Biomechanics and Motor Control of Human Movement.* John Wiley & Sons, Inc., 2009.

[22] R. J. Butler, H. P. Crowell, and I. M. Davis, "Lower extremity stiffness: implications for performance and injury." *Clin. Biomech. (Bristol, Avon)*, vol. 18, no. 6, pp. 511–7, Jul. 2003.

[23] K. Shamaei, G. S. Sawicki, and A. M. Dollar, "Estimation of quasi-stiffness of the human knee in the stance phase of walking." *PLoS One*, vol. 8, no. 3, p. e59993, Jan. 2013.

[24] K. Shamaei, G. S. Sawicki, and A. M. Dollar, "Estimation of quasi-stiffness of the human hip in the stance phase of walking," *PLoS One*, vol. 8, no. 12, 2013.

[25] A. Azaman and S.-I. Yamamoto, "Estimation of stiffening strategy of ankle and hip based on joint sway," in *2013 6th Int. IEEE/EMBS Conf. Neural Eng.* IEEE, Nov. 2013, pp. 1554–1557.

[26] K. Shamaei, G. S. Sawicki, and A. M. Dollar, "Estimation of Quasi-Stiffness and Propulsive Work of the Human Ankle in the Stance Phase of Walking," *PLoS One*, vol. 8, no. 3, 2013.

[27] A. Hansen, D. Childress, S. Miff, S. Gard, and K. Mesplay, "The human ankle during walking: implications for design of biomimetic ankle prostheses." *J. Biomech.*, vol. 37, no. 10, pp. 1467–74, Oct. 2004.

[28] E. J. Rouse, R. D. Gregg, L. J. Hargrove, and J. W. Sensinger, "The difference between stiffness and quasi-stiffness in the context of biomechanical modeling." *IEEE Trans. Biomed. Eng.*, vol. 60, no. 2, pp. 562–8, Feb. 2013.

[29] S. Pfeifer, M. Hardegger, H. Vallery, R. List, M. Foresti, R. Riener, and E. J. Perreault, "Model-based estimation of active knee stiffness," in *2011 IEEE Int. Conf. Rehabil. Robot.* IEEE, Jun. 2011, pp. 1–6.

[30] S. Pfeifer, H. Vallery, M. Hardegger, R. Riener, and E. J. Perreault, "Model-based estimation of knee stiffness." *IEEE Trans. Biomed. Eng.*, vol. 59, no. 9, pp. 2604–12, Sep. 2012.

[31] E. J. Rouse, L. J. Hargrove, E. J. Perreault, and T. A. Kuiken, "Estimation of human ankle impedance during walking using the perturberator robot," in *2012 4th IEEE RAS EMBS Int. Conf. Biomed. Robot. Biomechatronics.* IEEE, Jun. 2012, pp. 373–378.

[32] E. J. Rouse, L. J. Hargrove, E. J. Perreault, and T. A. Kuiken, "Estimation of human ankle impedance during the stance phase of walking." *IEEE Trans. Neural Syst. Rehabil. Eng.*, vol. 22, no. 4, pp. 870–8, Jul. 2014.

[33] S. L. Delp, F. C. Anderson, A. S. Arnold, P. Loan, A. Habib, C. T. John, E. Guendelman, and D. G. Thelen, "OpenSim: open-source software to create and analyze dynamic simulations of movement." *IEEE Trans. Biomed. Eng.*, vol. 54, no. 11, pp. 1940–50, Nov. 2007.

[34] B. J. Fregly, M. L. Boninger, and D. J. Reinkensmeyer, "Personalized neuromusculoskeletal modeling to improve treatment of mobility impairments: a perspective from European research sites." *J. Neuroeng. Rehabil.*, vol. 9, p. 18, Jan. 2012.

[35] M. Sartori, M. Reggiani, D. Farina, and D. G. Lloyd, "EMG-driven forward-dynamic estimation of muscle force and joint moment about multiple degrees of freedom in the human lower extremity." *PLoS One*, vol. 7, no. 12, p. e52618, Jan. 2012.

[36] A. V. Hill, "The Heat of Shortening and the Dynamic Constants of Muscle," *Proc. R. Soc. B Biol. Sci.*, vol. 126, no. 843, pp. 136–195, Oct. 1938.

[37] A. M. Gordon, A. F. Huxley, and F. J. Julian, "The variation in isometric tension with sarcomere length in vertebrate muscle fibres." *J. Physiol.*, vol. 184, no. 1, pp. 170–92, May 1966.

[38] F. E. Zajac, "Muscle and tendon: properties, models, scaling, and application to biomechanics and motor control." *Crit. Rev. Biomed. Eng.*, vol. 17, no. 4, pp. 359–411, Jan. 1989.

[39] M. Pandy, "Computer modeling and simulation of human movement." *Annu. Rev. Biomed. Eng.*, vol. 3, pp. 245–73, Jan. 2001.

[40] F. C. Anderson and M. G. Pandy, "A Dynamic Optimization Solution for Vertical Jumping in Three Dimensions," *Comput. Methods Biomech. Biomed. Engin.*, vol. 2, no. 3, pp. 201–231, Jan. 1999.

[41] A. Erdemir, S. McLean, W. Herzog, and A. J. van den Bogert, "Model-based estimation of muscle forces exerted during movements," *Clin. Biomech.*, vol. 22, no. 2, pp. 131–154, Feb. 2007.

[42] V. Monaco, M. Coscia, and S. Micera, "Cost function tuning improves muscle force estimation computed by static optimization during walking." *Conf. Proc. ... Annu. Int. Conf. IEEE Eng. Med. Biol. Soc. IEEE Eng. Med. Biol. Soc. Annu. Conf.*, vol. 2011, pp. 8263–6, Jan. 2011.

[43] D. G. Lloyd and T. S. Buchanan, "Strategies of muscular support of varus and valgus isometric loads at the human knee." *J. Biomech.*, vol. 34, no. 10, pp. 1257–67, Oct. 2001.

[44] D. G. Lloyd and T. F. Besier, "An EMG-driven musculoskeletal model to estimate muscle forces and knee joint moments in vivo," *J. Biomech.*, vol. 36, no. 6, pp. 765–776, Jun. 2003.

[45] E. Todorov and M. I. Jordan, "Optimal feedback control as a theory of motor coordination." *Nat. Neurosci.*, vol. 5, no. 11, pp. 1226–35, Nov. 2002.

[46] S. H. Scott, "Optimal feedback control and the neural basis of volitional motor control." *Nat. Rev. Neurosci.*, vol. 5, no. 7, pp. 532–46, Jul. 2004.

[47] M. Chhabra and R. A. Jacobs, "Properties of Synergies Arising from a Theory of Optimal Motor Behavior," *Neural Comput.*, vol. 18, no. 10, pp. 2320–2342, Oct. 2006.

[48] D. G. Thelen, F. C. Anderson, and S. L. Delp, "Generating dynamic simulations of movement using computed muscle control." *J. Biomech.*, vol. 36, no. 3, pp. 321–8, Mar. 2003.

[49] D. Piovesan, A. Pierobon, P. Dizio, and J. R. Lackner, "Comparative analysis of methods for estimating arm segment parameters and joint torques from inverse dynamics." *J. Biomech. Eng.*, vol. 133, no. 3, p. 031003, Mar. 2011.

[50] F. C. Anderson and M. G. Pandy, "Static and dynamic optimization solutions for gait are practically equivalent." *J. Biomech.*, vol. 34, no. 2, pp. 153–61, Feb. 2001.

[51] Y.-C. Lin, T. W. Dorn, A. G. Schache, and M. G. Pandy, "Comparison of different methods for estimating muscle forces in human movement." *Proc. Inst. Mech. Eng. H.*, vol. 226, no. 2, pp. 103–12, Feb. 2012.

[52] A. Seth and M. G. Pandy, "A neuromusculoskeletal tracking method for estimating individual muscle forces in human movement," *J. Biomech.*, vol. 40, no. 2, pp. 356–366, Jan. 2007.

[53] K. Yamamoto, M. Ishii, K. Hyodo, T. Yoshimitsu, and T. Matsuo, "DEVELOPMENT OF POWER ASSISTING SUIT : Miniaturization of supply system to realize wearable suit," *Proc. ... Int. Conf. Motion Vib. Control*, vol. 6, no. 2, pp. 848–854, 2002.

[54] J. Pratt, B. Krupp, C. Morse, and S. Collins, "The RoboKnee: an exoskeleton for enhancing strength and endurance during walking," in *IEEE Int. Conf. Robot. Autom. 2004. Proceedings. ICRA '04. 2004*, vol. 3. IEEE, 2004, pp. 2430–2435 Vol.3.

[55] A. Zoss, H. Kazerooni, and A. Chu, "Biomechanical design of the Berkeley lower extremity exoskeleton (BLEEX)," *IEEE/ASME Trans. Mechatronics*, vol. 11, no. 2, pp. 128–138, Apr. 2006.

[56] J. L. Pons, *Wearable Robots: Biomechatronic Exoskeletons*, 2008.

[57] M. Sartori, M. Reggiani, D. G. Lloyd, and E. Pagello, "A neuromusculoskeletal model of the human lower limb: towards EMG-driven actuation of multiple joints in powered orthoses." *IEEE Int. Conf. Rehabil. Robot.*, vol. 2011, p. 5975441, Jan. 2011.

[58] E. J. Rechy-Ramirez and H. Hu, "Bio-signal based control in assistive robots: a survey," *Digit. Commun. Networks*, vol. 1, no. 2, pp. 85–101, Apr. 2015.

[59] J. R. Wolpaw, N. Birbaumer, W. J. Heetderks, D. J. McFarland, P. H. Peckham, G. Schalk, E. Donchin, L. A. Quatrano, C. J. Robinson, and T. M. Vaughan, "Brain-computer interface technology: a review of the first international meeting." *IEEE Trans. Rehabil. Eng.*, vol. 8, no. 2, pp. 164–73, Jun. 2000.

[60] L. F. Nicolas-Alonso and J. Gomez-Gil, "Brain computer interfaces, a review." *Sensors (Basel).*, vol. 12, no. 2, pp. 1211–79, Jan. 2012.

[61] A. L. S. Ferreira, L. C. de Miranda, E. E. C. de Miranda, and S. G. Sakamoto, "A Survey of Interactive Systems based on Brain-Computer Interfaces," pp. 3–13, Aug. 2013.

[62] J. M. Carmena, M. A. Lebedev, R. E. Crist, J. E. O'Doherty, D. M. Santucci, D. F. Dimitrov, P. G. Patil, C. S. Henriquez, and M. A. L. Nicolelis, "Learning to control a brain-machine interface for reaching and grasping by primates." *PLoS Biol.*, vol. 1, no. 2, p. E42, Nov. 2003.

[63] L. Tonin, T. Carlson, R. Leeb, and J. del R Millan, "Brain-controlled telepresence robot by motor-disabled people," in *2011 Annu. Int. Conf. IEEE Eng. Med. Biol. Soc.*, vol. 2011. IEEE, Aug. 2011, pp. 4227–4230.

[64] L. R. Hochberg, D. Bacher, B. Jarosiewicz, N. Y. Masse, J. D. Simeral, J. Vogel, S. Haddadin, J. Liu, S. S. Cash, P. van der Smagt, and J. P. Donoghue, "Reach and grasp by people with tetraplegia using a neurally controlled robotic arm." *Nature*, vol. 485, no. 7398, pp. 372–5, May 2012.

[65] J. J. Shih, D. J. Krusienski, and J. R. Wolpaw, "Brain-computer interfaces in medicine." *Mayo Clin. Proc.*, vol. 87, no. 3, pp. 268–79, Mar. 2012.

[66] J. J. Daly and J. R. Wolpaw, "Brain-computer interfaces in neurological rehabilitation." *Lancet. Neurol.*, vol. 7, no. 11, pp. 1032–43, Nov. 2008.

[67] M. Grosse-Wentrup, D. Mattia, and K. Oweiss, "Using brain-computer interfaces to induce neural plasticity and restore function." *J. Neural Eng.*, vol. 8, no. 2, p. 025004, Apr. 2011.

[68] S. L. Gonzalez Andino, C. Herrera-Rincon, F. Panetsos, and R. Grave de Peralta, "Combining BMI Stimulation and Mathematical Modeling for Acute Stroke Recovery and Neural Repair," *Front. Neurosci.*, vol. 5, p. 87, Jan. 2011.

[69] A.-S. Wahl and M. E. Schwab, "Finding an optimal rehabilitation paradigm after stroke: enhancing fiber growth and training of the brain at the right moment." *Front. Hum. Neurosci.*, vol. 8, p. 381, Jan. 2014.

[70] J. P. Donoghue, "Connecting cortex to machines: recent advances in brain interfaces," *Nat. Neurosci.*, vol. 5, pp. 1085–1088, Oct. 2002.

[71] N. B. Thomas Navin Lal, Thilo Hinterberger, Guido Widman, Michael Schröder, Jeremy Hill, Wolfgang Rosenstiel, Christian E. Elger, Bernhard Schölkopf, "Methods Towards Invasive Human Brain Computer Interfaces," in *Adv. Neural Inf. Process.* MIT Press, 2005, pp. 737–744.

[72] R. Sitaram, A. Caria, R. Veit, T. Gaber, G. Rota, A. Kuebler, and N. Birbaumer, "FMRI brain-computer interface: a tool for neuroscientific research and treatment." *Comput. Intell. Neurosci.*, p. 25487, Jan. 2007.

[73] J. Mellinger, G. Schalk, C. Braun, H. Preissl, W. Rosenstiel, N. Birbaumer, and A. Kübler, "An MEG-based brain-computer interface (BCI)." *Neuroimage*, vol. 36, no. 3, pp. 581–93, Jul. 2007.

[74] S. M. Coyle, T. E. Ward, and C. M. Markham, "Brain–computer interface using a simplified functional near-infrared spectroscopy system," *J. Neural Eng.*, vol. 4, no. 3, pp. 219–226, Sep. 2007.

[75] D. Farina and F. Negro, "Accessing the neural drive to muscle and translation to neurorehabilitation technologies." *IEEE Rev. Biomed. Eng.*, vol. 5, pp. 3–14, Jan. 2012.

[76] R. Merletti, M. Aventaggiato, A. Botter, A. Holobar, H. Marateb, and T. M. M. Vieira, "Advances in surface EMG: recent progress in detection and processing techniques." *Crit. Rev. Biomed. Eng.*, vol. 38, no. 4, pp. 305–45, Jan. 2010.

[77] A. Nordez, T. Gallot, S. Catheline, A. Guével, C. Cornu, and F. Hug, "Electromechanical delay revisited using very high frame rate ultrasound." *J. Appl. Physiol.*, vol. 106, no. 6, pp. 1970–5, Jun. 2009.

[78] H. Begovic, G.-Q. Zhou, T. Li, Y. Wang, and Y.-P. Zheng, "Detection of the electromechanical delay and its components during voluntary isometric contraction of the quadriceps femoris muscle." *Front. Physiol.*, vol. 5, p. 494, Jan. 2014.

[79] C. Fleischer and G. Hommel, "A Human–Exoskeleton Interface Utilizing Electromyography," *IEEE Trans. Robot.*, vol. 24, no. 4, pp. 872–882, Aug. 2008.

[80] T. Lenzi, S. M. M. De Rossi, N. Vitiello, and M. C. Carrozza, "Intention-based EMG control for powered exoskeletons." *IEEE Trans. Biomed. Eng.*, vol. 59, no. 8, pp. 2180–90, Aug. 2012.

[81] R. Gopura, D. Bandara, J. Gunasekara, and T. Jayawardane, "Recent Trends in EMG-Based Control Methods for Assistive Robots," in *Electrodiagnosis New Front. Clin. Res.*, H. Turker, Ed. Sciente, Technology and Medicine open access publisher, 2013, pp. 237–268.

[82] K. Kiguchi and Y. Hayashi, "EMG-Based Control of a Lower-Limb Power-Assist Robot," in *Intell. Assist. Robot.*, ser. Springer Tracts in Advanced Robotics, S. Mohammed, J. C. Moreno, K. Kong, and Y. Amirat, Eds. Cham: Springer International Publishing, 2015, vol. 106, pp. 371–383.

[83] R. Chowdhury, M. Reaz, M. Ali, A. Bakar, K. Chellappan, and T. Chang, "Surface Electromyography Signal Processing and Classification Techniques," *Sensors*, vol. 13, no. 9, pp. 12 431–12 466, Sep. 2013.

[84] G. R. Müller-Putz, C. Breitwieser, F. Cincotti, R. Leeb, M. Schreuder, F. Leotta, M. Tavella, L. Bianchi, A. Kreilinger, A. Ramsay, M. Rohm, M. Sagebaum, L. Tonin, C. Neuper, and J. D. R. Millán, "Tools for Brain-Computer Interaction: A General Concept for a Hybrid BCI." *Front. Neuroinform.*, vol. 5, p. 30, Jan. 2011.

[85] B. Z. Allison, C. Brunner, V. Kaiser, G. R. Müller-Putz, C. Neuper, and G. Pfurtscheller, "Toward a hybrid brain-computer interface based on imagined movement and visual attention." *J. Neural Eng.*, vol. 7, no. 2, p. 26007, Apr. 2010.

[86] R. Leeb, S. Perdikis, L. Tonin, A. Biasiucci, M. Tavella, M. Creatura, A. Molina, A. Al-Khodairy, T. Carlson, and J. D. R. Millán, "Transferring brain-computer interfaces beyond the laboratory: successful application control for motor-disabled users." *Artif. Intell. Med.*, vol. 59, no. 2, pp. 121–32, Oct. 2013.

[87] T. Carlson, L. Tonin, S. Perdikis, R. Leeb, and J. del R Millán, "A hybrid BCI for enhanced control of a telepresence robot." *Conf. Proc. ... Annu. Int. Conf. IEEE Eng. Med. Biol. Soc. IEEE Eng. Med. Biol. Soc. Annu. Conf.*, vol. 2013, pp. 3097–100, Jan. 2013.

[88] G. Pfurtscheller, B. Z. Allison, C. Brunner, G. Bauernfeind, T. Solis-Escalante, R. Scherer, T. O. Zander, G. Mueller-Putz, C. Neuper, and N. Birbaumer, "The hybrid BCI." *Front. Neurosci.*, vol. 4, p. 30, Jan. 2010.

[89] M. R. Tucker, J. Olivier, A. Pagel, H. Bleuler, M. Bouri, O. Lambercy, J. D. R. Millán, R. Riener, H. Vallery, and R. Gassert, "Control strategies for active lower extremity prosthetics and orthotics: a review." *J. Neuroeng. Rehabil.*, vol. 12, p. 1, Jan. 2015.

[90] F. O. Flemisch, C. A. Adams, S. R. Conway, K. H. Goodrich, M. T. Palmer, and P. C. Schutte, "The H-Metaphor as a Guideline for Vehicle Automation and Interaction," NASA Langley Research Center, Hampton, VA, United States, Tech. Rep., Jan. 2003.

[91] L. Tonin, R. Leeb, M. Tavella, S. Perdikis, and J. d. R. Millan, "The role of shared-control in BCI-based telepresence," in *2010 IEEE Int. Conf. Syst. Man Cybern.* IEEE, Oct. 2010, pp. 1462–1466.

[92] T. Carlson and J. del R. Millan, "Brain-Controlled Wheelchairs: A Robotic Architecture," *IEEE Robot. Autom. Mag.*, vol. 20, no. 1, pp. 65–73, Mar. 2013.

[93] M. Q. Liu, F. C. Anderson, M. H. Schwartz, and S. L. Delp, "Muscle contributions to support and progression over a range of walking speeds." *J. Biomech.*, vol. 41, no. 15, pp. 3243–52, Nov. 2008.

[94] M. H. Schwartz, A. Rozumalski, and J. P. Trost, "The effect of walking speed on the gait of typically developing children." *J. Biomech.*, vol. 41, no. 8, pp. 1639–50, Jan. 2008.

[95] A. L. Hof, "Scaling gait data to body size," *Gait Posture*, vol. 4, no. 3, pp. 222–223, May 1996.

[96] T. W. Dorn, A. G. Schache, and M. Pandy, "Muscular strategy shift in human running: dependence of running speed on hip and ankle muscle performance." *J. Exp. Biol.*, vol. 215, no. Pt 11, pp. 1944–56, Jun. 2012.

[97] H. J. Hermens, B. Freriks, C. Disselhorst-Klug, and G. Rau, "Development of recommendations for SEMG sensors and sensor placement procedures." *J. Electromyogr. Kinesiol.*, vol. 10, no. 5, pp. 361–74, Oct. 2000.

[98] A. Seth, M. Sherman, J. A. Reinbolt, and S. L. Delp, "OpenSim: a musculoskeletal modeling and simulation framework for in silico investigations and exchange," *Procedia IUTAM*, vol. 2, pp. 212–232, Jan. 2011.

[99] G. T. Yamaguchi and F. E. Zajac, "A planar model of the knee joint to characterize the knee extensor mechanism," *J. Biomech.*, vol. 22, no. 1, pp. 1–10, Jan. 1989.

[100] S. Delp, J. Loan, M. Hoy, F. Zajac, E. Topp, and J. Rosen, "An interactive graphics-based model of the lower extremity to study orthopaedic surgical procedures," *IEEE Trans. Biomed. Eng.*, vol. 37, no. 8, pp. 757–767, 1990.

[101] S. R. Hamner, A. Seth, and S. L. Delp, "Muscle contributions to propulsion and support during running." *J. Biomech.*, vol. 43, no. 14, pp. 2709–16, Oct. 2010.

[102] S. R. Ward, C. M. Eng, L. H. Smallwood, and R. L. Lieber, "Are current measurements of lower extremity muscle architecture accurate?" *Clin. Orthop. Relat. Res.*, vol. 467, no. 4, pp. 1074–82, Apr. 2009.

[103] A. Seth, M. Sherman, P. Eastman, and S. Delp, "Minimal formulation of joint motion for biomechanisms." *Nonlinear Dyn.*, vol. 62, no. 1, pp. 291–303, Oct. 2010.

[104] M. A. Sherman, A. Seth, and S. L. Delp, "Simbody: multibody dynamics for biomedical research," *Procedia IUTAM*, vol. 2, pp. 241–261, 2011.

[105] J. L. Hicks, T. K. Uchida, A. Seth, A. Rajagopal, and S. Delp, "Is my model good enough? Best practices for verification and validation of musculoskeletal models and simulations of human movement." *J. Biomech. Eng.*, vol. 137, no. 2, p. 020905, Dec. 2014.

[106] D. G. Thelen, "Adjustment of muscle mechanics model parameters to simulate dynamic contractions in older adults." *J. Biomech. Eng.*, vol. 125, no. 1, pp. 70–7, Feb. 2003.

[107] D. G. Thelen and F. C. Anderson, "Using computed muscle control to generate forward dynamic simulations of human walking from experimental data," *J. Biomech.*, vol. 39, no. 6, pp. 1107–1115, Jan. 2006.

[108] R. Bortoletto, E. Pagello, and D. Piovesan, "Lower Limb Stiffness Estimation during Running: The Effect of Using Kinematic Constraints in Muscle Force Optimization Algorithms," in *Simulation, Model. Program. Auton. Robot.*, ser. Lecture Notes in Computer Science, D. Brugali, J. F. Broenink, T. Kroeger, and B. A. MacDonald, Eds., vol. 8810. Cham: Springer International Publishing, 2014, pp. 364–375.

[109] R. Bortoletto, E. Pagello, and D. Piovesan, "How different human muscle models affect the estimation of lower limb joint stiffness during running," in *Work. Neuro-Robotics Patient-Specific Rehabil. IAS-13*, Jul. 2014.

[110] R. Bortoletto, E. Pagello, and D. Piovesan, "Effects of reserve actuators on optimization solutions: From muscle force to joint stiffness," in *2015 IEEE Int. Conf. Rehabil. Robot.* IEEE, Aug. 2015, pp. 973–978.

[111] F. A. Mussa Ivaldi, P. Morasso, and R. Zaccaria, "Kinematic networks. A distributed model for representing and regularizing motor redundancy." *Biol. Cybern.*, vol. 60, no. 1, pp. 1–16, Jan. 1988.

[112] V. Mohan and P. Morasso, "Passive Motion Paradigm: An Alternative to Optimal Control," *Front. Neurorobot.*, vol. 5, p. 4, Jan. 2011.

[113] H. Nijmeijer and A. van der Schaft, *Nonlinear Dynamical Control Systems*, 2013.

[114] E. G. Walsh and G. W. Wright, "INERTIA, RESONANT FREQUENCY, STIFFNESS AND KINETIC ENERGY OF THE HUMAN FOREARM," *Q. J. Exp. Physiol.*, vol. 72, no. 2, pp. 161–170, Apr. 1987.

[115] X. Hu, W. M. Murray, and E. J. Perreault, "Muscle short-range stiffness can be used to estimate the endpoint stiffness of the human arm." *J. Neurophysiol.*, vol. 105, no. 4, pp. 1633–41, Apr. 2011.

[116] L. Cui, E. J. Perreault, H. Maas, and T. G. Sandercock, "Modeling short-range stiffness of feline lower hindlimb muscles." *J. Biomech.*, vol. 41, no. 9, pp. 1945–52, Jan. 2008.

[117] D. Piovesan, A. Pierobon, and F. A. Mussa Ivaldi, "Critical Damping Conditions for Third Order Muscle Models: Implications for Force Control," *J. Biomech. Eng.*, vol. 135, no. 10, p. 101010, Sep. 2013.

[118] M. A. Sherman, A. Seth, and S. L. Delp, "WHAT IS A MOMENT ARM? CALCULATING MUSCLE EFFECTIVENESS IN BIOMECHANICAL MODELS USING GENERALIZED COORDINATES." *Proc. ASME Des. Eng. Tech. Conf.*, vol. 2013, Aug. 2013.

[119] S. Calinon, I. Sardellitti, and D. G. Caldwell, "Learning-based control strategy for safe human-robot interaction exploiting task and robot redundancies," in *2010 IEEE/RSJ Int. Conf. Intell. Robot. Syst.* IEEE, Oct. 2010, pp. 249–254.

[120] R. Bortoletto, S. Michieletto, E. Pagello, and D. Piovesan, "Human Muscle-Tendon Stiffness Estimation During Normal Gait Cycle Based on Guassian Mixture Model," in *Intell. Auton. Syst. 13*, ser. Advances in Intelligent Systems and Computing, E. Menegatti, N. Michael, K. Berns, and H. Yamaguchi, Eds., vol. 302. Cham: Springer International Publishing, 2016.

[121] A. P. Dempster, N. M. Laird, and D. B. Rubin, "Maximum Likelihood from Incomplete Data via the EM Algorithm," 1976.

[122] M. H. DeGroot, *Optimal Statistical Decisions*, 2004.

[123] G. Schwarz, "Estimating the Dimension of a Model," *Ann. Stat.*, vol. 6, no. 2, pp. 461–464, Mar. 1978.

[124] K. Radkhah, D. Scholz, O. von Stryk, M. Maus, and A. Seyfarth, "Towards Human-Like Bipedal Locomotion with Three-Segmented Elastic Legs," in *Robot. (ISR), 2010 41st Int. Symp. 2010 6th Ger. Conf. Robot.*, 2010, pp. 1–8.

[125] K. Radkhah, T. Lens, and O. von Stryk, "Detailed dynamics modeling of BioBiped's monoarticular and biarticular tendon-driven actuation system," in *2012 IEEE/RSJ Int. Conf. Intell. Robot. Syst.* IEEE, Oct. 2012, pp. 4243–4250.

[126] R. Bortoletto, M. Sartori, F. He, and E. Pagello, "Simulating an Elastic Bipedal Robot Based on Musculoskeletal Modeling," in *Biomim. Biohybrid Syst. 2012 - First Int. Conf. Living Mach. 2012*, ser. Lecture Notes in Computer Science, T. J. Prescott, N. F. Lepora, A. Mura, and P. F. M. J. Verschure, Eds., vol. 7375. Berlin, Heidelberg: Springer Berlin Heidelberg, 2012, pp. 26–37.

[127] R. Bortoletto, M. Sartori, F. He, and E. Pagello, "Modeling and Simulating Compliant Movements in a Musculoskeletal Bipedal Robot," in *Simulation, Model. Program. Auton. Robot.*, ser. Lecture Notes in Computer Science, I. Noda, N. Ando, D. Brugali, and J. J. Kuffner, Eds., vol. 7628. Berlin, Heidelberg: Springer Berlin Heidelberg, 2012, pp. 237–250.

[128] F. He, Y. Liang, H. Zhang, and E. Pagello, "Modeling, Dynamics and Control of an Extended Elastic Actuator in Musculoskeletal Robot System," in *Intell. Auton. Syst. 12*, ser. Advances in Intelligent Systems and Computing, S. Lee, H. Cho, K.-J. Yoon, and J. Lee, Eds., vol. 194. Berlin, Heidelberg: Springer Berlin Heidelberg, 2013, pp. 671–681.

[129] T. Reilly, J. K. O'Rourke, D. Steudler, D. Piovesan, and R. Bortoletto, "LOCOMOTIVE UNDER-ACTUATED IMPLEMENT GUIDED VIA ELASTIC ELEMENTS (L.U.I.G.E.E): A PRELIMINARY DESIGN," in *ASME 2015 Int. Mech. Eng. Congr. Expo. IMECE2015*, Houston, Texas, 2015.

[130] J. R. Papich, C. J. Kennett, and D. Piovesan, "Open-Source Software in Biomedical Education: From Tracking to Modeling Movements: American Society for Engineering Education," in *121st ASEE Annu. Conf. Expo.*, Indianapolis, 2014.

[131] S. K. Ong and A. Nee, "Virtual Reality and Augmented Reality Applications in Manufacturing," Aug. 2004.

[132] R. C. Romero, A. Cardenas, and D. Piovesan, "Viscoelastic properties of the ankle during quiet standing via raster images and EKF," in *2014 IEEE Signal Process. Med. Biol. Symp.* IEEE, Dec. 2014, pp. 1–5.

[133] D. T. Westwick and E. J. Perreault, "Estimates of acausal joint impedance models." *IEEE Trans. Biomed. Eng.*, vol. 59, no. 10, pp. 2913–21, Oct. 2012.

[134] D. Simon, *Optimal State Estimation: Kalman, H Infinity, and Nonlinear Approaches*, 1st ed. Wiley-Interscience, 2006.

[135] D. A. Winter, A. E. Patla, F. Prince, M. Ishac, and K. Gielo-Perczak, "Stiffness Control of Balance in Quiet Standing," *J Neurophysiol*, vol. 80, no. 3, pp. 1211–1221, Sep. 1998.

[136] M. Günther and R. Blickhan, "Joint stiffness of the ankle and the knee in running," *J. Biomech.*, vol. 35, no. 11, pp. 1459–1474, Nov. 2002.

[137] D. Stefanyshyn and B. Nigg, "Dynamic Angular Stiffness of the Ankle Joint During Running and Sprinting," *J. Appl. Biomech.*, vol. 14, no. 3, pp. 292–299, 1998.

[138] I. D. Loram and M. Lakie, "Direct measurement of human ankle stiffness during quiet standing: the intrinsic mechanical stiffness is insufficient for stability," *J. Physiol.*, vol. 545, no. 3, pp. 1041–1053, Dec. 2002.

[139] E. J. Rouse, L. J. Hargrove, A. Akhtar, and T. A. Kuiken, "Validation of methods for determining ankle stiffness during walking using the Perturberator robot," in *2012 4th IEEE RAS EMBS Int. Conf. Biomed. Robot. Biomechatronics*. IEEE, Jun. 2012, pp. 1650–1655.

[140] M. Plocharski and P. Plocharski, "Ankle joint stiffness during phases of human walking," 2013.

[141] H. Lee and N. Hogan, "Time-Varying Ankle Mechanical Impedance During Human Locomotion." *IEEE Trans. Neural Syst. Rehabil. Eng.*, vol. 23, no. 5, pp. 755–64, Sep. 2015.

[142] D. Piovesan, A. Pierobon, P. DiZio, and J. R. Lackner, "Experimental measure of arm stiffness during single reaching movements with a time-frequency analysis." *J. Neurophysiol.*, vol. 110, no. 10, pp. 2484–96, Nov. 2013.

[143] T. F. Besier, D. G. Lloyd, and T. R. Ackland, "Muscle activation strategies at the knee during running and cutting maneuvers." *Med. Sci. Sports Exerc.*, vol. 35, no. 1, pp. 119–27, Jan. 2003.

[144] M. Millard, T. Uchida, A. Seth, and S. L. Delp, "Flexing computational muscle: modeling and simulation of musculotendon dynamics." *J. Biomech. Eng.*, vol. 135, no. 2, p. 021005, Feb. 2013.

[145] C. S. Knabe, V. Orekhov, M. A. Hopkins, B. Y. Lattimer, and D. W. Hong, "Two configurations of series elastic actuators for linearly actuated humanoid robots with large range of motion," in *2014 IEEE-RAS Int. Conf. Humanoid Robot.* IEEE, Nov. 2014, pp. 1096–1096.

[146] C. E. García, D. M. Prett, and M. Morari, "Model predictive control: Theory and practice—A survey," *Automatica*, vol. 25, no. 3, pp. 335–348, May 1989.

[147] M. Grimmer, M. Eslamy, S. Gliech, and A. Seyfarth, "A comparison of parallel- and series elastic elements in an actuator for mimicking human ankle joint in walking and running," *Proc. - IEEE Int. Conf. Robot. Autom.*, pp. 2463–2470, 2012.